3D Modeling of Indoor Building Geometry Using Unmanned Aerial Systems

Wael Elhassan

A Thesis in

The Department of

Building, Civil and Environmental Engineering

Presented in Partial Fulfillment of the Requirements

For the Degree of

Master of Applied Sciences (in Civil Engineering) at

Concordia University

Montreal, Quebec, Canada

March 2016

CONCORDIA UNIVERSITY
School of Graduate Studies

This is to certify that the thesis prepared

By: Wael Elhassan

Entitled: 3D Modeling of Indoor Building Geometry Using Unmanned Aerial Systems

and submitted in partial fulfillment of the requirements for the degree of

Master of Applied Science in Civil Engineering

complies with the regulations of the University and meets the accepted standards with respect to originality and quality.

Signed by the final Examining Committee:

_____ Chair
Dr. Khaled Galal

_____ Examiner
Dr. Amin Hammad

_____ Examiner
Dr. Theodore Stathopoulos

_____ Supervisor
Dr. Z. Zhu

Approved by _____

Chair of Department or Graduate Program Director

March 2016

_____

Dean of Faculty

ABSTRACT

3D Modeling of Indoor Building Geometry using Unmanned Aerial Systems

Wael Elhassan

As-built Building Information Models (BIMs) can significantly enhance the efficiency of facility management and operations. However, they are seldom used in the architecture, engineering, construction, and facility management (AEC/FM) industries due to the difficulty of collecting the spatial information required to create such BIMs. Typically, this spatial information is collected through manual field surveys, which are time-consuming and error-prone. Therefore, image-based sensing techniques have been proposed and tested for the three-dimensional (3D) modeling of spatial information using images captured by handheld cameras. Moreover, with recent technological advancements, Unmanned Aerial Systems (UAS) equipped with high-definition cameras have become a powerful tool for remote image acquisition.

So far, it is still not clear whether images remotely captured by a UAS can be used for the 3D modeling of indoor building environments. The main objectives of this research were: (a) to test the feasibility of using a UAS for the 3D modeling indoor building environments, and (b) to evaluate the effectiveness of using the UAS for 3D modeling in terms of accuracy, density, time, and cost. In order to achieve these objectives, a UAS is first deployed to collect several overlapping images of an indoor building environment. Next, a Structure from Motion (SfM) algorithm is applied to generate a 3D point cloud that represents the spatial information of the indoor building environment. Later, the accuracy and density of this 3D point cloud were evaluated by comparing it with the ground truth point cloud generated from a laser scanner. The time and cost needed for modeling using the UAS were also recorded and compared with the ones from the laser scanner. This framework was applied in two case studies: (1) the 12th floor of the Hall building, and (2) the 2nd floor of the EV building, at Concordia University. The results of these studies showed that 80% of the 3D points had a deviation of up to 8.8 cm from the ground truth. Approximately 20% of those points had a deviation of 0.81 cm or less. Overall, these studies demonstrate that UAS-based modeling is able to model the spatial information of indoor building environments with dense point clouds and with acceptable accuracy. Furthermore, the studies also indicate that the 3D modeling of spatial information with a UAS can be a time- and cost-effective approach.

ACKNOWLEDGMENTS

This journey would not have been possible without the support of my family, supervisor, and friends. To my family, thank you for your support and inspiration throughout this journey. Special thanks to my father and my idol Mohammed Elhassan for always pushing me to be the best person I can be, and motivating me to follow this path. Special thanks to my mother Mei Elzard, for her constant emotional support and prayers.

My deepest gratitude goes to my supervisor Dr. Zhenhua Zhu for his continuous support throughout this journey, for his patience, motivation, and immense knowledge. His guidance has greatly helped me throughout this research. I could not imagine I could have made it without him. In addition, I would like to thank my examiners, Dr. Amin Hammad, Dr. Khaled Galal, and Dr. Theodore Stathopoulos for their precious time, valuable advice and helpful suggestions in reviewing my thesis.

My sincere thanks go to my colleague and friend, Ghassan Al Lafi, for helping in the fieldwork, and for his support. In addition, I would like to thank my friends Ryan Persram and Monica Crosetta for their proofreading and support throughout this journey.

Finally, I would like to show my appreciation to the Natural Sciences and Engineering Research Council of Canada (NSERC) for their financial support

TABLE OF CONTENTS

LIST OF FIGURES

LIST OF TABLES

CHAPTER 1: INTRODUCTION

1.1. Background and Motivation

Traditional construction documents (i.e., 2D plans and drawings, technical specifications, etc.) are considered obsolete and lead to increased costs when used in the design, construction, and maintenance phases of a facility project (Qu, Coco, Rönnäng, & Sun, 2014). These documents represent the facility's 3D built environment and its building information with 2D representations for each building discipline (e.g., Architectural, Structural, Mechanical, Electrical, etc.; Qu et al., 2014). This makes the detection of design errors and omissions in the design phase a challenging task (Qu et al., 2014). Design errors and omissions that are not discovered until the construction phase can lead to project delays, cost overruns, and decreased productivity (Qu et al., 2014). Moreover, using traditional construction documents as a communication platform between the different stakeholders involved in the facility project can be highly inefficient. According to the National Institute of Standards and Technology (NIST), the capital facilities industry in the United States wastes $15.8 billion annually on interoperability issues and miscommunication between project stakeholders (Gallaher, O'Connor, Dettbarn, & Gilday, 2004).

Building Information Models (BIMs) are currently replacing traditional construction documents since they offer various benefits to the project stakeholders (Tang, Huber, Akinci, Lipman, & Lytle, 2010). A BIM represents the physical and functional characteristics of a facility in a digital format (Smith, 2007). That is, the BIM not only represents the facility's geometric information, but also contains metadata about the facility's building components such as material specifications, energy data, and cost and schedule information (Qu et al., 2014; Smith, 2007). This offers immaculate simulation and visualization abilities for building energy performance analysis, daylight analysis, and clash detection of components from the various building disciplines (e.g., detecting clashes between mechanical ducts and electrical cable trays; Smith, 2007). Also, the BIM can be used to instantly generate reports and drawings that are helpful for purchasing, fabrication, and other construction operations (Ball, 2014). Furthermore, when the BIM is shared and collaborated on the cloud computing technology, it can serve as the knowledge base for the different project stakeholders (Ball, 2014). Depending on the role of the stakeholders, they are allowed to insert, extract, or modify information in the BIM at any time and share it with other

stakeholders (Smith, 2007). Consequently, BIMs can facilitate efficient communication between project stakeholders, which can reduce the overall cost and time of exchanging information throughout the design and construction phases of a facility project (Smith, 2007). The benefits that can be gained from using BIMs have encouraged a worldwide shift by the Architecture, Engineering, and Construction (AEC) community towards using BIMs instead of traditional construction documents. According to a smart market report by McGraw-Hill Construction (2012), the adoption of BIM by construction professionals in North America has surged from 28% in 2007 to 71% in 2012 In the UK, the adoption of BIM has increased from 31% in 2010 to 54% in 2013 (The National Building Specification, 2014).

Since BIMs are a valuable tool for the design and construction phases, many owners and facility managers started to believe that BIMs could be beneficial for the operations and maintenance (O&M) phase (McGraw-Hill Construction, 2014). The O&M phase is the longest and most expensive phase of the facility's lifecycle, where it makes up approximately 68% of the total lifecycle cost (Giel & Issa, 2011). In this phase, owners and facility managers use as-built documents (usually provided by the contractor) for maintenance, repairs, and planning future renovations. Therefore, these documents should be as accurate as possible and should be handled efficiently, but this is rarely the case. According to a report by the NIST, Gallaher et al. (2004) claimed that the capital facilities industry in North America wasted $10.5 billion on processing, communicating, and revising as-built information in 2002. Thus, it is necessary to find a more efficient way of handling as-built information. Substituting traditional as-built documents with a BIM (i.e., as-built BIM) can offer numerous benefits to the owner and facility management team. Firstly, the stakeholders involved in managing the facility will be able to access a cloud-based as-built BIM to retrieve, add, or modify information, depending on their role. This will facilitate efficient communication between the various stakeholders, and reduce the overall cost and time of handling as-built information (Tang et al., 2010). Secondly, the as-built BIM can be used to locally search for objects within the facility, as well as efficiently manage its spaces and equipment (Tzedaki & Kamara, 2013). Thirdly, the use of as-built BIMs can enhance the visualization and analysis of proposed renovations, which can improve the efficiency of decision making and planning for future renovations (Tang et al., 2010; Woo, Wilsmann, & Kang, 2010). Finally, the as-built BIM can be used to analyze the facility's energy efficiency, which in turn can facilitate the

design of energy efficient retrofits in order to accommodate sustainability guidelines, such as Leadership in Energy and Environmental Design (LEED) and Green Globes (Woo et al., 2010).

Even though owners and facility managers have started to realize the benefits of BIMs in the O&M phase, few have actually utilized BIMs in their facility management and maintenance operations (Giel & Issa, 2011). This is mainly due to the difficulty of creating BIMs that capture the actual state of the facility as it was built (i.e., as-built BIM). BIMs that are created in the design phase (i.e, as-planned BIMs) hardly ever reflect the actual state of the facility, since the facility is not always constructed exactly as the design specifies (Tang et al., 2010). Furthermore, after the facility is handed over to the client, multiple modifications and changes are done to the facility without proper documentation (Giel & Issa, 2011; Tang et al., 2010). In current practice, creating as-built BIMs involves measuring the facility's existing spatial information in extensive manual field surveys (Klein, Li, & Becerik-Gerber, 2012). These surveys are usually performed using laser distance measurers and measuring tapes (Klein et al., 2012). When an as-planned BIM is available, the spatial information collected is used to update it to create the as-built BIM (Klein et al., 2012). However, when no as-planned BIM exists, the spatial information is used to update the 2D as-built documents, which are then used to construct the as-built BIM (Klein et al., 2012). Since manual field measurements are error-prone and time-consuming, professionals in AEC community are opting for remote sensing techniques in capturing the spatial information needed for their as-built BIMs (Giel & Issa, 2011; Klein et al., 2012). Remote sensing techniques use non-disruptive sensing equipment from a distance to 3D model the spatial information of the surrounding environment (Klein, Li, & Becerik-Gerber, 2011). This information is represented in discrete (x, y, z) point coordinates, which are usually referred to as a 3D point cloud (Qu et al., 2014).

Nowadays, laser-based remote sensing using laser scanners is the most reliable remote sensing technique for the 3D modeling of spatial information (Klein et al., 2012; Qu et al., 2014). In this technique, professional surveyors set up the laser scanner in key locations throughout the facility to 3D model its spatial information (Tang et al., 2010). The laser scanner does this by emitting laser pulses to the surrounding environment (Wang, 2014). The scanner then collects the reflected laser pulses to analyze them and produce a 3D point cloud of the surrounding environment (Wang, 2014). Nowadays, modern laser scanners are able to produce dense point clouds within an accuracy of 2 to 5 mm (Qu et al., 2014). Nonetheless, laser scanners are still

rarely used for various reasons (Klein et al., 2012; Qu et al., 2014). First, laser scanning is time-consuming because surveyors must carefully set up the laser scanner and its reference targets in key locations throughout the facility to capture it completely. In large-scale projects, this might take days of planning and execution (Klein, et al., 2012; Qu et al., 2014). Second, assembling and operating the laser scanning equipment can only be conducted by highly trained professionals (Klein et al., 2012). Finally, and most importantly, many professionals consider laser scanning to be a high capital expenditure since the equipment costs tens of thousands of dollars (Klein et al., 2012; Qu et al., 2014).

An alternative to laser-based remote sensing is the image-based approach, which is becoming more popular due to its affordability and simplicity (Klein et al., 2012; Qu et al., 2014). Image-based remote sensing is a photogrammetric technique that uses a series of overlapping images with well-known camera positions and orientations to 3D model the spatial information (Westoby, Brasington, Glasser, Hambrey, & Reynolds, 2012). Generally, this technique works by identifying, matching, and triangulating common points that appear on several overlapping images to generate the 3D point cloud (Bhatla, Choe, Fierro, & Leite, 2012). In traditional photogrammetric algorithms, the coordinates and orientation of each image taken were obtained from a GPS and electric compass attached to the camera (Westoby et al., 2012). However, in the modern photogrammetric algorithm known as Structure-from-Motion (SfM), the coordinates and orientation of each image taken are automatically calculated (Westoby et al., 2012). Therefore, modern image-based sensing techniques are now able to 3D model the spatial information using ordinary digital cameras without attaching a GPS or a compass (Bhatla et al., 2012; Westoby et al., 2012). Consequently, image-based sensing techniques are now offering a cost-efficient and portable solution for remote sensing (Klein et al., 2012). In addition, the appearance of commercial SfM software platforms (e.g., Autodesk Recap360, PhotoModeler, Microsoft Photosynth) have made image-based sensing user-friendly, since the user only needs to upload a series of overlapping images to generate the 3D point cloud (Klein et al., 2012).

To date, image-based sensing of indoor building environments has been conducted using images captured by handheld cameras. However, image-based sensing could also be achieved remotely if the images are collected by Unmanned Aerial Systems (UAS). UAS (also referred to as Unmanned Aerial Vehicles, Drones) are generic aircrafts that are designed to operate without

human pilots on-board (Remondino, Barazzetti, Nex, Scaioni, & Sarazzi, 2011). According to Eisenbeiß (2009), UAS offer numerous benefits. Firstly, UAS can be used in risky and dangerous situations without endangering human life. Secondly, because of their small size, they can be used in confined environments and inaccessible locations. Thirdly, UAS are not subjected to physiological limitations and economical expenses associated with on-board human pilots. Fourthly, UAS collect data in real time by transmitting live video (or images) to the ground control station. Moreover, recent technological developments have made modern UAS more efficient in terms of size, cost, payload capacity, and flight performance (Colomina & Molina, 2014). In addition, with the arrival of lightweight and cost-efficient equipment such as global positioning systems (GPS), and lightweight digital cameras, UAS have become an effective and cost-efficient tool for remote image acquisition (Siebert & Teizer, 2014). These advantages have led to more widespread applications of UAS in the field of engineering. For example, several research groups are currently using UAS-based imagery for inspecting hazardous and inaccessible locations, and detecting environmental hazards (e.g., landslides, forest fires, etc.) (Rufino & Moccia, 2005; Metni & Hamel, 2007). They can also be used in agricultural analyses, and surveying dangerous sites (e.g., quarries, landfills, etc.) (Remondino et al., 2011; Siebert & Teizer, 2014).

Recent image-based sensing techniques allow for cost efficient 3D modeling of spatial information since they only require ordinary digital images (Bhatla et al., 2012; Klein et al., 2012; Westoby et al., 2012). Furthermore, UAS have become commercially available at an affordable price, and can be used for remote image acquisition if mounted with a digital camera. Therefore, using images collected by UAS can be a cost-effective approach for 3D modeling of indoor building environments in a remote manner. Several advantages can be achieved from using this modeling approach, including but not limited to:

(1) Remote image acquisition and modeling of dangerous environments without jeopardizing the safety of staff. For example, UAS can be used to model the indoor environments of nuclear plants and power plants. Moreover, it can be used for post-disaster modeling, i.e., modeling a facility just after a disaster (e.g. earthquake, or fire), which can improve the safety of disaster response and assessment.

(2) Aerial image acquisition and modeling of large facilities such as a warehouse or a factory. The typical image acquisition using handheld cameras can be inefficient in such large facilities because it requires numerous images to capture all parts of the environment. However, UAS allow for effective image acquisition in such situations, as the environment can be captured more efficiently via aerial images. In addition, UAS allow for image acquisition of areas inaccessible by foot (e.g., the top of large machinery), which can improve the quality and completeness of the generated 3D model.

1.2. Problem Statement

Recent technological advancements have made modern UAS more efficient in terms of size, cost, and payload capacity. Additionally, the combination of UAS with lightweight, high definition cameras has made UAS a cost-effective solution for remote image acquisition. However, it is still not clear whether images remotely captured by UAS can be used for 3D modeling of indoor building environments. Recent image-based sensing techniques allow for 3D modeling using a collection of digital images, which can be a cost-efficient, portable, and user-friendly approach for collecting spatial. Consequently, image-based sensing techniques are increasingly being tested and implemented in academic research to replace current spatial information modeling techniques. Furthermore, UAS have become widely available in the market today at an affordable price, and if equipped with digital cameras, they can be used for remote image acquisition. This has motivated several research groups to use UAS-based imagery for a wide variety of engineering applications (e.g., inspection, disaster response and prevention, agricultural analysis, and surveying). However, to the author's best knowledge, there is a gap in the literature pertaining to whether images captured remotely by UAS can be used to 3D model indoor building environments.

1.3. Objectives and Proposed Methodology

This research has two main objectives. First, it will test the feasibility of using a UAS for the 3D modeling indoor building environments. Then, it will evaluate the effectiveness of modeling using the UAS in terms of accuracy, density, time and cost.

To achieve these objectives, a camera mounted on a UAS will be used to collect overlapping images of an indoor building environment. These images are then processed using a commercially available SfM software to generate a 3D point cloud of the environment's spatial information (i.e., the UAS-based point cloud). Since laser scanning is the most reliable remote sensing technique

available today, and it can produce dense point clouds within an accuracy of 2 to 5mm (Qu et al., 2014), a 3D point cloud from a laser scanner (i.e., a laser-based point cloud) will serve as the ground truth for this research. To generate the laser-based point cloud, a laser scanner is deployed to scan the same indoor building environment and generate a 3D point cloud of its spatial information. Thereafter, the UAS-based point cloud, the laser-based point cloud, and the time and cost required to create both, are analyzed and compared in order to evaluate the effectiveness of modeling using the UAS. In the evaluation stage, four metrics are computed and compared: 1) accuracy, 2) density, 3) time, and (4) cost. Additionally, any issues faced while creating the UAS-based point cloud will be outlined and discussed.

To measure the accuracy of the UAS-based point cloud. First, it is registered in a common coordinate system with the ground truth point cloud (from the laser scanner). Afterward, a deviation analysis is conducted on two levels: (a) a point cloud level and (b) a control point level. For the point cloud deviation analysis, the deviation of each point in the UAS-based point cloud is calculated relatively from its corresponding location in the ground truth point cloud. For the control point deviation analysis, the coordinates of each control point (which are artificially implanted in the environment before data collection starts) in UAS-based point cloud are compared to their coordinates in the ground truth cloud.

To evaluate the density of the UAS-based point cloud. First, several $1m^2$ sections are taken at various locations in the UAS-based point cloud, and the number of points is computed for each section. Similarly, identical $1m^2$ sections are also taken at the laser-based point cloud, and the number of points is computed. The results from each point cloud are then compared, to evaluate the density of the UAS-based cloud.

A time and cost based comparison will also be conducted. In which the time needed for generating the UAS- and laser-based point clouds are recorded and compared. This will include the time necessary for on-site data collection, and data processing in the office. In addition, the cost of equipment, software, and labor required to create the UAS-based point cloud are estimated, and compared to ones estimated for the laser-based point cloud.

The evaluation will be conducted in two case studies: (1) the 12^{th} floor of the Hall building, and (2) the 2^{nd} floor of the EV building, at Concordia University. The results will be used to investigate if the images captured by the UAS can be used for the 3D modeling of indoor building

environments. And will be used to evaluate the effectiveness of modeling using the UAS. Moreover, the lessons learned and the difficulties encountered from conducting these case studies will be outlined and discussed, to highlight the limitations of using the UAS for modeling indoor building environments.

1.4. Expected Contributions

The results of this research demonstrate that a UAS can be used to 3D model the spatial information of indoor building environments. Moreover, the case studies' findings show that UAS-based modeling is able to generate dense 3D point clouds of the spatial information within acceptable accuracy. In addition, the results indicate that UAS-based modeling can be a time- and cost-efficient approach for the collection of spatial information.

The results and findings of this research can motivate other research groups to develop applications for the UAS. For example, a UAS can be used for post-disaster modeling without endangering human life. In fact, search and rescue missions inside a facility that is affected by a disaster (e.g., earthquake, bombing, etc.) can be very dangerous to the life of the rescue personnel. This is mainly due to the high degree of uncertainty in regards to the facility's stability. Therefore, UAS-based modeling can help engineers develop a method for remotely modeling critical building components (e.g., concrete columns) after the occurrence of a disaster. These models can be used to identify cracks and defects in such critical components, which can be used to assess the facility's stability and ensure the safety of the rescue personnel in search and rescue missions. Furthermore, UAS-based modeling can be also used to simulate the energy efficiency of facilities. Where the UAS can be mounted with an infrared (IR) camera to collect the facility's thermal information. The thermal information can then be fused with the 3D point cloud (i.e., the spatial information) that is created using the camera mounted on the UAS to generate a 3D thermal model of the facility. 3D thermal models enable engineers to detect air infiltration and heat losses from the building envelope, and simulate the facility's energy efficiency, which in turn can facilitate the design of energy efficient retrofits that can reduce the energy wasted and the overall energy cost.

1.5. Thesis Organization

Chapter 1: Introductory chapter that gives brief information on the concepts used in this thesis, and outlines the motivations behind this dissertation. Also, this chapter clearly states the goals and expected contributions of this thesis. The thesis organization is included in this chapter as well.

Chapter 2: This chapter explains the key concepts dealt with in this thesis. And describes related work to this research.

Chapter 3: This chapter clearly outlines the flow of processes that will be followed to achieve the objectives of this research.

Chapter 4: In chapter 4, the implementation of case study I and case study II is described in detail. Also, this chapter explains how the case studies were used to compare UAS-based to laser-based modeling. And, clearly shows the comparison results.

Chapter 5: In chapter 5, the comparison results are discussed to evaluate the effectiveness of using a UAS for 3D modeling. Additionally, any issues encountered while conducting the case studies are discussed in this chapter, to highlight the limitations of using a UAS for the 3D modeling indoor building environments.

Chapter 6: Finally, chapter 6 concludes this research work with a summary of how it was implemented and an overview of the results. Recommendations for future research work are included in this chapter as well.

CHAPTER 2: LITERATURE REVIEW

2.1. As-built BIM

2.1.1. As-built BIM and its Applications

Owners and facility managers typically rely on two-dimensional (2D) as-built documents for facility management operations. These documents serve as a graphical communication platform for the facility management team and other stakeholders. These documents are also used for maintenance, repairs, and planning for future renovations. Therefore, as-built documents should be handled efficiently, and must be accurate. However, this is rarely the case. According to a report by the National Institute of Standards and Technology (NIST), Gallaher et al. (2004) claimed that in 2002, the capital facilities industry in North America wasted $10.5 Billion on processioning, communicating, and revising as-built documents. Thus, it is evident that a more efficient approach for handling as-built information is needed. Substituting traditional as-built documents with an as-built BIM can offer various benefits to the owner and facility management team. Firstly, the stakeholders will be able to access a cloud-based as-built model to retrieve, add, or modify information depending on their role, which can facilitate efficient communication between the different stakeholders, and reduce the overall time and cost of handling as-built information (Tang et al., 2010). Secondly, the as-built BIM can be used for the local search for objects within the facility, and to efficiently manage its spaces and equipment (Tzedaki et al., 2013). Thirdly, the as-built BIM can be used for visualization and analysis of proposed renovations (Woo et al., 2010). In turn, this can facilitate effective decision making and planning for future renovations (Woo et al., 2010) Finally, the as-built BIM can be used for analyzing the facility's energy efficiency, which can help in the design of energy efficient retrofits that can reduce the overall energy cost (Woo et al., 2010).

2.1.2. As-built BIM Creation

Conventional methods

The conventional approach for creating as-built BIMs involves importing the up-to-date 2D as-built drawings to a BIM modeling software platform (e.g., Autodesk Revit), to trace up these 2D drawings and create the as-built BIM (Giel & Issa, 2011). This process is extremely manual,

error-prone, and time-consuming. Moreover, 2D as-built drawings hardly ever reflect the actual state of the facility, since little is ever done to document the renovations and modifications made after the project is handed over to the client (Giel & Issa, 2011). Therefore, manual field measurement will be required to update the 2D as-built documents before they are used to create the as-built BIM, which is also time-consuming and error-prone.

Point cloud to BIM

Since manual field measurements are extremely inefficient, many professionals in the AEC industry are opting for remote sensing technologies for the collection spatial information (Giel & Issa, 2011; Klein et al., 2012). Remote sensing techniques use non-disruptive sensing equipment to 3D model the surrounding environment's spatial information (Klein et al., 2011). The collected spatial information will be in the form of discrete (x, y, z) point coordinates, usually referred to as 3D point clouds (Qu et al., 2014). 3D point clouds can be used to create an as-built BIM. In order to do this, the 3D point clouds must undergo two highly manual processes: (1) data processing, and (2) BIM modeling.

The first step in data processing is registration. In this step, point clouds from different positions and locations are aligned in a common coordinate system (Jung et al., 2014; Tang et al., 2010). This is done to capture the facility/scene completely in one point cloud (Tang et al., 2010). Registration is achieved through a point cloud processing software (e.g., Autodesk Recap, Trimble RealWorks), in which the user manually identifies and matches points that correspond to the point clouds from the different positions. These points can be targets which were artificially implanted in the environment, or feature points available in the scene (e.g., wall corner). The output of the registration process is a registered point cloud that combines all the point clouds from different positions/locations in a common coordinate system (see Figure 1). Another supplementary task in data processing is data filtering, in which the point cloud is filtered out from any unwanted data (Tang et al., 2010).

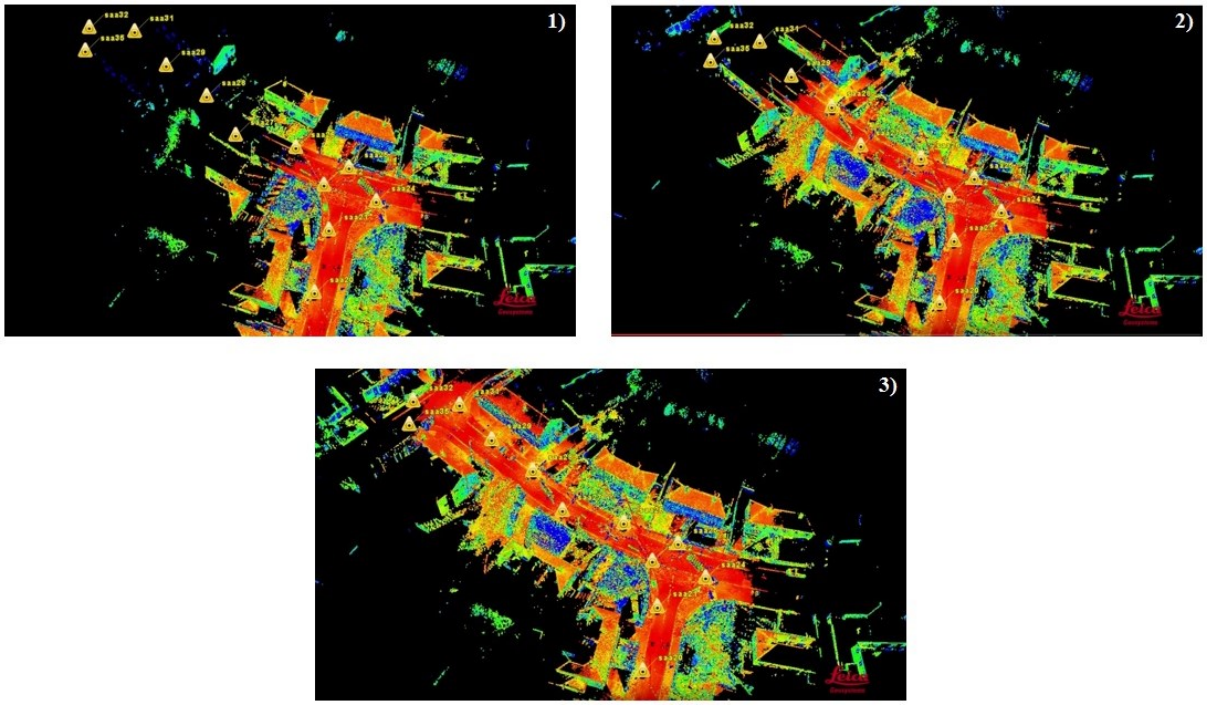

Figure 1: Registration process. (Leica Geosystems, 2012)

In BIM modeling, the registered point cloud will be converted from a collection of discrete 3D point coordinates into a semantically rich BIM. The first step towards doing this is geometric modeling, where the point cloud is converted into a solid geometric model (see Figure 2). This is achieved by fitting geometric primitives (e.g. planes, cylinders, spheres, etc.) to the point cloud (Huber et al., 2011, Jung et al., 2014; Tang et al., 2010). This is necessary for data storage purposes. Because representing the environment with a small number of equations that describe its shape and boundaries is by far more compact than representing it with millions of 3D points (Huber et al., 2011). After the point cloud is converted into a solid 3D model, semantic information is added to it to create the as-built BIM (Huber et al., 2011, Jung et al., 2014; Tang et al., 2010). This entails assigning object categories to the different 3D components (e.g., wall-1 is a brick wall), and establishing relationships between these components (e.g., wall-1 is connected to floor-1; Tang et al., 2010).

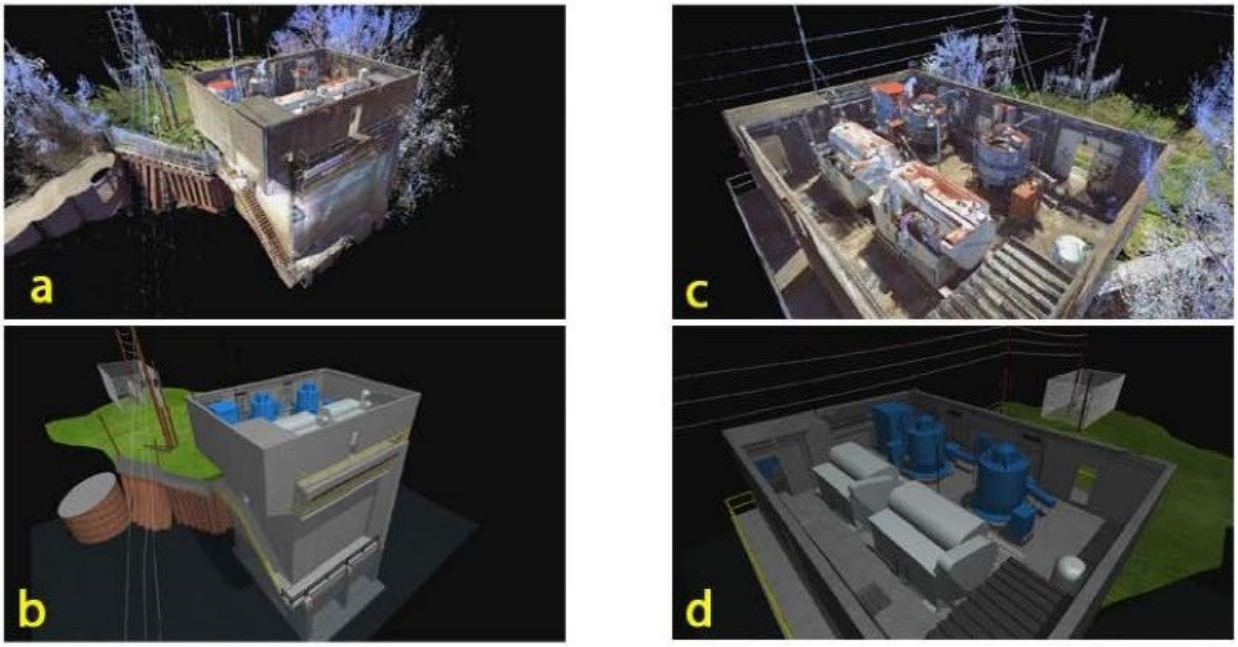

Figure 2: Sample of geometric modeling. (Qu et al., 2014, p. 815)

The process of creating an as-built BIM from a point cloud is mostly manual, time-consuming, and error-prone (Huber et al., 2011, Jung et al., 2014; Tang et al., 2010). This is mainly because the whole process from point cloud registration to BIM modeling cannot be achieved by a single software package. On one hand, the point cloud processing software are able to register, manage and filter the point cloud, but lack BIM-specific capabilities necessary for semantic modeling (Tang et al., 2010). On the other hand, the BIM modeling software cannot handle the massive point cloud data (Tang et al., 2010). Consequently, modelers often need to shuttle back and forth between the different software packages when creating the as-built BIM from a 3D point cloud. This raises the possibility of errors and information loss during the creation of the as-built BIM and makes the process very labor-intensive and tedious. (Tang et al., 2010).

The manual nature of as-built BIM creation has motivated several research efforts which intend to automate this process. However, this has not been achieved yet for several reasons:

1- The abundant number of clutter objects (e.g. furniture, decorations) in indoor environments makes automatic BIM modeling of indoor environments very challenging. This is mainly because clutter objects should not be included in the BIM, and it is very difficult to make the computer automatically distinguish what should and shouldn't be included in the BIM (Tang et al., 2010).

2- The high level of occlusion in indoor environments is problematic to automatic BIM modeling. Modeling occluded objects mainly depends on making assumptions. For example, modeling a wall that is partially occluded/blocked by a closet depends on the assumption that the wall must extend to the floor. These assumptions are difficult for the computer to make on its own (Jung et al., 2014; Tang et al., 2010).

3- The huge size of scanned data often leads to system slowdowns and failure in the modeling process (Jung et al., 2014).

Recently, there has been considerable research attempting to automate the process of as-built BIM creation. Discussing these research efforts in detail is considered out of the scope of this thesis. However, it is worth noting that Tang et al. (2010) has surveyed the latest techniques developed to automate the process of as-built BIM creation.

2.2. Spatial Information Collection Techniques

Even though owners and facility managers have started to realize the benefits of as-built BIMs in the O&M phase, few have actually utilized them in their facility management and maintenance operations (Giel & Issa, 2011). This is mainly due to the difficulty of creating and maintaining BIMs that represent the actual state of the facility. BIMs that are created in the design phase (i.e, as-planned BIMs) hardly ever reflect the actual state of the facility since it is not always constructed exactly as the design specifies (Tang et al., 2010). Furthermore, after the facility is handed over to the client, multiple modifications and changes are done to it without proper documentation (Giel & Issa, 2011; Tang et al., 2010). Therefore, in order to create an as-built BIM that represents the facility's actual condition, its current spatial information must be collected. In this section, the currently available techniques for the collection of spatial information will be reviewed and discussed.

2.2.1. Traditional Manual Field Surveys

The conventional approach for the collection spatial information involves performing manual field surveys. In these surveys, surveyors use laser distance measurers (see Figure 3) and measuring tapes to measure and document the dimensions of all the building components (Jung, et al., 2014). These surveys are rather labor-intensive, error-prone, and time-consuming.

Figure 3: Laser distance measurer. (DeWALT Electronic Press Kit, 2009)

Since manual field surveys are time-consuming and error-prone, professionals have started to use remote sensing techniques for the collection of spatial information (Giel & Issa, 2011; Klein et al., 2012). In remote sensing, non-disruptive sensing equipment is used to 3D model the spatial information of the surrounding environment and represent it with 3D point clouds. The following two sections (2.2.2 & 2.2.3) review the two most recognized remote sensing techniques available today.

2.2.2. Laser-based Remote Sensing

In laser-based remote sensing, a laser scanner is used to emit laser signals to the surrounding environment and collect its spatial information (Albourae, 2014; Klein et al., 2012; Leica Geosystems, 2012). According to Wang (2014), there are two types of laser scanners available in the market today, time-of-flight laser scanners, and phase-shift laser scanners.

Time-of-flight laser scanners

Time-of-flight (TOF) laser scanners emit pulses of laser to the surrounding environment. These pulses reflect on objects in the environment and return to the scanner (Faro Technologies Inc, 2011; Leica Geosystems, 2012). The scanner records the time it took for the laser to travel from the scanner to the object and come back; hence the name time of flight. It then measures the distance between them using Equation 1 (Leica Geosystems, 2012). In addition to the distance measurement, the scanner also records the horizontal and vertical angles for each distance measurement (Faro Technologies Inc, 2011; Leica Geosystems, 2012). To do this, the scanner

revolves around its vertical axis to form a horizontal plate of laser that is used to measure the horizontal angle α for each measured point (see Figure 5-a) (Faro Technologies Inc, 2011; Leica Geosystems, 2012). Furthermore, the scanner also has a small mirror that is revolving around the horizontal axis which reflects the pulses of laser to form a vertical plate from it (see Figure 5-b). This vertical plate is used to measure the vertical angle θ for each distance measurement (Faro Technologies Inc, 2011; Leica Geosystems, 2012). Finally, after collecting all this information for one targeted point (see Figure 6), those measurements are converted into the Cartesian coordinates using Equation 2 (Albourae, 2014).

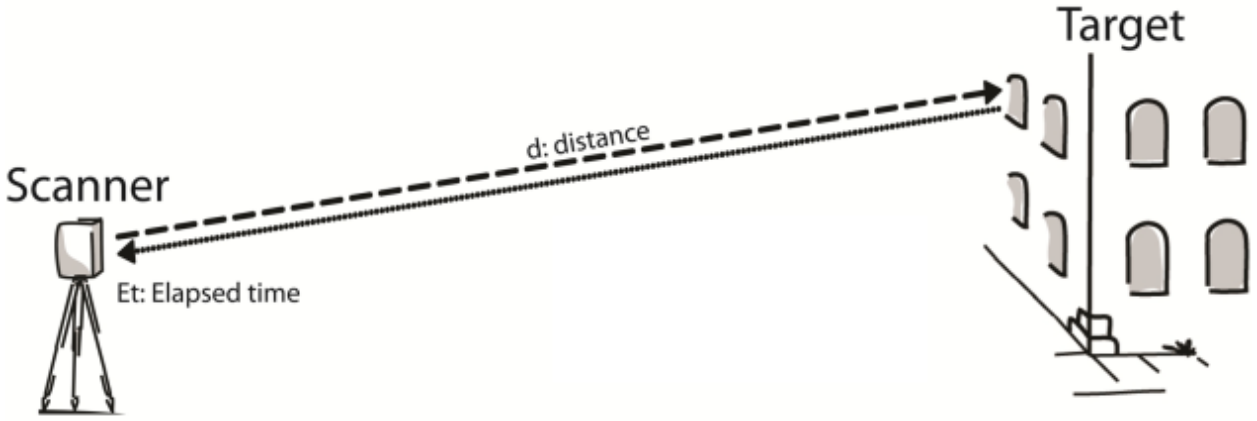

Figure 4: TOF laser scanner distance calculation. (Lato, 2010)

$$d = \frac{(Et \times c)}{2} \qquad \text{Equation 1}$$

Where:

d: distance between the point targeted and the scanner

c: speed of light in air

Et: time between send and receiving the light beam

$$\begin{bmatrix} x \\ y \\ z \end{bmatrix} = d \begin{bmatrix} \cos\theta . \cos\alpha \\ \cos\theta . \sin\alpha \\ \sin\theta \end{bmatrix} \qquad \text{Equation 2}$$

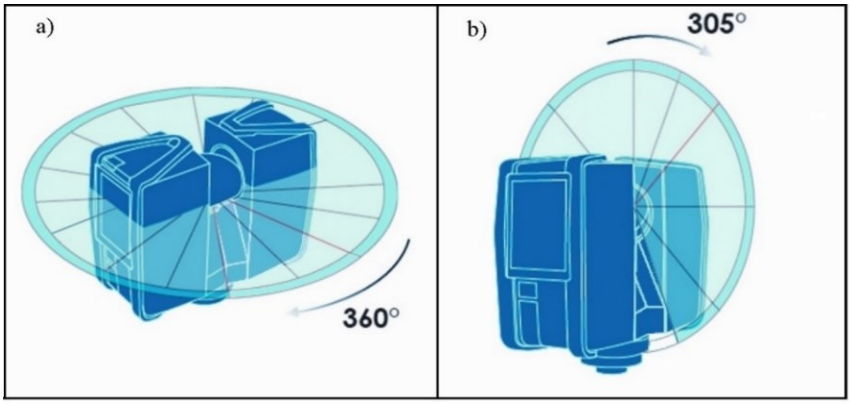

Figure 5: Laser scanner angle measurements: a) horizontal angle measurement, b) vertical angle measurement. (Faro Technologies Inc, 2011)

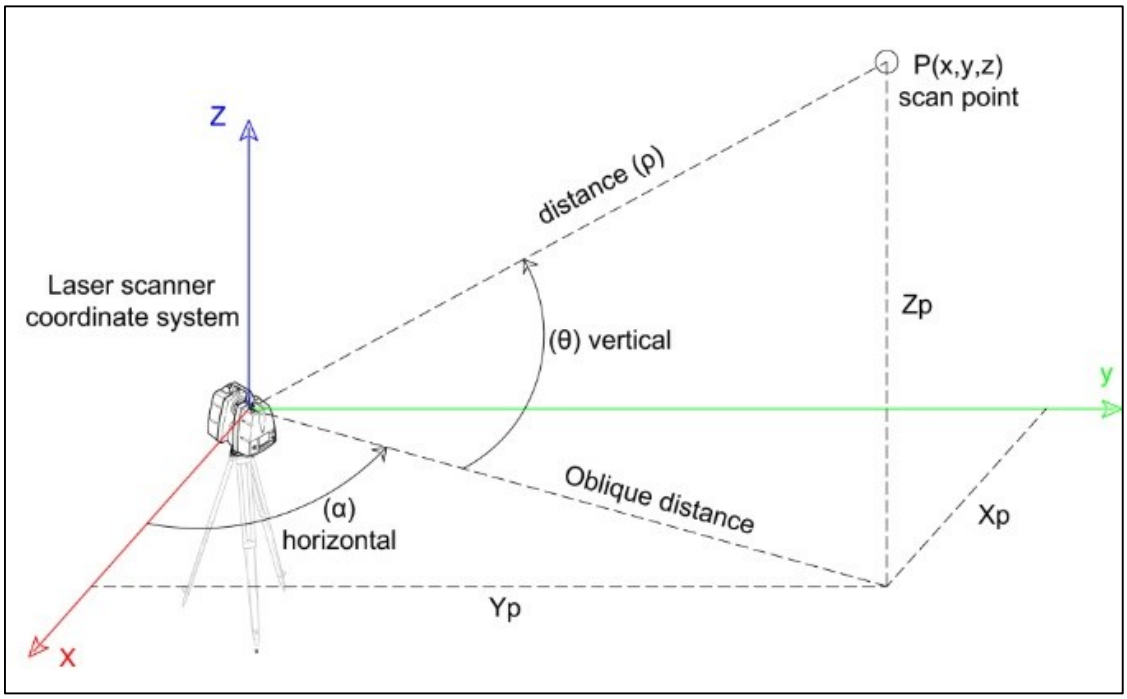

Figure 6: Measurements to find the coordinates of one targeted point. (Albourae, 2014)

Phased-shift laser scanners

Phase-shift laser scanners emit a continuous laser wave with a modulated frequency and wavelength. The wave reflects off objects in the environment and returns back to the scanner. The scanner then computes the phase shift of the returning wave and uses it to calculate the time of flight of the wave (Equation 3). Subsequently, the distance, vertical, and horizontal angles are computed using the time of flight (Wang, 2014). Finally, these values are plugged in Equation 2 to generate the Cartesian coordinates of the targeted point (Albourae, 2014). It is worth noting that

Phase-shift laser scanners are ten times faster than TOF laser scanners, however, they have limited range to around 130 m (Wang, 2014).

$$Time\ of\ flight = \frac{phase\ shift}{2\pi\ \times modular\ frequency} \qquad \text{Equation 3}$$

Post Processing

Laser scanners represent the environment's spatial information with a collection of 3D point coordinates (i.e., a 3D point cloud). Since 3D point clouds do not contain any color information, modern scanners are equipped with digital cameras that collect photos meanwhile scanning the environment. These photos are merged with the 3D point cloud to add texture to it and create a 3D photorealistic point cloud (see Figure 7; Leica Geosystems, 2012).

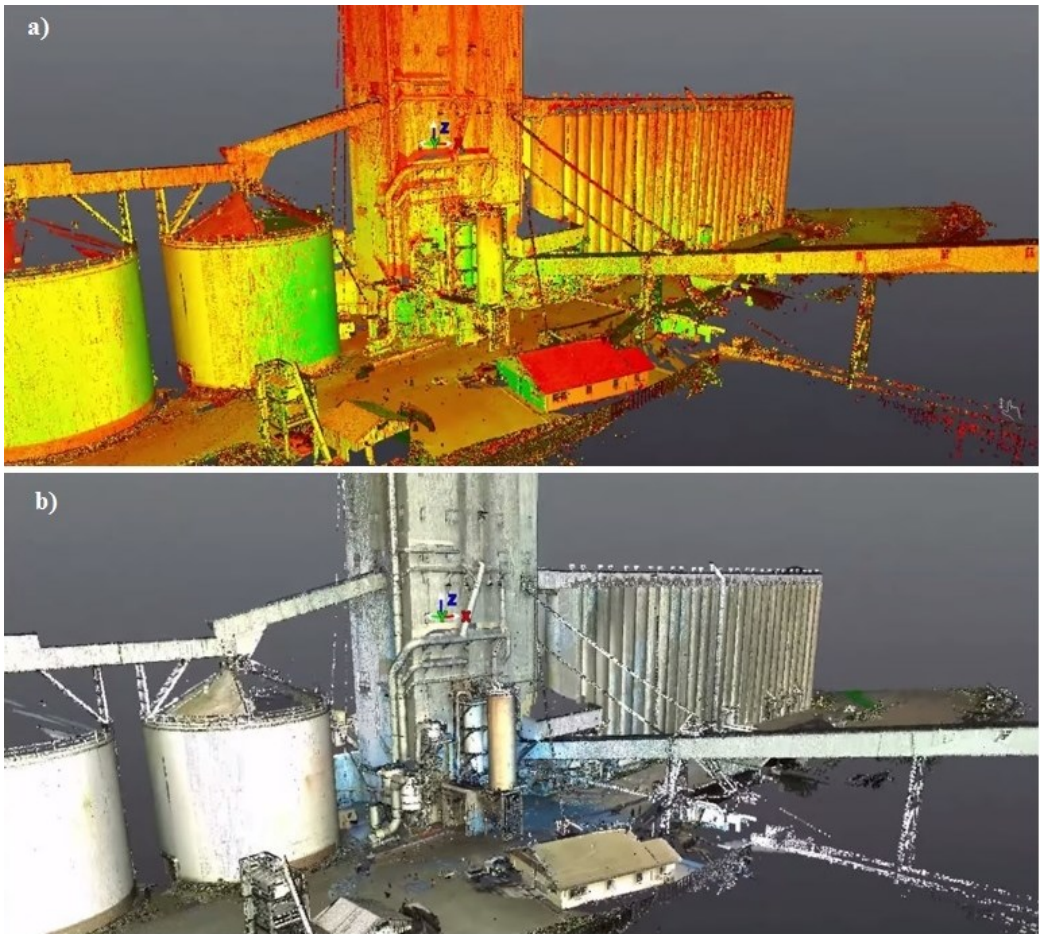

Figure 7: Point cloud from a laser scanner: a) Before merging the point cloud with digital photos, b) After merging the point cloud with digital photos. (Leica Geosystems, 2012)

Finally, to capture a facility/site completely, scans from different positions can be fused together in a process known as registration. Registration is a post-processing task, where point clouds from different scanning positions are registered in one common coordinate system (Jung et al., 2014; Tang et al., 2010). This is done by matching points that correspond in each point cloud being registered. The matched points can be checkerboard and/or spherical reference targets that were artificially implanted in the environment before scanning it. Features available in the environment (e.g., corners, door edges) can also be used for registration. The outcome of the registration process is one comprehensive point cloud that contains all the point clouds from the different scanning positions. In large scale facilities, setting up the scanner and its reference targets through the facility can take days of planning and execution (Klein et al., 2012; Qu et al., 2014).

Figure 8: Checkerboard reference targets

Figure 9: Spherical reference targets

Nowadays, laser-based remote sensing is the most reliable technique for the 3D modeling of spatial information (Klein et al., 2012; Qu et al., 2014). Mainly, this is because modern laser scanners are able to model the spatial information with dense point clouds with an accuracy of 2 to

5 mm (Qu et al., 2014). Nonetheless, laser scanners are still seldom used in the architecture, engineering, construction, and facility management (AEC/FM) industry (Klein et al., 2012; Qu et al., 2014). This can be regarded to several reasons. Firstly, laser scanning is time-consuming, because surveyors need to assemble the laser scanner and its reference targets in several parts of the facility to capture it completely. In large scale facilities, this might take days of planning and execution depending on the size and complexity of the facility (Klein et al., 2012; Qu et al., 2014). Secondly, the assembly and operation of the laser scanning equipment can only be conducted by highly trained professionals (Klein et al., 2012). Finally, and most importantly, laser scanning is extremely expensive because the scanning equipment costs tens of thousands of dollars (Klein et al., 2012; Qu et al., 2014). Alternatively, image-based remote sensing has been gaining popularity recently due to its affordability and simplicity (Klein et al., 2012).

2.2.3. Image-based Remote Sensing

In image-based remote sensing, a collection of overlapping images is used to 3D model the surrounding environment's spatial information (Westoby et al., 2012). The fundamental concept of image-based remote sensing is Stereophotogrammetry (Westoby et al., 2012). Stereophotogrammetry involves estimating the 3D coordinates of points that appear in two or more images that are taken from different positions (Thompson, 1966). The core principle of this approach is triangulation, in which the intersection of light rays coming from the different camera positions and converging on a common point, can be used to estimate the 3D coordinates of this common point (Dai & Lu, 2010; Warne, 2015).

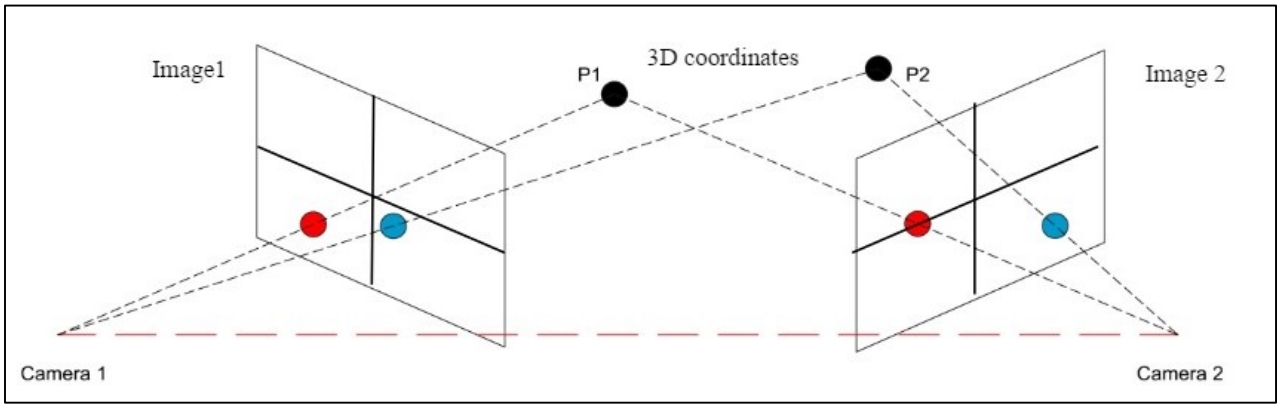

Figure 10: Concept of stereophotogrammetry. (Albourae, 2014)

To illustrate how stereophotogrammetry calculates the 3D coordinates of common points, a stereo normal case can be used. The conditions of a stereo normal case are as follows:

1- Images are taken at the same elevation (on the same plane).

2- Images are identically oriented.

3- Images are taken at same focal length.

In the following part, a stereo normal case example is used to highlight the basic concepts of stereophotogrammetry. It is worth noting that this example was adopted from a lecture by Prof. Cyrill Stachniss at the University of Bonn, Germany (Stachniss, 2015). And was solved with the aid of the manual of photogrammetry (Thompson, 1966).

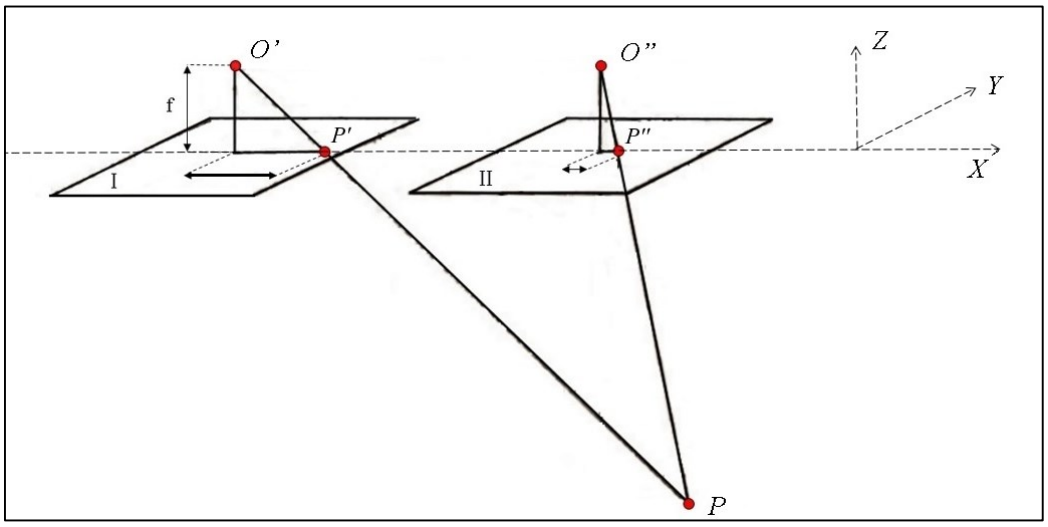

Figure 11: Stereo normal case example. (Stachniss, 2015)

Figure 11 shows two images in a stereo normal case, in which the images are taken at the same focal length **f**, at the same elevation, and at similar orientation. In other words, the images have equal Z & Y coordinates but different X coordinates. In Figure 11 the point ***P*** can be seen from both images (i.e., it is a matched point), it appears at point ***P'*** in the first image and at point ***P"*** in the second. ***O'*** and ***O"*** are the focal points for the first and second images, respectively. Since there is no transition on the Y-axis, then this problem can be converted into a 2D problem by ignoring the Y-axis.

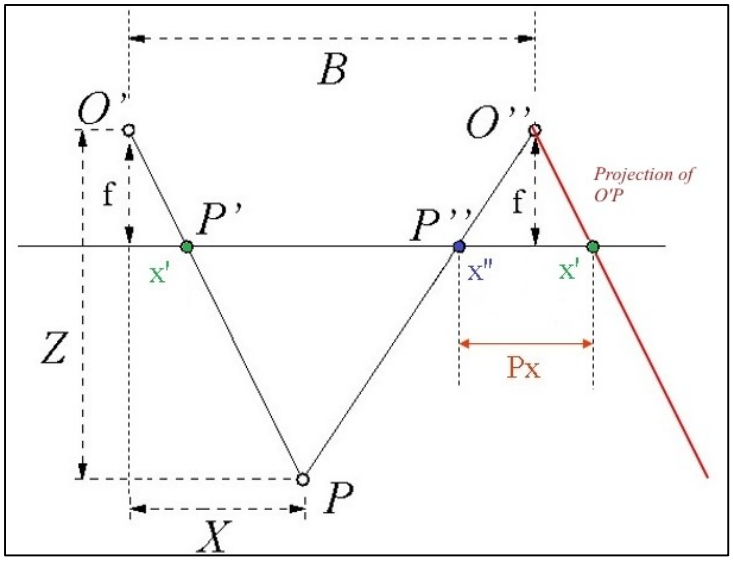

Figure 12: 2D problem after ignoring the Y-axis. (Stachniss, 2015)

Figure 12 displays the resulting 2D problem after ignoring the Y-axis. In Figure 12, ***B*** represents the distance between ***O'*** and ***O"***. ***x'*** and ***x"*** are the x-coordinates of the points ***P'*** and ***P"***, respectively.

To calculate the Z-coordinate of the point ***P***. First, the line ***PO'*** can be projected to the other side to the other side (as shown in Figure 12 in red color). Next, the Z-coordinate can be easily calculated using the intercept theorem:

$$\frac{Z}{f} = \frac{B}{Px} \qquad \text{Equation 4}$$

Where **Px** represents the parallax, which is the difference between the x-coordinates of the points ***P'*** and ***P"***. To get the Z-coordinate Equation 4 is multiplied by **f:**

$$Z = f\frac{B}{x' - x''} \qquad \text{Equation 5}$$

The intercept theorem is also used to calculate the X-coordinate of the point P:

$$\frac{Z}{X} = \frac{f}{x'} \qquad \text{Equation 6}$$

To get the X-coordinate, Z (from Equation 5) is plugged in Equation 6:

$$X = x'\frac{B}{x' - x''} \qquad \text{Equation 7}$$

This was a simplistic example of calculating point coordinates using stereophotogrammetry. More complex examples that include images taken at different 3D coordinates and different orientations can be found in the manual of photogrammetry (Thompson, 1966). However, this example was enough to illustrate the following:

1- The 3D coordinates of a point can be calculated if it corresponds in two of more images.

2- Calculating the 3D coordinates of a matched point depends on the location and orientation of each image taken.

Structure from Motion

In order to calculate the 3D coordinates of a point that corresponds to two or more images, the location and orientation of each image taken must be established. Traditionally, obtaining this information required attaching a GPS (for 3D coordinates) and an electronic compass (for orientation) to the camera (Westoby et al., 2012). However, in the modern photogrammetric algorithm known as Structure-from-Motion (SfM), the coordinates and orientation of each image taken are automatically calculated (Westoby et al., 2012). SfM not only converts 2D overlapping digital images into a 3D point cloud, but also automatically estimates the relative location and orientation of each image taken (Westoby et al., 2012). Therefore, SfM solves the problem of manually obtaining the 3D coordinates and orientation of each image (Westoby et al., 2012). 3D point cloud generation using the SfM algorithm involves the following steps: (1) image acquisition, (2) feature extraction and matching, (3) estimation of camera positions and orientations, and (4) 3D reconstruction.

Image acquisition

In the data acquisition stage, any type of digital camera is used to collect a set of overlapping images of the scene (see Figure 13; Westoby et al, 2012). Westoby et al. (2012) argued that an overlap of 80% or more must be maintained between images to enable feature extraction and matching. Moreover, Warne (2015) discussed that blurry images can cause distortion in the model since it is difficult to match pixel points across blurry images. Therefore, it is vital to keep the camera in focus during image acquisition. Furthermore, SfM is a passive sensing technique, in other words, it uses the light available in the scene. Thus, image acquisition can only be performed in properly illuminated areas (Bhatla et al., 2012). In addition, Westoby et al. (2012) recommend

collecting images at the highest resolution possible, because the resolution of the images directly affects the quality and density of the generated point cloud.

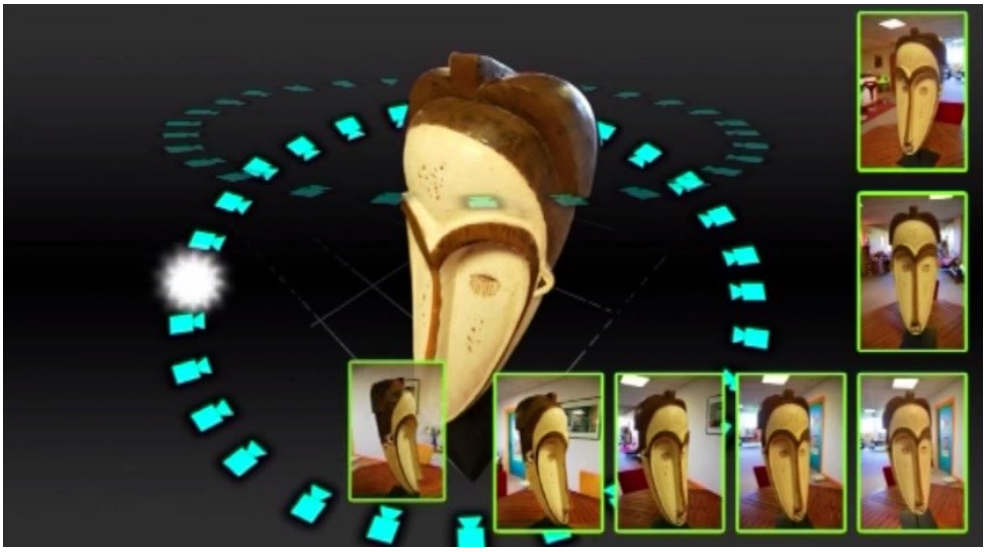

Figure 13: Acquisition of overlapping images. (Autodesk, 2013)

Feature extraction and matching

In the SfM algorithm, feature points are automatically extracted from the images using the Scale Invariant Feature Transform (SIFT) object recognition system that was developed by Lowe (2004). The feature points are represented by unique variations and contrast available in the images (Klein et al., 2012). Thus, the number of feature points detected in an image is highly dependent on the image texture and resolution. In other words, complex images that contain several details will return the most feature points (Westoby et al., 2012). After extracting the features, The SIFT algorithm also uses a *nearest neighbor* matching scheme to automatically match the feature points across the set of images (see Figure 14; Golparvar-Fard et al., 2011). This is also referred to photo stitching. In order for a feature point to be successfully matched, it must appear in at least 3 photographs (Westoby et al., 2012). Therefore, increasing the number of overlapping images increases the number of feature points matched, which can increase the density of the point cloud (Westoby et al., 2012). Finally, the output of this stage is a set of images that are matched together using the extracted feature points. These matched images are commonly referred to as stitched images.

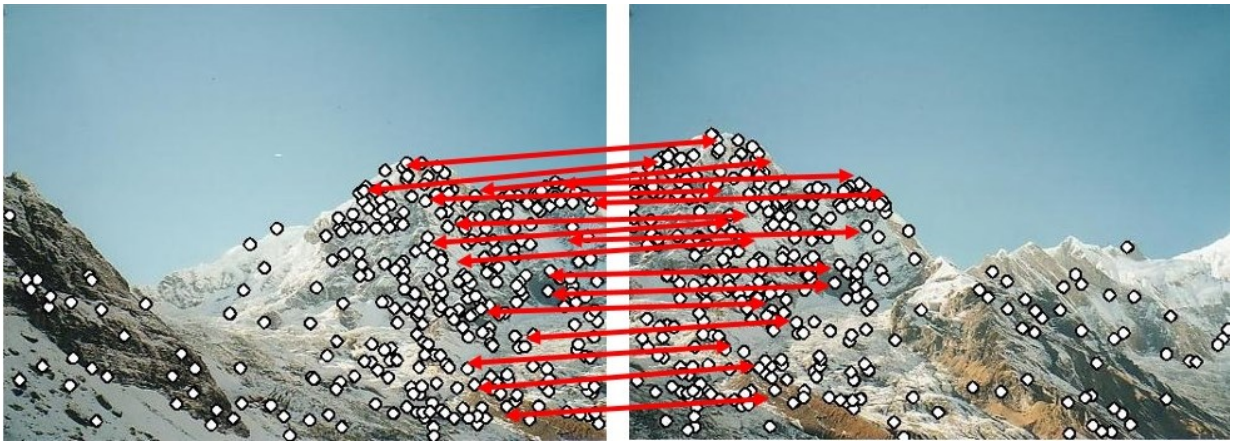

Figure 14: Feature point matching. (Stachniss, 2015)

Estimation of camera positions and orientations

After matching the feature points across the set of overlapping images, the camera position and orientation of each image can be estimated. This is done through a process known as bundle adjustment. The name "Bundle Adjustment" refers to *bundles* of light leaving each feature point and converging on the camera center, these bundles are then *adjusted* with respect to the feature points and the camera's positions (Triggs et al., 2002). Bundle adjustment uses a non-linear least squares to jointly optimize the camera parameters and the coordinates matched points (Snavely K. N., 2009; Triggs, McLauchlan, Hartley, & Fitzgibbon, 2002). The product of bundle adjustment is a sparse/low-density 3D point cloud, and the position and orientation of each image taken (see Figure 15; Bhatla et al., 2012; Westoby et al., 2012).

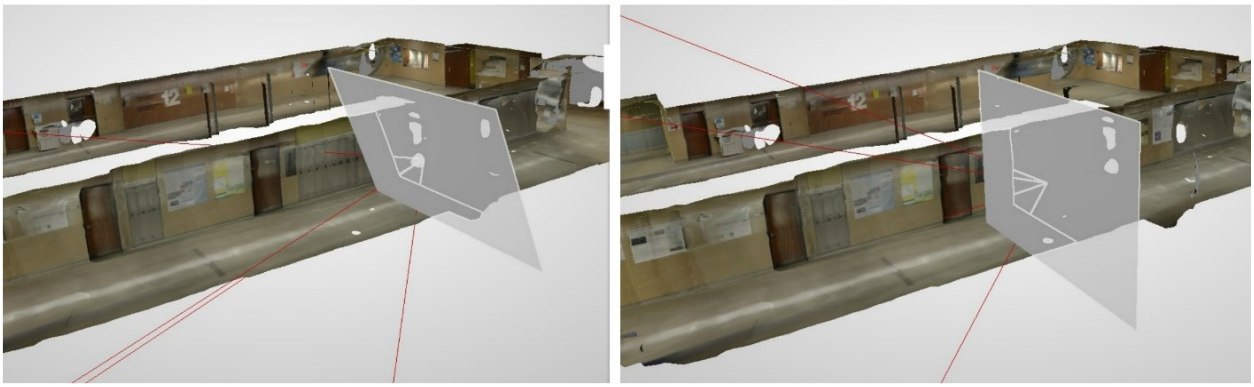

Figure 15: Product of the bundle adjustment.

3D reconstruction

After estimating the positions and orientation of each image, this information can be used to generate the 3D point cloud (Golparvar-Fard et al., 2011). This is achieved by triangulation, in which the intersection of light rays coming from the different camera positions, and converging on a common feature point is used to "triangulate" the coordinates of this point (see Figure 16-d; Dai & Lu, 2010; Warne, 2015). Finally, the outcome of this stage is a 3D textured point cloud (i.e., contains color information) that represents the spatial information of the scene.

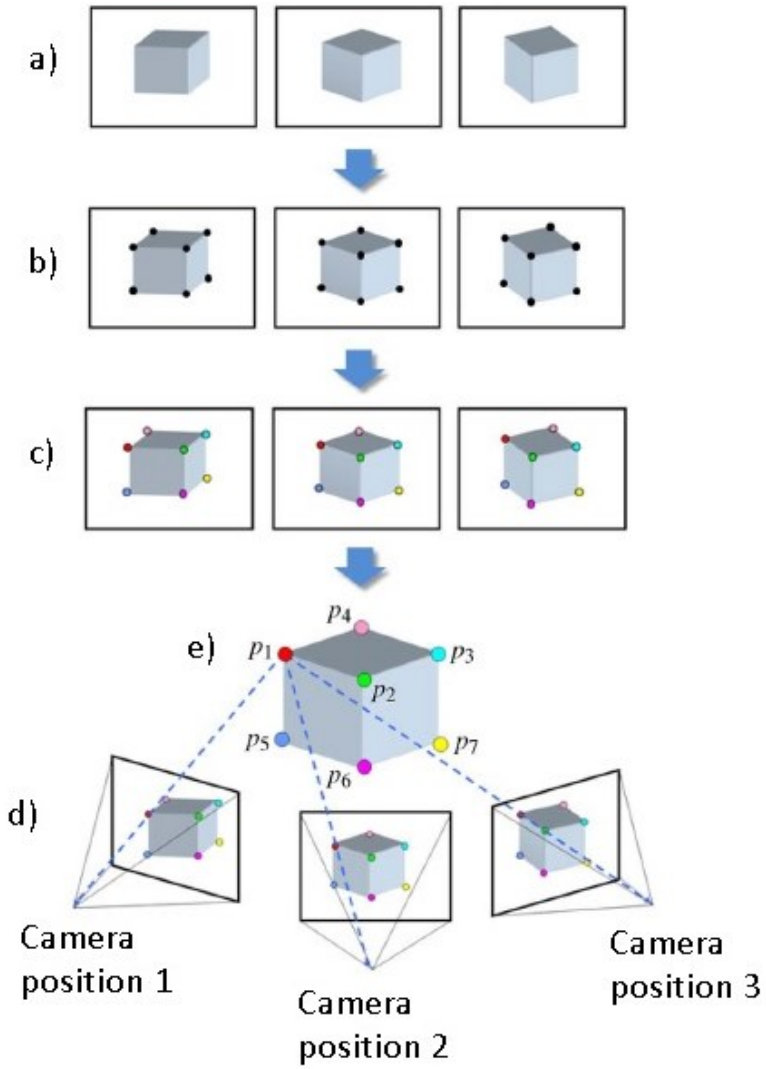

Figure 16: How point clouds are generated via SfM: a) acquisition of overlapping images, b) feature point extraction, c) feature point matching, d) camera position estimation, e) 3D point reconstruction. (Snavely, Simon, Goesele, Szeliski, & Seitz, 2010)

In recent years, numerous commercial software packages (e.g., Microsoft Photosynth, Autodesk Recap 360) that use SfM algorithms have appeared. These software packages offer full automation of the process, from feature point extraction to 3D reconstruction. Moreover, no specialized equipment are needed for this process since the only equipment needed is a digital camera. Therefore, SfM has made image-based sensing an affordable and user-friendly solution for the collection of spatial information (Klein et al., 2012; Qu et al., 2014).

Research work done on image-based remote sensing

The affordability and simplicity of image-based remote sensing have motivated several research groups to investigate the effectiveness of using this technique for the 3D modeling of spatial information. In one example, Klein et al. (2011) used an off-the-shelf 8 Megapixel camera and a commercially available software to model two heavily occluded rooms in a university building. The authors argued that using a heavily occluded space makes the experiment more realistic since removing furniture and other occlusions before starting the image acquisition process is impractical. To measure the accuracy of their models, Klein et al. (2011) manually measured the rooms with a laser distance measurer to serve as the ground truth. Finally, their test results show that the errors for image-based sensing fall within the range of centimeters, where the average deviation of their models from the ground truth was 4.52 cm. Moreover, in a more recent study conducted by the same author, Klein et al. (2012) used the same approach to model the exterior walls of a university building. To measure the accuracy in this case, Klein et al. (2012) choose 37 points on the surface of the exterior wall (such as façade openings) to serve as the control points. The authors then compared the coordinates of these point between the ground truth and the image-based models. In this case, the image-based models had a higher error, where the average deviation of the control points was 18.28 cm, 23.11 cm, and 11.78 cm on the X-, Y-, and Z-axis, respectively.

On a wider scale, Bhatla et al. (2012) tested the accuracy and reliability of image-based sensing using a 2000 ft under-construction bridge. To do this, the authors used an off-the-shelf DSLR camera, and the commercial software Autodesk Photofly to model 5 sections of the bridge. In this study, the test results yielded errors of up to 3.18 m. The authors attributed these inaccuracies to three main reasons. First, the presence of natural vegetation and ponds on site which prevented adequate image acquisition of the bridge. Second, the lack of texture and contrast on the surface of the bridge, which is vital for feature point extraction and matching. Third, the lack of well-defined

corners and edges in the bridge, which prevented accurate recognition of feature points and selection of reference points.

In another example of measuring the accuracy of the image-based sensing technique, Westoby et al. (2012) used a consumer-grade digital camera with their own SfM algorithm to model an 80m high coastal cliff. To measure the accuracy of their image-based point clouds, the authors also modeled the cliff using a laser scanner. The authors argued that the point clouds from a laser scanner are accurate enough to serve as the ground truth for their experiment. To measure the accuracy of the image-based point clouds, the authors subtracted the image-based point clouds from the laser-based point clouds. Their results indicated that 94% of the overlapping differences (between image- and laser-based point clouds) are within ±1m. In addition, their results also indicated that 86% of the overlapping differences were in the range of ±0.5m. Moreover, the authors argued that in vegetation-free areas the differences drop to ±0.1m

There are several types of digital cameras available on the market today. This has motivated researchers to find the minimum camera requirements needed for the image-based sensing technique. For example, Thoeni, Giacomini, Murtagh, and Kniest (2014) modeled a small rock wall in Australia using 5 different digital cameras and a laser scanner. The authors argued that this will establish the minimum camera requirements needed to obtain image-based models comparable to ones from a laser scanner. After generating the image-based point clouds from the cameras, they were compared to the laser-based point clouds from the laser scanner using a deviation analysis. The results obtained by Thoeni et al. (2014) suggests that a 9.5 Megapixel image sensor is enough to create image-based point clouds that are comparable to ones from a laser scanner.

One of the main limitations of image-based sensing is its inability to model featureless surfaces. Therefore, several recent research efforts focused on finding solutions for this limitation. On promising solution was recently presented by Tsai, Wu, Lee, Chang, and Su (2015). In their research, the authors presented an approach that uses both RGB-D and DSLR cameras to produce dense and complete (i.e., no voids in un-textured areas) point clouds. To test their approach, Tsai et al. (2015) used 4 RGB-D cameras (Microsoft Kinect) and 4 DSLR cameras to collect several overlapping images of a corridor in a university building. Subsequently, they used these images to generate two separate point clouds: (1) a point cloud from the DSLR images, (2) and another from the RGB-D cameras. These point clouds were fused together using the Helmert (7-parameter)

transformation. Tsai et al. (2015), then compared the fused point cloud (from RGB-D and DSLR images) with the DSLR point cloud. Their test results indicated the fused point cloud was in fact more complete and contained fewer voids, but it was less accurate than the DSLR point cloud. Namely, the fused point cloud had an average deviation of 1.62 cm from the ground truth, while the DSLR point cloud had an average deviation of 0.86 cm.

2.2.4. Comparison Between Remote Sensing Techniques

Image- and laser-based remote sensing are two very different techniques for the 3D modeling of spatial information. Although laser scanners use accurate and dense point clouds to model the spatial information, image-based sensing can do so with sufficient accuracy and density, but for a fraction of the cost. These differences have recently encouraged several research groups to compare laser- and image-based sensing techniques. For example, Klein et al. (2012) and Bhatla et al. (2012) conducted a qualitative comparison between image- and laser-based sensing technologies. According to Klein et al. (2012) and Bhatla et al. (2012), laser scanners model the spatial information within an accuracy of millimeters, while image-based sensing has an accuracy within centimeters. Also, the authors stated that laser-based point clouds are denser than image-based point clouds. Moreover, Klein et al. (2012) stated that image-based sensing has three advantages over laser-based sensing. First, image-based sensing is by far more affordable than laser-based sensing. This is mainly because laser scanners cost tens of thousands of dollars while digital cameras are fairly inexpensive. Second, image-based sensing is user-friendly, while laser-based scanning is not. Because the laser scanning equipment can only be operated by professional surveyors. Third, image-based sensing is portable since it is conducted using handheld digital cameras. On the other hand, laser scanners are bulky and must be placed on a tripod.

Other researcher works included a quantitative comparison between image-based and laser-based sensing techniques. For instance, Golparvar-Fard et al. (2011) measured and compared the accuracy of both sensing techniques. In doing so, the authors used a Nikon D80 and their own SfM algorithm to model a concrete column and a masonry block at 8 different situations, including: (1) indoor masonry block while the camera resolution was set to 2323×1555 pixels; (2) indoor masonry block @ 3872×2592; (3) outdoor masonry block @ 1162×778; (4) outdoor masonry block @ 1936×1296; (5) outdoor construction column @ 2323×1555; (6) outdoor construction column @ 3872×2592; (7) indoor construction column @ 2323×1555; (8) indoor construction column @

3872×2592. They also used a laser scanner to model the same concrete column and masonry block. The end result was 8 image-based point clouds, and 4 laser-based point clouds. To compare the accuracy of both types of point clouds, the authors converted all these point clouds into 3D CAD objects. Golparvar-Fard et al. (2011) then compared the dimensions of the CAD objects with the actual dimensions of the concrete column and masonry block. Specifically, they calculated the X/Y, Y/Z, and X/Z ratios for the CAD objects and got the percentage error for each ratio using the actual X/Y, Y/Z, and X/Z ratios. Their results indicated that laser scanning is always more accurate than image-based sensing. Still, the results of the image-based sensing technique were satisfactory. For instance, with respect to the indoor masonry block with images set to 3872×2592 pixels, the percentage errors for X/Y, Y/Z, and X/Z were 1.53%, 1.66%, and 0.00%, respectively.

A more comprehensive quantitative comparison between image- and laser-based sensing techniques was conducted by Dai, Rashidi, Brilakis, and Vela (2012). In their study, the researchers compare image- and laser-based sensing techniques in terms of accuracy, density, time, and cost. To do this, Dai et al. (2012) used 3 infrastructure objects as case studies. Specifically, they modeled the surfaces of a concrete beam, a concrete building, and an arch bridge using digital cameras and free image-based modeling software. They also modeled the test objects using a laser scanner. To get the ground truth model needed for the accuracy comparison, the researchers used a total station to get the 3D coordinates of the edges of the test objects. They then rendered the surface of the ground truth models using the Poisson surface reconstruction algorithm. With respect to their accuracy analysis, the image-based point clouds had an average deviation of 9.34 cm from the ground truth, which was significantly more than that of the laser-based point clouds (0.58 cm). Moreover, when the density was compared, the laser-based point clouds turned out to be significantly denser that image-based point clouds. The authors claimed that the image-based point clouds had low density because the surfaces of the test objects had a low number of features available. Additionally, when the comparison was done in terms of cost, the results revealed that the average cost spent on constructing the image-based point clouds ($1081) was a fraction of what was spent on the laser-based point clouds ($100,140). Finally, the results of the time-based comparison indicated that image-based sensing is more time-efficient with regards to the time needed for the on-site data collection. On the other hand, the laser-based approach was more time-efficient with respect to the time needed for processing the point clouds. Dai et al. (2012) claimed

that the time needed for processing the image-based point clouds considerably increased as the number of images increased.

2.3. Unmanned Aerial Systems

According to the international association of Unmanned Vehicle Systems (UVS international), Unmanned Aerial Systems (UAS) are generic aircrafts designed to operate with no human pilot. Along with the term UAS, other terms like Remotely Piloted Vehicle (RPV), Drone, and Unmanned Aerial Vehicle (UAV) are commonly found throughout literature (Remondino, Barazzetti, Nex, Scaioni, & Sarazzi, 2011). UAS are best known for their military applications such as unmanned aerial surveillance, reconnaissance and target assassination. Therefore, it is no surprise that UAS have military origins. They were first used by the US military in the Vietnamese war in the early 1970s, and by the Israeli military in the October war in 1973 (Colomina & Molina, 2014). Academically, a few research groups realized the potential of using UAS for civilian applications in the late 1970s. However, their ideas didn't get enough recognition at the time, due to the difficulty of acquiring UAS at the time (Colomina & Molina, 2014). With recent technological improvements, UAS have become widely available to the public at an affordable price (Siebert & Teizer, 2014). Thus, UAS are now being used in several civilian applications, such inspections, agricultural analysis, surveying, and many more.

2.3.1. System Configurations

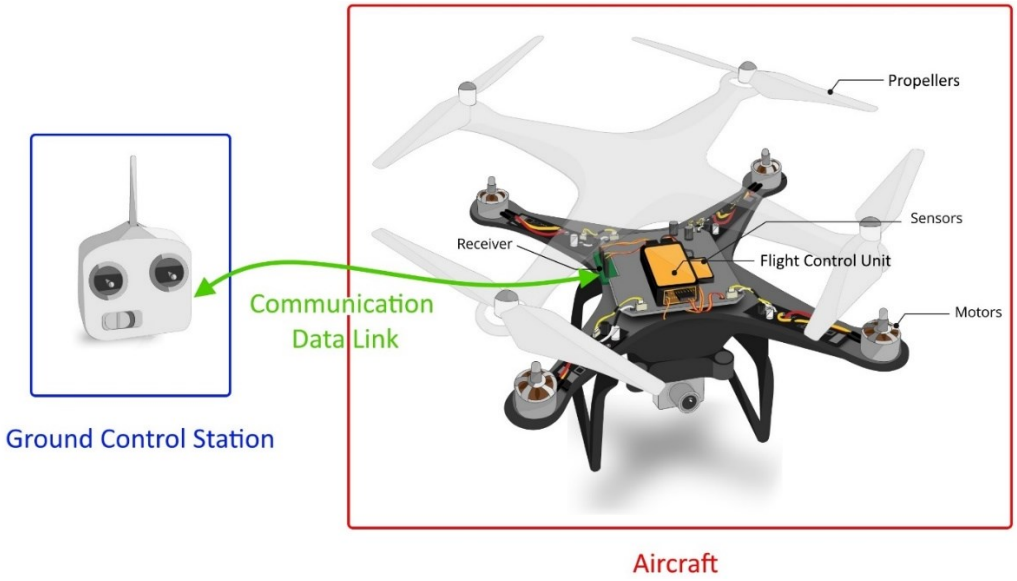

Figure 17: Main components of a UAS. (McDougal, 2015)

Three main components make up a UAS: (1) the ground control station, (2) the communication data link, and (3) the aircraft (see Figure 17; Colomina & Molina, 2014). The ground control station (see Figure 18) is the device used to control and monitor the aircraft, this device can be stationary or transportable (Colomina & Molina, 2014). The communication data link is the connection between the aircraft and the ground control station. It is a crucial part of the system since it is the only way to communicate with the aircraft and control it (Colomina & Molina, 2014). Several communication techniques are available for a modern UAS, but for a small non-military UAS Wi-Fi 2.4 GHz is a common choice (Colomina & Molina, 2014). The aircraft is the main component of a UAS. It receives the commands from the ground control station through the receiver and sends them to the Flight Control Unit (FCU). Sensors (e.g., Inertial Measurement Unit, Gyroscope) calculate the necessary flight information (e.g., acceleration, orientation, alignment) and sends them to the FCU (Siebert & Teizer, 2014). The FCU receives the information from the sensors, and the commands from the receiver, and uses them to navigate the aircraft using the motors and propellers (Siebert & Teizer, 2014).

Figure 18: Ground control station.

There are mainly two types of UAS: fixed wing UAS, and rotary-wing UAS (Siebert & Teizer, 2014). Fixed wing UAS offer more airtime and less noise than rotary-wing UAS. Therefore, they are very suitable for applications such as surveillance and reconnaissance (Siebert & Teizer, 2014). However, they are not very maneuverable and need an airstrip for takeoff and landing

(Siebert & Teizer, 2014). Rotary wing UAS don't need an airstrip for takeoff and landing. In addition, they are very suitable for confined spaces as they are stable, maneuverable, and easy to operate (Eisenbeiß, 2009; Siebert & Teizer, 2014).

Colomina and Molina (2014) have split modern UAS into three main categories depending on their operation range and maximum takeoff weight. These three main categories include nono-micro-mini UAS, close-short-medium range UAS, and the remaining UAS. Of the three categories, nano-micro-mini UAS have the shortest operation range and the lowest maximum takeoff weight. Specifically, mini UAS can only operate within a distance of 10 km or less from the ground control station, and have a maximum takeoff weight of 30 kg (Colomina & Molina, 2014). Close-short-medium range UAS can operate within 70 km or less from the ground control station, and have a maximum takeoff weight between 150 and 1250 kg (Colomina & Molina, 2014). The remaining UAS have an operation range of over 70 km, where these UAS are only operated by special governmental teams (e.g., military forces; Colomina & Molina, 2014).

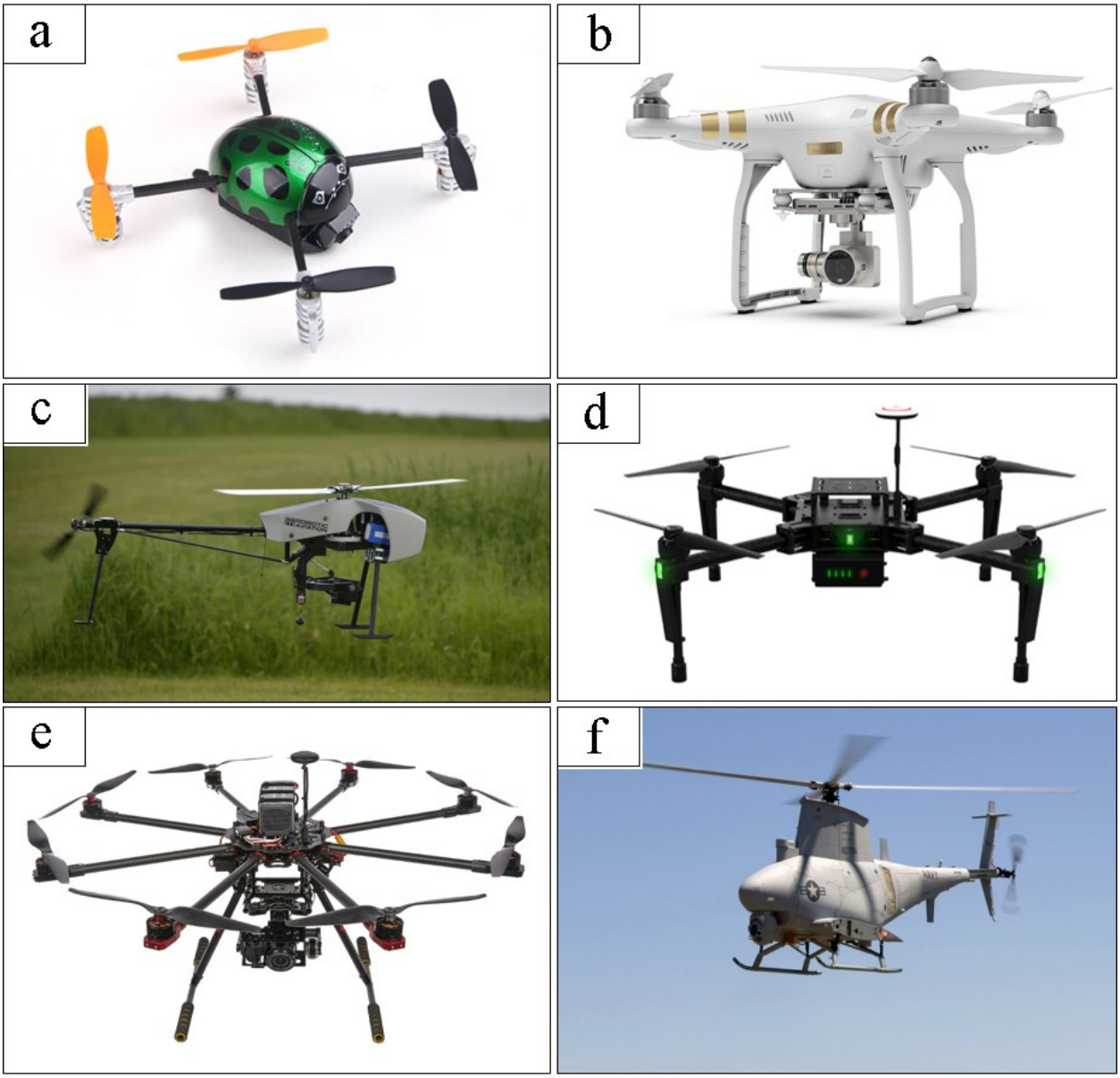

Figure 19. Rotary wing UAS: a) QR Ladybird V2 by Walkera, b) Phantom 3 Professional by DJI, c) Responder by ING Robotic Aviation, d) Matrice 100 by DJI, e) Octocopter Hawk F900 RTF by SkyhawkRC, f) MQ-8B Fire Scout by USAF (United States Air Force). (http://www.dronelife.com)

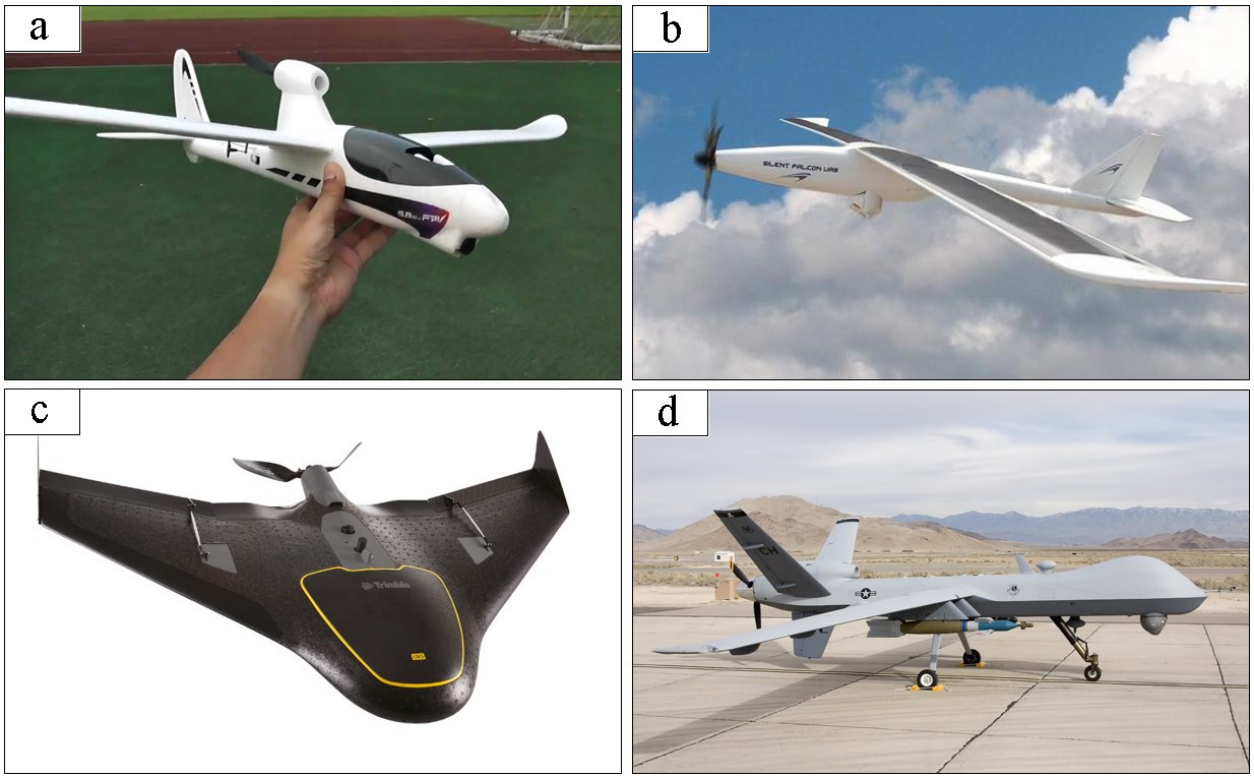

Figure 20. Fixed wing UAS: a) SPY HAWK by Hubsan, b) Silent Falcon by Silent Falcon UAS, c) UX5 Aerial Imaging Solution by Trimble, d) General Atomics MQ-9 Reaper by USAF. (http://www.dronelife.com)

Recent market analysis indicates that UAS are becoming increasingly popular worldwide. According to a study by MarketsandMarkets (2014), the UAS market is expected to grow from $6,762 million in 2014 to $10,573 million by 2020. Moreover, UAS have also been gaining popularity academically. For example, the number of papers submitted to the International Society for Photogrammetry and Remote Sensing (ISPRS) congress has doubled between 2008 and 2012 (Colomina & Molina, 2014). Perhaps this increased popularity can be attributed to the numerous advantages of UAS. Eisenbeiß (2009) outlined a number of benefits that can be gained from using UAS:

1. UAS can be used in risky and dangerous situations without endangering human life.
2. Since UAS have become smaller in size, they can be used in confined environments and inaccessible locations.
3. UAS are not burdened with the physiological limitations and economical expenses associated with on-board human pilots.

4. UAS can collect data in real-time by transmitting live video (or images) to the ground control station.

2.3.2. Applications

Recent technological developments have made modern UAS more efficient in terms of size, cost, payload capacity, and flight performance. In addition, with the arrival of lightweight and cost-efficient equipment (e.g., GPS, digital cameras) UAS have become an effective and cost-efficient tool for remote image acquisition (Siebert & Teizer, 2014). Consequently, UAS are currently being used in a range of engineering applications, including but not limited to:

Inspections

A camera mounted on a UAS can be used for the inspection of hazardous and inaccessible equipment (e.g., wind turbines, power lines, bridges, solar panels; AIBOTIX, 2015). For instance, Metni and Hamel (2007) used a UAS for monitoring and maintaining bridges and structures.

Disaster response and prevention

With the help of UAS, natural disasters can be monitored and detected. For example, Rufino and Moccia (2005) equipped a fixed-wing UAS with a hyperspectral camera to monitor and detect forest fires. Also, the UAS can be used in the detection of landslides. This was investigated by many research works such as the ones done by Carvajal, Agüera, and Pérez (2011), Joswig (2011), Niethammer, Rothmund, Schwaderer, Zeman, and Rau, Jhan, Lo, and Lin (2011).

Agriculture analysis

Vegetation control is usually performed via satellite imagery. However, UAS-imagery can be a cost-effective solution for the collection of information from agricultural fields (Colomina & Molina, 2014; Remondino et al., 2011). For example, Remondino et al. (2011) used a UAS to collect aerial images of a wine yard in the visible and Near-Infrared (NIR) spectrums. They then used these images to derive the Normalized Difference Vegetation Index (NDVI), which helped study the health and cultivation of the wine yard.

Surveying

Surveying and 3D mapping using UAS-imagery are currently being investigated to replace traditional surveying techniques because of the wide range of benefits that can be achieved with it. For example, Siebert and Teizer (2014) developed a system that uses UAS-imagery and a SfM software (i.e., Agisoft PhotoScan) to generate 3D mapping data and Digital Elevation Models (DEMs). After testing their system on several earth moving construction sites, the authors claimed that their system can collect 3D mapping data quickly and autonomously with acceptable accuracy. Moreover, Siebert and Teizer (2014) explained that accurate cut and fill information can be easily extracted from the DEMs generated by their system. As a result, quantity takeoff for excavation and backfilling can become faster, easier and more precise. Furthermore, the Siebert and Teizer (2014) outlined several benefits that can be achieved when UAS-imagery is used for surveying and 3D mapping instead of traditional techniques. Such as, cost saving, faster data acquisition, safer surveying of dangerous locations, and easier surveying of inaccessible locations (e.g, quarries, landfills).

Image-based modeling using UAS-imagery

Preservation of archeological and cultural heritage sites is extremely expensive. Several countries don't have enough money to preserve their cultural sites (Eisenbeiß, 2009). Consequently, many sites are often left to decompose without having any documentation at all (Eisenbeiß, 2009). High-resolution documentation of cultural heritage is highly important for scientific and tourism purposes (Eisenbeiß, 2009). Therefore, this has stimulated quite a few researchers to use UAS-imagery and image-based sensing techniques for the documentation of cultural heritage. For example, Remondino et al. (2011) used a UAS to capture 100 top view images of an archeological site in Veio, Italy. They then converted these images into a dense 3D point cloud using an open source SfM software tool to document the archeological site.

Image-based modeling using UAS-imagery can also be used for creating 3D city models. 3D city models can be used for various applications (e.g., city planning, damage assessment, digital tourism, architecture; Wefelscheid, Hänsch, & Hellwich, 2011). The main advantages of using a UAS for the creation of 3D city models are the ability to (1) capture a large amount of information efficiently, and (2) capture information from inaccessible locations (e.g., top of skyscrapers; Colomina & Molina, 2014). Consequently, UAS are currently being testing and implemented in

the generation of 3D city models. For example, Xie, Lin, Gui, and Lin (2012) mounted a fixed-wing UAS with four Cannon EOS 5D Mark II cameras to collect aerial images of city buildings. The authors argued that the combination of four cameras ensured that every part of the surveying area was captured in four or more images. Xie et al. (2012) tested their approach on two university building in China and claim that it improved the speed and accuracy of 3D building modeling.

2.4. Research Gap

The 3D modeling of indoor building environments using image-based sensing techniques has been investigated by several researchers, such as Klein et al. (2012) and Golparvar-Fard et al. (2011). Nonetheless, to the author's best knowledge these research efforts only studied the feasibility of modeling single entities (e.g., one masonry block, room). This is not enough because as-built 3D models used for facility management operations should represent the facility completely with all of its components. Therefore, to represent a more realistic situation of modeling indoor building environments, a closed-loop environment of four corridors will be chosen as a testing environment for this research. Furthermore, modeling a closed-loop environment takes into account the residual errors, which result from the accumulation of errors throughout the modeling process (see Figure 21). This cannot be achieved if only single entities are modeled.

Moreover, recent technological advancements have made modern UAS efficient in terms of size, cost, and payload capacity. Additionally, the combination of UAS with lightweight high definition cameras has made modern UAS a cost-effective solution for remote image acquisition. Consequently, several researchers in recent years have used UAS for a variety of engineering applications (e.g., inspection, disaster response and prevention, agricultural analysis, surveying). However, to the author's best knowledge, no existing UAS-based research studies have focused on investigating whether images captured remotely by a UAS can be used to model the spatial information of indoor building environments. Both gaps will be addressed in this research thesis.

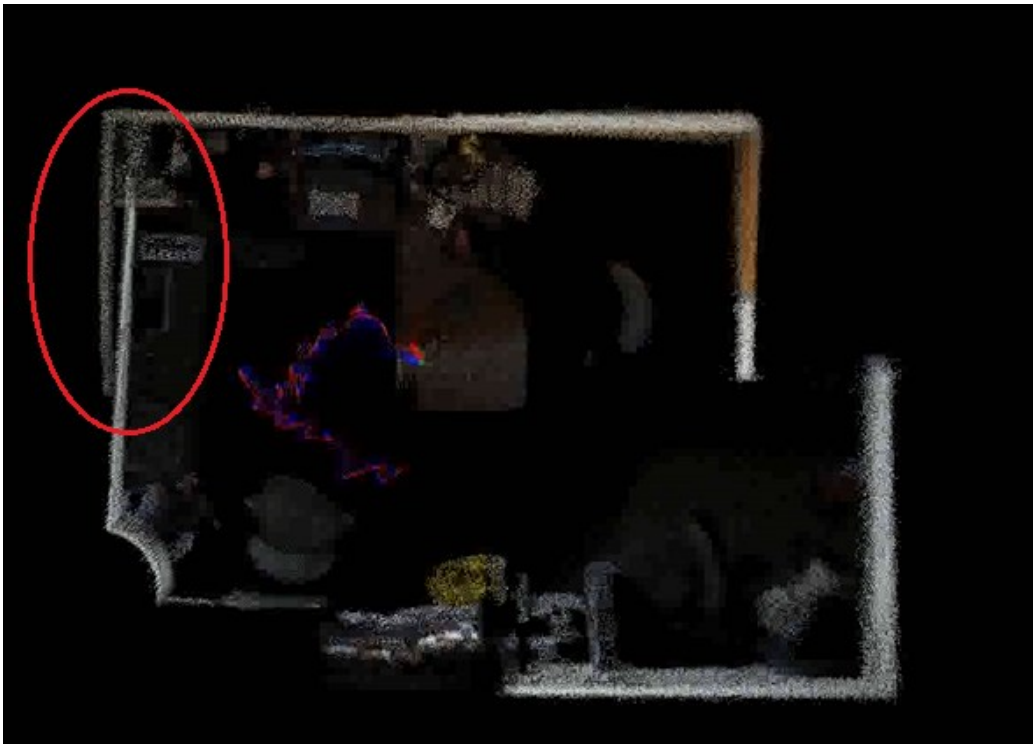

Figure 21: Example of residual error.

CHAPTER 3: METHODOLOGY

3.1. Overview

The first objective of this research is to test the feasibility of using a UAS for the 3D modeling of indoor building environments. To accomplish this, a commercial-grade UAS and a SfM 3D modeling software will first be selected. This equipment and software will be used to model typical indoor building environments in order to test the feasibility of using a UAS for the 3D modeling of spatial information. The 3D modeling of indoor building environments has been studied by several researchers, such as Klein et al. (2012) and Golparvar-Fard et al. (2011). However, to the author's best knowledge these research efforts only studied the modeling of single entities (e.g., one masonry block, room). This is not enough because as-built 3D models used for facility management operations should represent the environment in its entirety with all of its components. Therefore, to have a realistic test-bed, a closed-loop indoor building environment of four corridors will serve as the testing environment in this research. After choosing the testing environment, the UAS will be used to collect several overlapping images of this environment. The set of images will then be processed by the 3D modeling software to generate a UAS-based 3D point cloud of the testing environment. The lessons learned and issues encountered while constructing this UAS-based point cloud will be outlined and discussed to highlight the feasibility of modeling indoor building environments using a UAS. Subsequently, in order to evaluate the effectiveness of using a UAS for the 3D modeling of indoor building environments, the UAS-based point cloud will be compared to a laser-based point cloud from a laser scanner. This comparison will be done in terms of accuracy, density, cost, and time. The first step in doing this comparison is to align both types of point clouds (the UAS-based and laser-based point clouds) in a common coordinate system. To accomplish this, control points must be implanted in the environment before data collection begins. Then, the control points can be matched between the different point clouds to register them in a common coordinate system. After aligning the clouds in a common coordinate system, their accuracy and density will be compared. In addition, the time and cost information will be recorded while constructing the point clouds, and will be used to perform a time- and cost-based comparison between both modeling techniques. Finally, the results of this comparison will be used to highlight the advantages and limitations of modeling indoor building environments using a UAS. Figure 22 displays a flowchart of the methodology followed in this research.

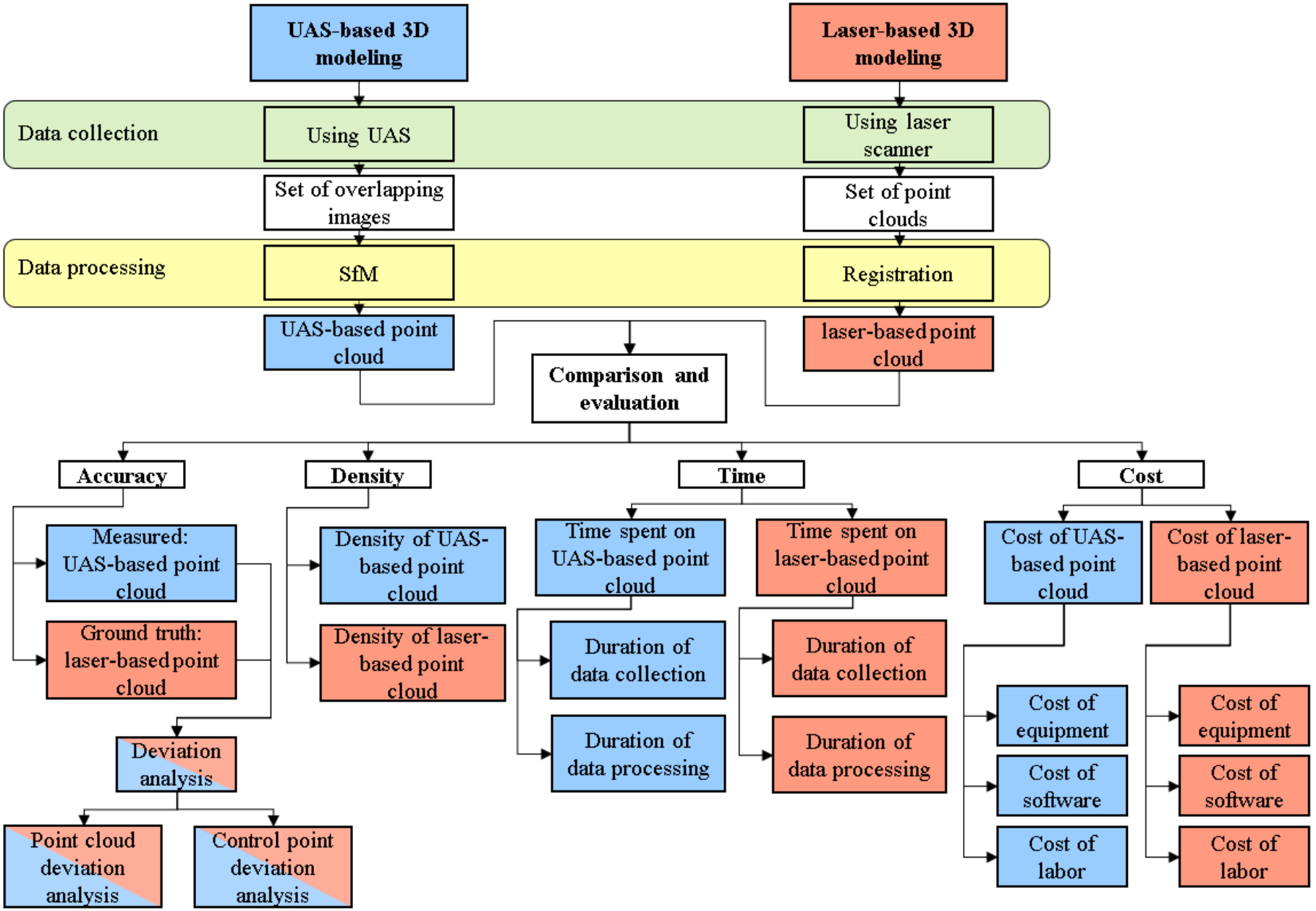

Figure 22: Research methodology flowchart.

3.2. UAS-based 3D Modeling

The first step towards constructing the UAS-based point cloud is hardware selection. Since there is an abundant number of UAS available in the market today, certain requirements must be established for selecting an appropriate UAS. First, it should be small in size since it will be used in confined spaces and maneuvered between tight corners. Second, the UAS should have an appropriate camera sensor. Previous research by Thoeni et al. (2014) indicated that in order for the SfM algorithm to give appropriate results, the image sensor must be at least 9.5 Megapixels. Moreover, since the images will be collected aerially there is a high probability that they will be blurry. Blurry images can cause distortion in the point cloud. Therefore, the camera should also have image stabilization capabilities. Third, the UAS should have live-streaming capabilities, in order to capture the images remotely. Finally, a UAS with an appropriate battery should be selected in order to conduct the image acquisition without any interruptions.

After selecting an appropriate UAS, it will then be used to generate the UAS-based 3D point cloud. To accomplish this, visual markers are first added to areas where there are an insufficient number of features (e.g., a drywall with one solid color and no decorations). This is necessary because the SfM algorithm depends on the number of features available in the environment to model it completely. Therefore, visual markers must be placed on featureless surfaces before data collection starts to artificially increase the number of features available, and ensure adequate modeling of these surfaces. Thereafter, the UAS will be used to collect overlapping images of the testing environment. An overlap of 80% or more should be maintained during the image acquisition, to ensure that there is a proper matching of features between the images. After image acquisition is completed, irregularities such as moving objects (e.g., people passing) as well as blurry images, which can cause distortions in the point cloud, will be manually removed from the images. Afterward, a SfM 3D modeling software is used to process these images and automatically generate the UAS-based 3D point cloud. The SfM algorithm begins by identifying the feature points available in the images using the Scale Invariant Feature Transform (SIFT) object recognition system. The nearest neighbor matching scheme is then used to match these feature points between the different overlapping images. The matched points are then used to approximate the position and orientation of each image taken using a highly iterative algorithm known as

'bundle adjustment'. Finally, the estimated camera positions and orientations are used to generate the UAS-based point cloud by triangulating the 3D coordinates of the matched feature points. After the UAS-based point cloud is generated, it can be scaled by manually defining a well-known dimension in it.

3.3. Laser-based 3D Modeling

Nowadays, laser scanning is the most reliable remote sensing technique for the 3D modeling of spatial information (Bhatla et al. 2012; Golparvar-Fard et al. , 2011; Klein et al., 2012). Therefore, to evaluate the effectiveness of modeling indoor building environments using a UAS, the UAS-based 3D modeling approach will be compared to laser scanning. To this end, a laser scanner is deployed in several locations throughout the testing environment. The raw scans from the different scanning positions are then registered in a common coordinate system to create one 3D point cloud of the testing environment. Finally, the registered point cloud is cleaned from any unwanted points, which will then be used in the comparison and evaluation stage.

3.4. Comparison and Evaluation

One of the main objectives of this research is to evaluate the effectiveness of 3D modeling indoor building environments using a UAS. To achieve this, a typical closed-loop indoor building environment is modeled using a UAS and a laser scanner. Both modeling approaches will then be compared in terms of accuracy, density, time, and cost.

3.4.1. Accuracy

Laser scanners have been reported to have an accuracy of around 2-5 mm (Qu et al., 2014; Thoeni et al., 2014). Therefore, the laser-based point cloud from the laser scanner can be used as the ground truth in measuring the accuracy of the UAS-based point cloud. However, before the laser-based point cloud is declared the ground truth, its accuracy should be validated. In doing so, a laser distance measurer can be utilized for measuring the actual dimensions of the testing environment, in order to validate the accuracy of the laser-based point cloud.

After validating the accuracy of the laser-based point cloud, it will be used as the ground truth in measuring the accuracy of the UAS-based point cloud. The first step towards measuring the accuracy of the UAS-based point cloud involves aligning it in a common coordinate system

with the laser-based point cloud (i.e., the ground truth point cloud). This can be achieved by matching control points (i.e., targets placed in the environment before any data collection takes place) that correspond to each point cloud. After aligning the clouds in a common coordinate system, a deviation analysis is conducted to measure the accuracy of the UAS-based clouds. The deviation analysis is conducted on two levels: (a) a point cloud level and (b) a control point level.

Point cloud deviation analysis

In the point cloud deviation analysis, the distance between each point in the UAS-based cloud and its hypothetical corresponding location in the ground truth point cloud is calculated. Since it is impossible to know the actual location of the measured point in the ground truth point cloud, the distance is calculated from the nearest point. In order to have more accurate results, a local modeling strategy can be followed. Using this strategy, the ground truth point cloud is modeled using a quadratic function that will fit a plane on the nearest point and several of its neighbors. The deviation distance will then be measured from the measured point **P** (in the UAS-based cloud) to the modeled plane (see Figure 23). This strategy is statistically more accurate than measuring the deviation from point to point (CloudCompare, 2015).

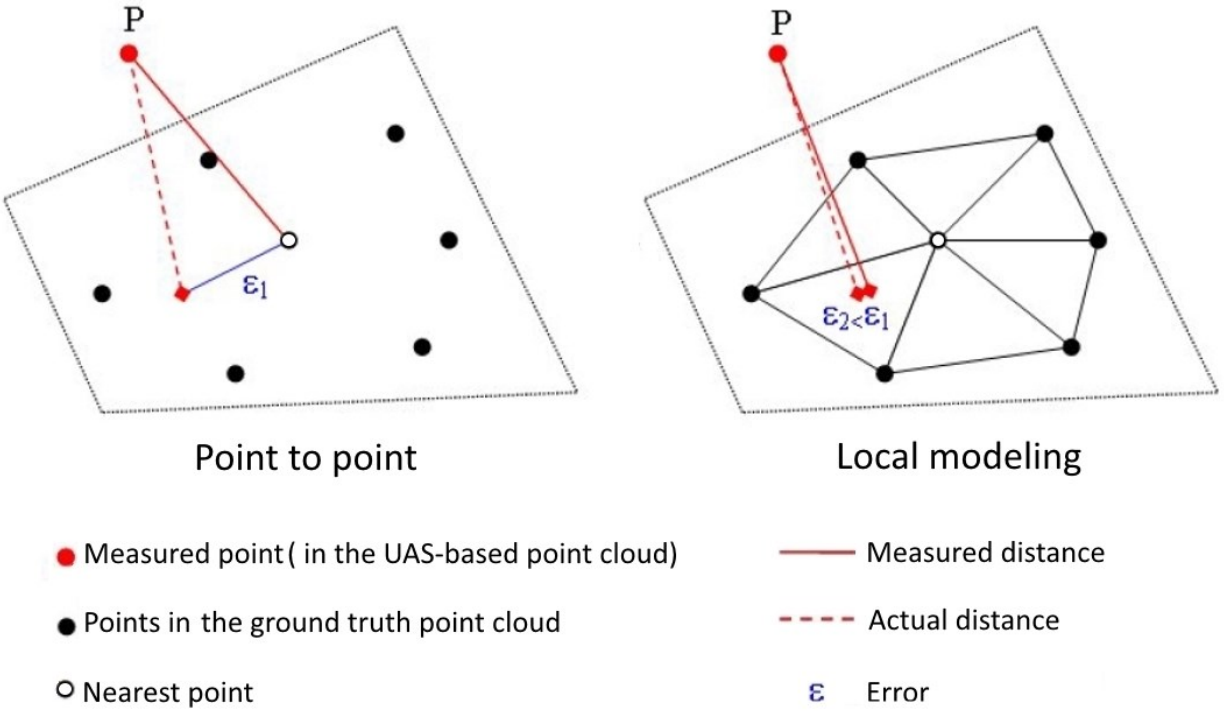

Figure 23: Point to point versus local modeling. (CloudCompare, 2015)

Control point deviation analysis

The point cloud deviation analysis is vital for measuring the accuracy of the UAS-based cloud. This is because it can help identify which areas have the most errors, and is a good overall estimation of the accuracy. However, it is still an approximation of the accuracy. This is partly because in the point cloud deviation analysis, the deviation is measured between the measured point (in the UAS-based point cloud) and it hypothetical corresponding location in the ground truth point cloud. As such, the corresponding point can never be exactly identified. Therefore, to get more accurate results the control point deviation analysis can be used. To conduct a control point deviation analysis, control points are first placed in various locations throughout the testing environment before any data collection occurs. Later, after generating the UAS-based point cloud and the ground truth point cloud, the difference in the coordinates of the control points will be computed (see Equation 8, Equation 9, and Equation 10). Additionally, these coordinates will be used to compute the absolute distance between the location of the control points in the ground truth point cloud and their location in the UAS-based point cloud (see Equation 11).

$$\Delta X = X_{ground\ truth\ cloud} - X_{UAS-based\ cloud} \quad \text{Equation 8}$$

$$\Delta Y = Y_{ground\ truth\ cloud} - Y_{UAS-based\ cloud} \quad \text{Equation 9}$$

$$\Delta Z = Z_{ground\ truth\ cloud} - Z_{UAS-based\ cloud} \quad \text{Equation 10}$$

$$\text{Absolute Distance} = \sqrt{(\Delta X)^2 + (\Delta Y)^2 + (\Delta Z)^2} \quad \text{Equation 11}$$

3.4.2. Density

Point cloud density can be defined as the number of 3D points present in a given area of the point cloud. It is crucial for a point cloud to be as dense as possible because dense point clouds are able to represent environments in a high level of detail. This is in contrast to sparse point clouds, which only represent the general shape of the environments (see Figure 24).

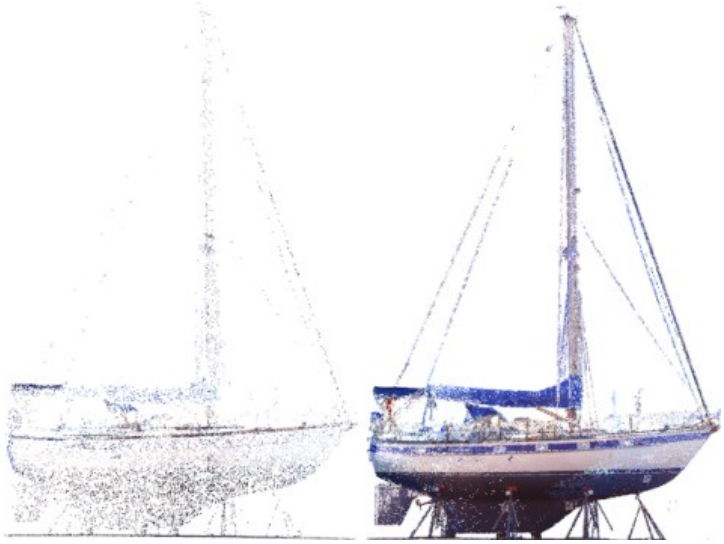

Figure 24: Sparse point cloud (left) vs. dense point cloud (right). (Autodesk, 2015)

Since laser scanners are able to generate dense point clouds, the laser-based point cloud can be used as the basis for evaluating the density of the UAS-based cloud. In doing so, ten $1m^2$ sections are randomly taken at several locations in the UAS-based cloud, and the number of points is computed. Similarly, identical sections are taken in the laser-based cloud, and the number of points is also computed. Thereafter, the results from each point cloud are compared to evaluate the density of the UAS-based point cloud when compared to the laser-based cloud.

3.4.3. Time and Cost

In the architecture, engineering, construction, and facility management (AEC/FM) industries, time and cost are crucial factors in deciding which tools or methods should be implemented and used. Therefore, a time- and cost-based comparison will be conducted to help professionals in the AEC/FM industry choose the modeling technique that best fits their needs. With respect to the time-based comparison, the time needed for creating the UAS-based and laser-based point clouds are recorded. This includes the time required for on-site data collection and the necessary time for processing the data in the office. In the cost-based comparison, the cost of generating the UAS-based and laser-based point clouds are computed and compared. This includes obtaining the cost of the equipment and software from official invoices and company websites. In addition to costs pertaining to the equipment and software, labor costs related to collecting and processing data for the point clouds can be estimated at 20$/hour.

CHAPTER 4: IMPLEMENTATION AND RESULTS

4.1. Implementation

In this chapter, the methodology outlined in chapter 3 will be applied to two case studies. Case study I is done on a close-loop segment of the 12th floor of Concordia University's Hall building (see Figure 25). Case study II is done on a close-loop segment of the 2nd floor of Concordia University's EV building (see Figure 26).

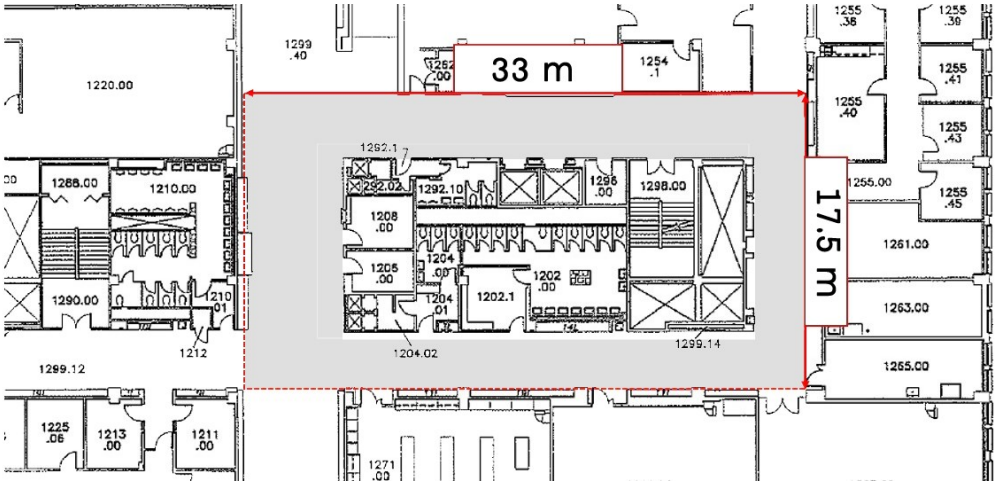

Figure 25: Hall building testing environment.

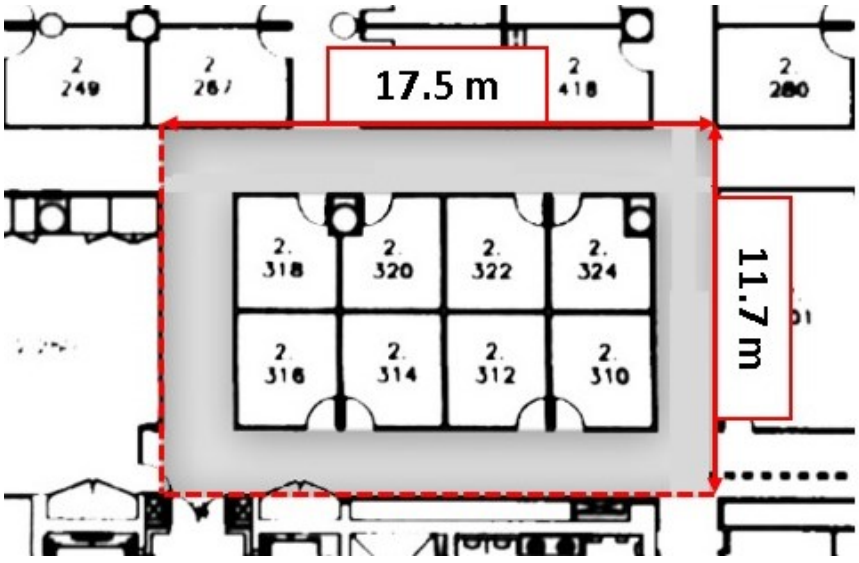

Figure 26: EV building testing environment.

Modeling surfaces with a low number of features can be a challenging task for the UAS-based modeling technique since it relies on the concepts of SfM for modeling. Therefore, to study the difference between modeling an environment with a low number of features and one with a high number of features these very different testing environments were selected. The Hall building testing environment contains several features on its wall sections. This is mainly because these wall sections are textured and contain several hangings and decorations on them (see Figure 27). On the other hand, the walls in the EV building testing environment are featureless since these walls are with one solid color and have a small number of decorations and hangings (see Figure 28).

Figure 27: Picture of the Hall building testing environment.

Figure 28: Picture of the EV building testing environment.

The following sections highlight the different equipment used in performing the case studies, followed by a detailed explanation of how the data was collected, processed, and compared. Finally, the results of each case study are presented at the end of this chapter as well.

4.1.1. Hardware

Equipment used for UAS-based modeling

To generate the UAS-based point cloud (for each case study), a DJI Phantom 3 Professional was used. The following sections highlight the technical specifications of the different components that make up this UAS. In addition, the rationale for choosing this particular UAS is discussed in this section as well.

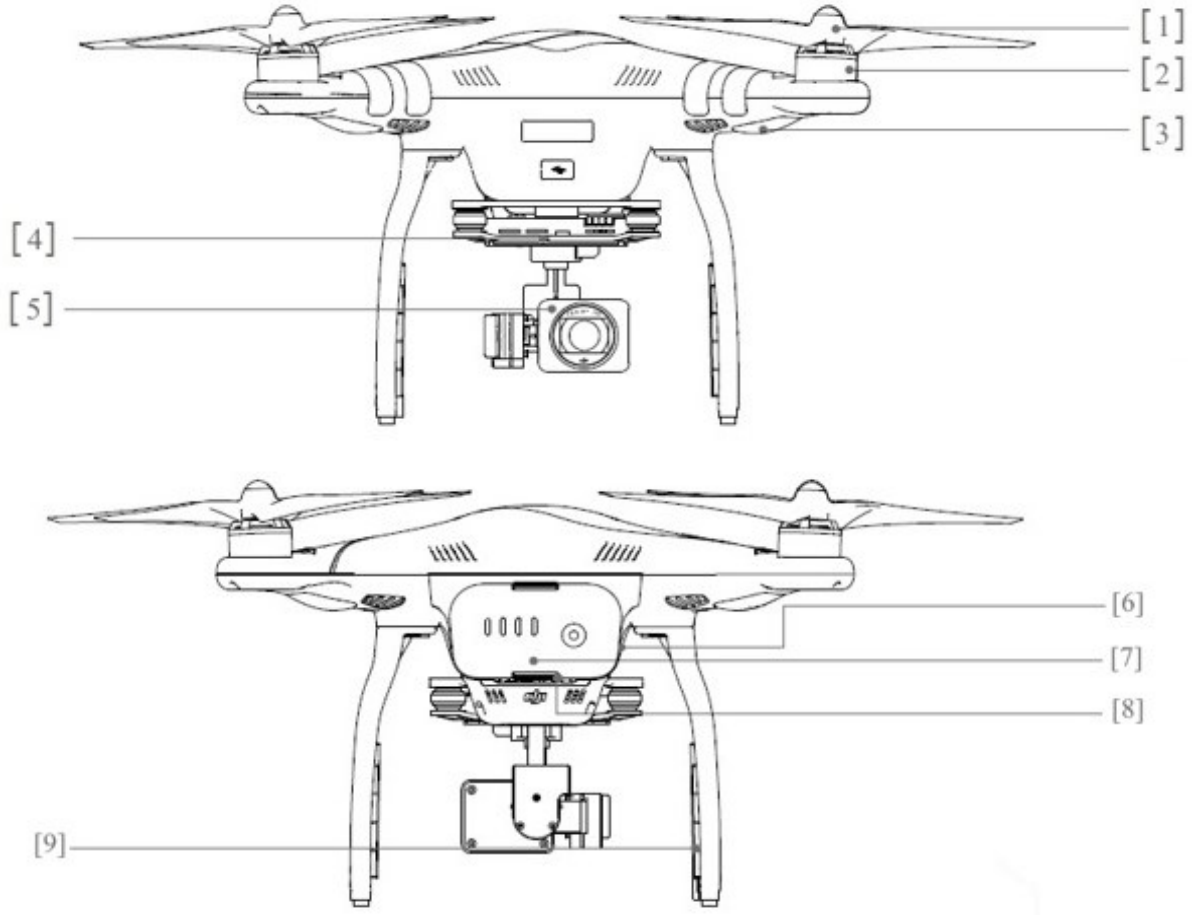

Figure 29: Components of the DJI Phantom 3 Professional. (DJI, 2015)

The DJI Phantom 3 Professional is made up of several components (see Figure 29). These components include:

[1][2] 4 different propellers and motors for flying. The propellers on the upper left corner and the lower right corner rotate clockwise while the other two propellers rotate anticlockwise.

[3] Two LED indicators, which are used to notify the user about the status of the aircraft (e.g. low battery).

[4] 3-axis gimbal, which connects the camera to the aircraft and is used to control the orientation of the camera.

[5] Sony EXMOR 12.4 Megapixel camera.

[6] SD card slot, which contains a 16 GB SD card that stores all the videos and images captured by the camera.

[7] 4480 mAh battery that provides up to 20 minutes of airtime.

[8] Indoor positioning sensors: one monocular camera and two ultrasonic sensors.

[9] Antennas for connecting the UAS to the ground control station.

Table 1: Technical specifications of the DJI Phantom 3 aircraft. (DJI, 2015)

Weight (Battery and Propellers included)	1280 g
Dimensions (including propeller guard)	612 x 612 mm
Max. Speed	16 m/s
Max. Altitude	6000 m
Max. Flight Time	23 m
Battery	4480 mAh – 15.2 V

The DJI phantom 3 Professional is equipped with a 12.4 Megapixel Sony camera (see Table 2 for technical specifications) which is used transmit a live video to the DJI GO smartphone application. Simultaneously, the camera can also be used to collect images or videos. The camera is mounted on the aircraft through a 3-axis gimbal (see Table 3 for technical specifications). The main function of the gimbal is to stabilize the camera during flight. It is also used to control the orientation of the camera.

Table 2: Technical specifications of the camera. (DJI, 2015)

Sensor	Sony EXMOR 1/2.3" Effective pixels: 12.4 M (total pixels: 12.76 M)
Lens	FOV 94° 20 mm (35 mm format equivalent) f/2.8, focus at ∞
ISO Range	100-3200 (video), 100-1600 (photo)
Shutter Speed	8s -1/8000s
Image Max Size	4000 x 3000

Table 3: Technical specifications of the gimbal. (DJI, 2015)

Controllable Range	Pitch -90° to +30°
Stabilization	3-axis (pitch, roll, yaw)

The DJI Phantom 3 is controlled by the ground control station (see Figure 30). The ground control station is made up of two parts: a remote controller (see Table 4 for technical specifications), and a smartphone connected to the remote controller. The remote controller is connected to the aircraft through a 2.4 GHz Wireless connection. The main function of the remote controller is to pilot the aircraft. It also has other functions such as a shutter button for collecting images, record button to collect videos, and dial for controlling the orientation of the camera. The remote controller is connected to a smartphone via a Micro USB port. The smartphone is used to run the DJI GO application (see Figure 31). This application offers several functions, including but not limited to:

1- Display a live video transmitted from the camera mounted on the aircraft.

2- Control the camera preferences (e.g., resolution, ISO, shutter speed)

3- Playback of all the images and videos captured by the camera.

4- Display the conditions of the aircraft (e.g., the status of the battery, the status of the connection between the aircraft and the remote controller)

Table 4: Technical specifications of the remote controller. (DJI, 2015)

Operating frequency	2.400 – 2.483 GHz
Max transmitting distance	2000 m (outdoor and unobstructed)
Battery	6000 mAh LiPo 2S
Smart Phone/Table connectivity	USB and Micro USB

Figure 30: The ground control station used in the case studies.

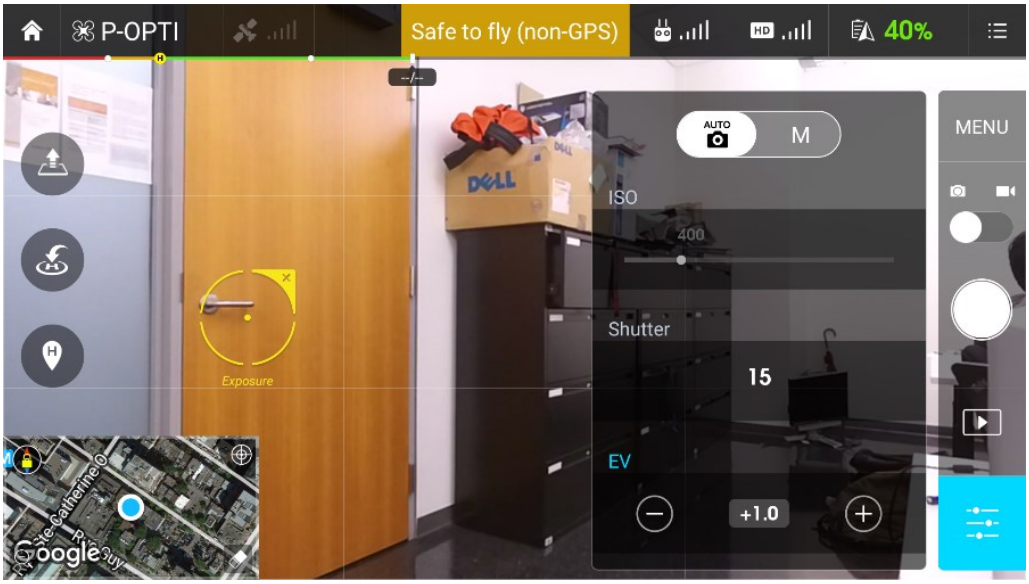

Figure 31: Screen capture of the DJI GO smartphone application.

Rationale for choosing the DJI Phanom 3

Nowadays, there are several types of UAS that are commercially available. In this research, the DJI Phantom 3 Professional was choose as the data collection tool for the generating the UAS-based point clouds. This choice was made for several reasons, including:

1) Suitable for indoor flight

Since both case studies are conducted indoors, the UAS must be suitable for indoor flight. There are certain features that make the DJI phantom 3 very suitable for flying indoors. First, it is small in size (612 x 612 mm), thus it can be easily maneuvered between narrow corridors and other obstructions that are always present in indoor environments. Second, it is fitted with protective propeller guards (see Figure 32) that can protect the propellers in the case of a collision. Finally, it includes several indoor positioning sensors (i.e., monocular camera and two ultrasonic sensors; see Figure 33) that help in positioning the aircraft during flight. This is typically done using a GPS. However, since this research only studies indoor environments, a GPS cannot be used. These indoor positioning sensors are also used to assist the pilot during take-off and landing.

Figure 32: The DJI Phantom 3 fitted with 4 propeller guards.

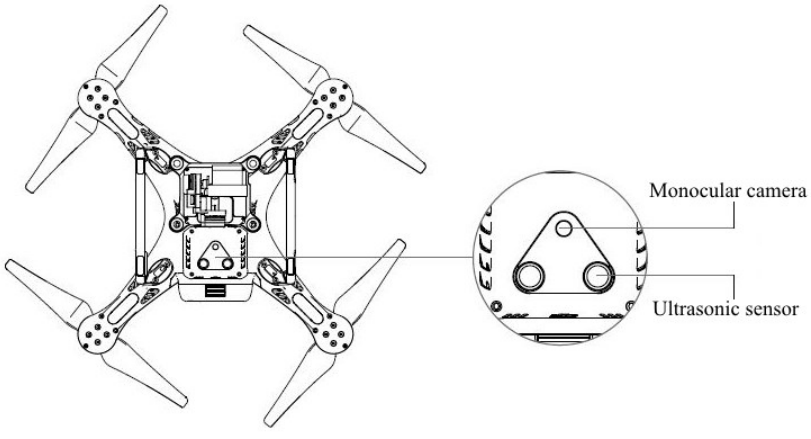

Figure 33: Indoor positioning sensors. (DJI, 2015)

2) Ability to collect images remotely

One of the main anticipated advantages of this research is the ability to model indoor environments remotely. Thus, is was vital to choose a UAS that can be piloted remotely. This is achievable with the DJI Phantom 3, as the camera can simultaneously collect images and transmit a live video to the ground control station (see Figure 34).

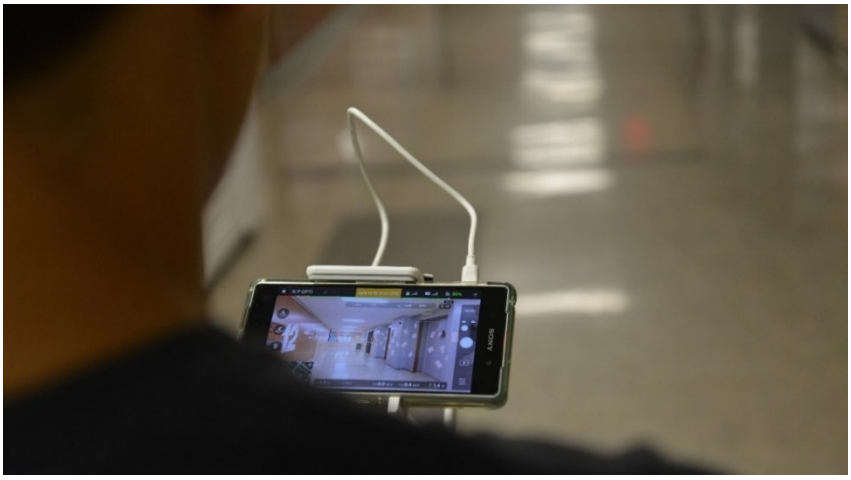

Figure 34: Piloting the DJI Phantom 3 remotely.

3) Image stabilization abilities

Image stabilization is vital for the success of the UAS-based modeling approach. This is mainly because blurry images can cause distortion in the point cloud. In the DJI Phantom 3, the camera is attached to the aircraft through a 3-axis gimbal, which stabilizes the camera from any movement on the Tait-Bryan angles (yaw, pitch, and roll). Additionally, the gimbal damps any vibration caused by the aircraft frame on the camera. This ensures that most images captured by the camera are stabilized (i.e., in focus).

4) High-resolution camera

The resolution of images directly affects the quality and density of the generated point cloud. As the number of pixels increases, the number of points matched and triangulated to create the point cloud increases. Thus, a high-resolution camera is needed to generate a dense point cloud. Moreover, a previous research study by Thoeni et al. (2014) suggests that in order for the SfM algorithm to give sufficient results a 9.5 Megapixel image sensor or higher must be used. The DJI

Phantom 3 is equipped with a Sony EXMOR 12.4 Megapixel image sensor, which should be enough to generate a dense point cloud.

Equipment used for laser-based modeling

To generate the laser-based point cloud (for each case study), a Faro Focus 3D X 130 laser scanner was used (see Figure 35; see Table 5 for technical specifications). This scanner was used to scan the testing environment from different positions to capture it completely. In addition, several reference targets were set out in the testing environment during the data collection in order to help in registering the scans from the different positions in a common coordinate system. These reference targets included spherical and checkerboard targets (see Figure 36).

Figure 35: Faro Focus 3D X 130. (Faro Technologies Inc., 2014)

Figure 36: Reference targets.

Table 5: Technical specifications of the Faro Focus 3D X 130. (Faro Technologies Inc., 2014)

Range (m)	0.6 - 130
Measurement speed (pts/sec)	122,000 - 976,000 [1]
Ranging error [2] (mm)	±2mm
Field of view (vertical/horizontal)	300° / 360°
Laser class	Laser class 1[3]
Data storage	SD, SDHC™, SDXC™
Scanner control	touchscreen display or WLAN with laptop/smartphone
Battery life	4.5 hours
Weight	5.2 kg
Size (mm)	240 x 200 x 100

[1] The measurement speed depends on the settings used.

[2] Ranging error is defined as a systematic measurement error at around 10m and 25m (Faro Technologies Inc., 2014).

[3] Laser class 1 is considered safe under all conditions of normal use (Faro Technologies Inc., 2014).

Equipment used for data processing and analysis

The machine used to process the information from the data collection stage and generate both the UAS- and laser-based point clouds was a Lenovo E440. This machine was also used in the comparison and evaluation stage, in which it was used to analyze and compare the UAS- and laser-based point clouds. Table 6 displays the technical specifications of the machine used in this research.

Table 6: Technical specifications of the Lenovo E440.

Processor	Intel Core i7 (4th Gen) 4702MQ @ 2.2 GHz
Memory (RAM)	12 GB DDR3
Storage	128 GB SATA III SSD
Graphics	NVIDIA® GeForce® GT740 M + 2GB VRAM
Operating system	Windows 7 Professional (64-bit)

4.1.2. Software

Software used for generating the UAS-based point clouds

The software used for generating the UAS-based point clouds was Autodesk ReCap 360 (see Figure 37; Autodesk ReCap 360, version 2.0). Recap 360 is an image processing software that uses the SfM algorithm to generate a point cloud from a collection of overlapping images. It is a cloud-based software, where it does all the image processing on the cloud computing technology. Moreover, it offers full automation of the SfM algorithm, from feature extraction to point cloud generation. However, some manual interference is sometimes required to improve the results and scale the model.

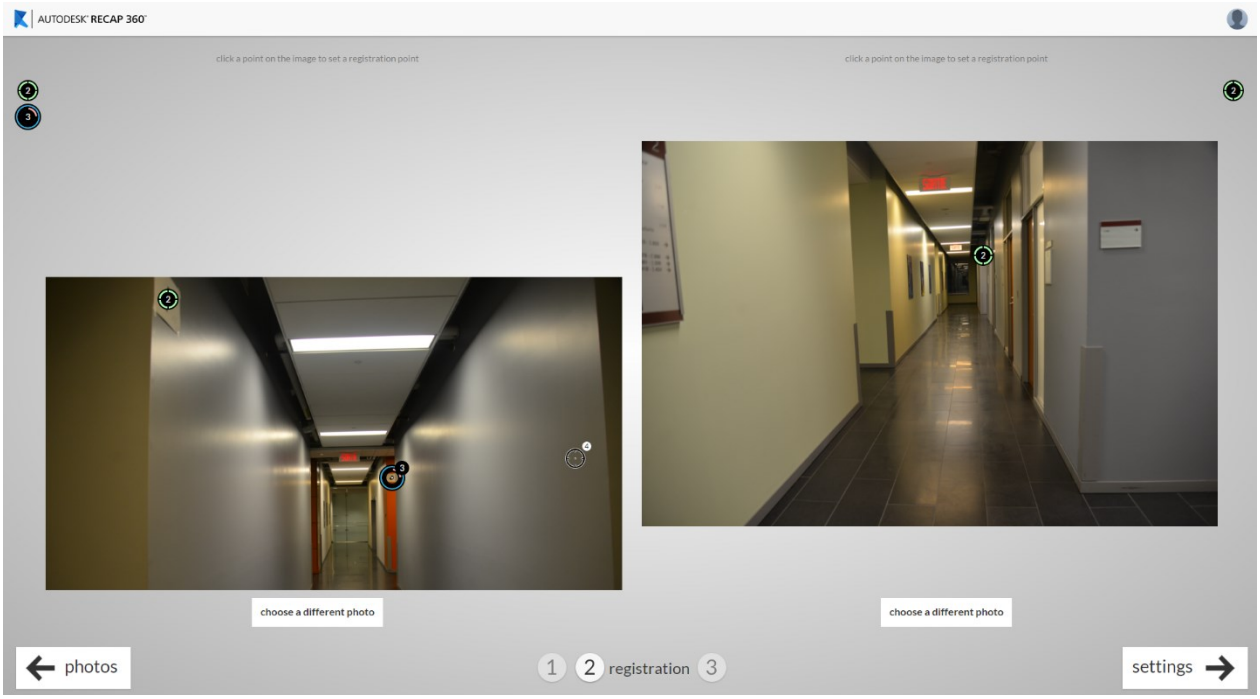

Figure 37: Point cloud generation using Autodesk Recap 360.

Software used for generating the laser-based point clouds

Laser scanning is always performed from several scanning positions to capture the environment completely. In order to create one comprehensive point cloud that includes all the scans from the different positions, the scans must be registered in a common coordinate system.

The software used for registration in this research work is Trimble RealWorks (see Figure 38; Trimble RealWorks, version 10.0.2.414), where it was used to identify and match the reference targets to register the scans together. Also, it was used to clean the final laser-based point clouds from any unnecessary points.

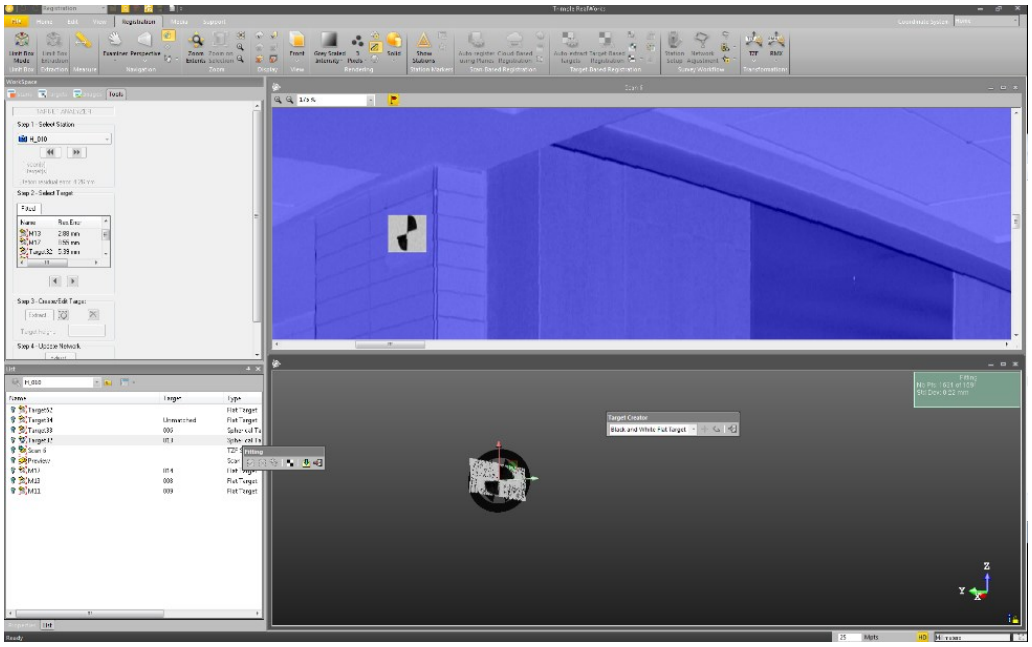

Figure 38: Registration using Trimble RealWorks.

Software used for deviation analysis

To measure the accuracy of the UAS-based point clouds, a deviation analysis was conducted. The open source software CloudCompare (CloudCompare, version 2.6.2) was utilized for this deviation analysis (see Figure 39). CloudCompare was also used for the density comparison. In which, it was used to segment the UAS- and laser-based point clouds into different 1 m^2 section and quantify the number of points for these sections.

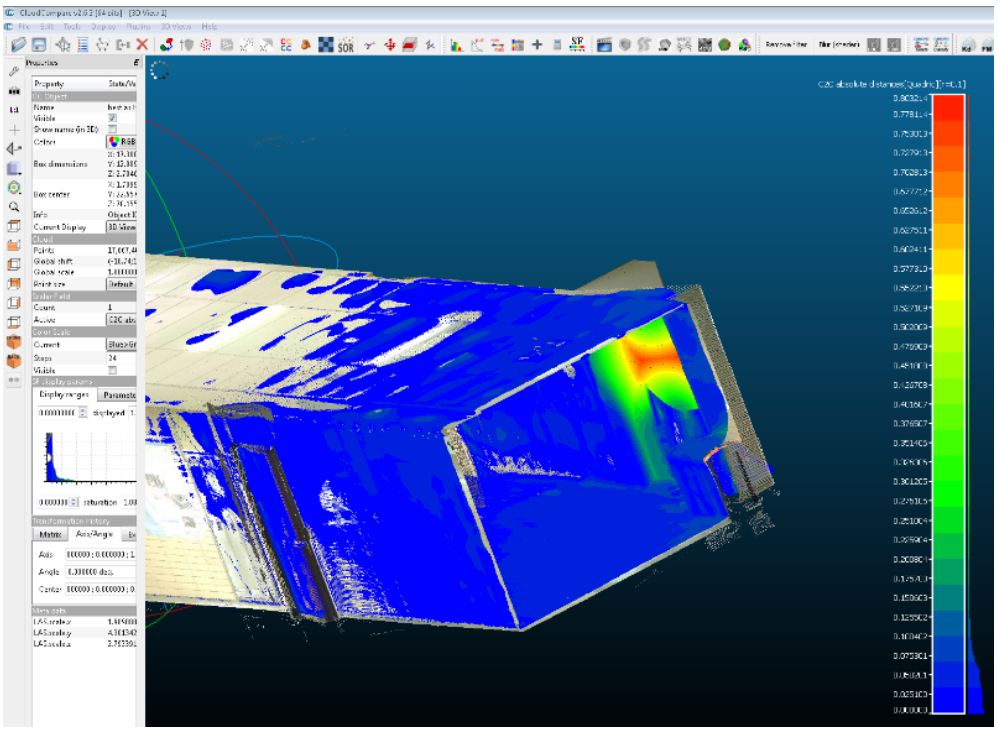

Figure 39: Deviation analysis using CloudCompare.

4.2. Case Study I – 12th Floor of Hall Building

4.2.1. Point Cloud Generation Using the UAS

Data Collection

In the data collection stage, the images required for generating a UAS-based point cloud of the Hall building testing environment were collected. The first step in doing this was to add visual markers to sections that were assumed to have a low number of features (e.g., stucco walls with one uniform color). This was done to artificially increase the number of features available and ensure adequate modeling of these sections. In total 50 visual markers were placed in the Hall building testing environment (see Figure 40).

After setting out the visual markers, a Sony Xperia Z2 smartphone was connected to the DJI remote controller and the DJI GO application was launched. Before takeoff, the image resolution was set to 4000x3000 pixels (maximum resolution). The maximum resolution was chosen to get the most pixels out of every image, which will increase the overall density of the generated point cloud. After that, the ground control station (i.e., the DJI remote controller

connected the Sony Xperia Z2 smartphone) was used pilot the UAS at a height of 1.5 approximately, which was enough to capture the vertical scene completely in each image. Also, it is worth noting that the camera lens was wide enough to capture the horizontal scene completely in each image. During the flight, the ground control station was used to pilot the UAS around the testing environment and collect overlapping images (see Figure 41). During image acquisition, an overlap of 80% or more was maintained between adjacent images (see Figure 42). On the corners of adjacent corridors, extra images were collected for two reasons. First, while collecting the images on the corners, the aircraft was in a turning motion which increased the possibility of obtaining blurry images. Therefore, extra images had to be taken to ensure having a sufficient number of overlapping images that were in-focus. Second, as the scene is completely changing from one corridor to the other, the features available in the scene are also changing. If there is not a sufficient number of features matched between the different corridors they will not stitch to each other. Thus, to guarantee that the corridors stitch to each other, extra overlapping images were taken at the corners between the corridors.

Figure 40: Visual markers added to the Hall building testing environment.

Figure 41: Pictures of the data collection for the Hall building UAS-based point cloud.

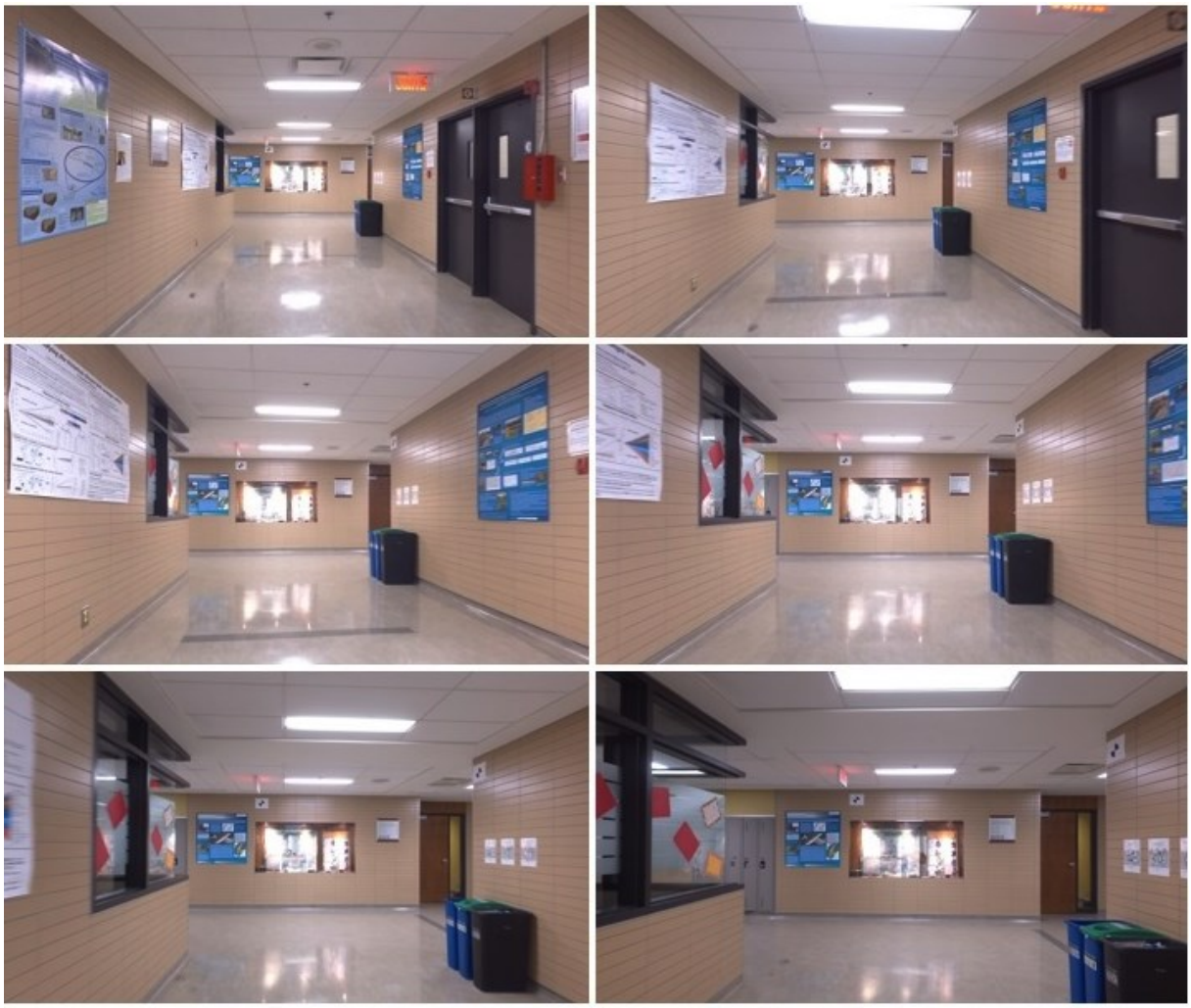

Figure 42: Sample of the overlapping images collected from the Hall building testing environment.

Table 7: Summary of the data collection for the Hall building UAS-based point cloud.

Number of visual markers placed	Number of images collected	Image resolution (pixels)	Focal length (mm)
50	272	4000x3000	8

Data processing

The first step after image acquisition was data filtration. In this stage, any irregularities in the set of images were removed. The irregularities mainly included blurry images and ones that contained moving objects (see Figure 43). After filtration, the number of images was reduced to 248 (see Table 8).

Table 8: Summary of the data filtration for the Hall building UAS-based point cloud.

Original No. of images	No. of images after filtration
272	248

Figure 43: Sample of the blurry images removed.

After filtration, the remaining images were uploaded to the software Autodesk ReCap 360 to generate the UAS-based point cloud (see Figure 44). Recap 360 automatically generated the point cloud by doing the following three processes: 1) identifying and matching of feature points across the images; 2) calculating approximate camera positions and orientations for each image taken (see Figure 45); 3) triangulating the 3D coordinates of each feature point identified from the camera positions and orientations to generate the point cloud. After generating the UAS-based point cloud, it was scaled by defining a well-known dimension that was measured on-site (see Figure 46). Figure 47 shows the final UAS-based point cloud of the Hall building testing environment.

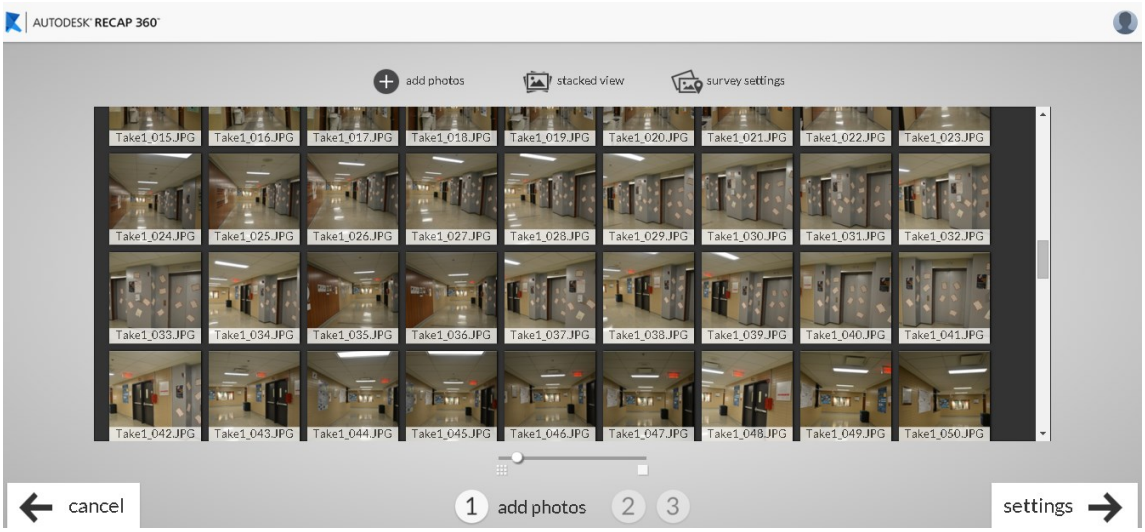

Figure 44: Uploading the images to Recap360.

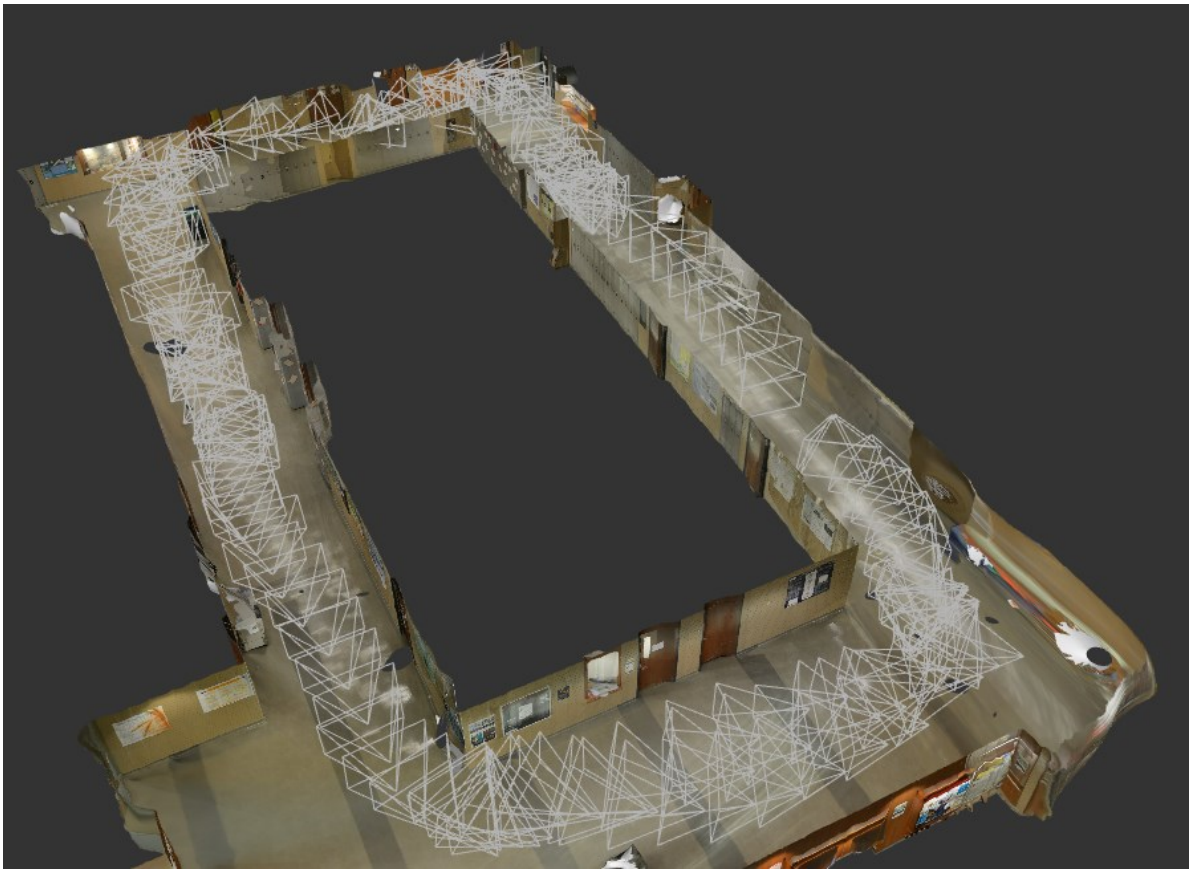

Figure 45: Camera positions and orientations in the Hall building UAS-based point cloud.

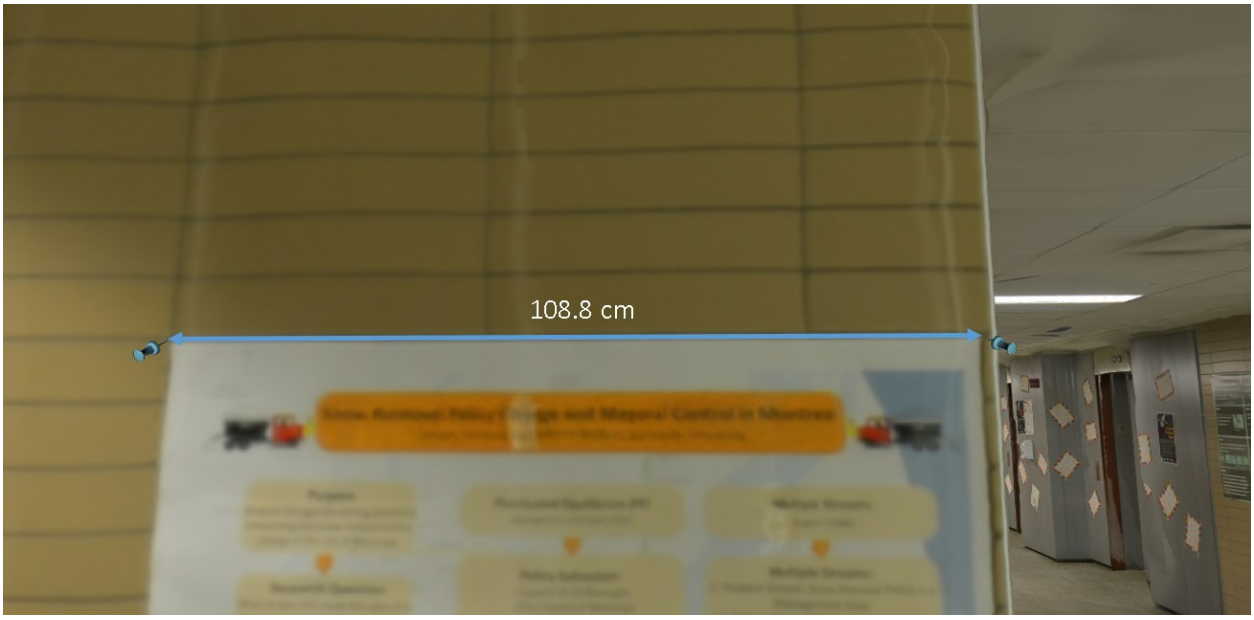

Figure 46: Scaling the UAS-based point cloud.

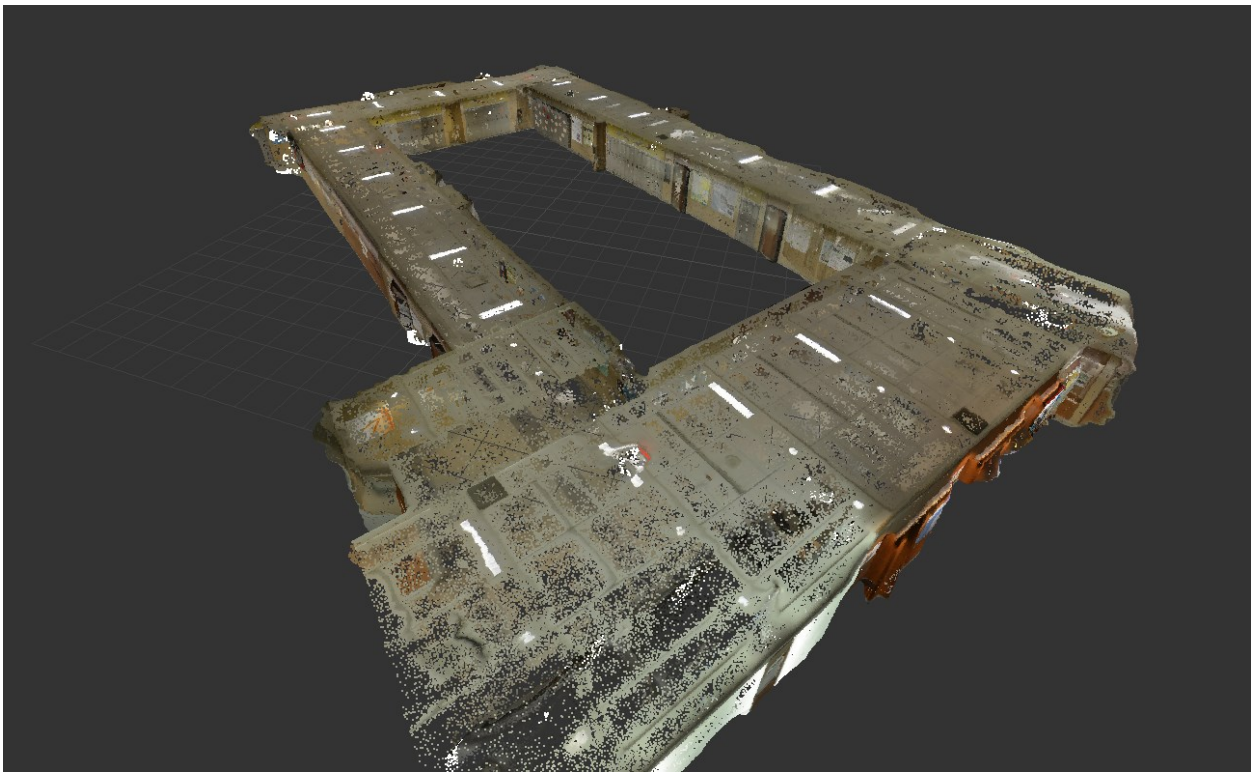

Figure 47: UAS-based point cloud of the Hall building testing environment.

4.2.2. Point Cloud Generation Using the Laser Scanner

Data collection

In the data collection stage, the Hall building testing environment was scanned from various locations using a Faro Focus3D X 130 laser scanner. The first step towards doing this was to place several spherical and checkerboard targets in different locations throughout the environment (see Figure 48). These reference targets are vital for the data processing stage as they will be used to register the scans from the different positions in a common coordinate system. In order to register two scans together, at least three reference targets must be seen from each scanning position. Thus, the location and orientation of each reference target were planned beforehand. Table 9 shows a summary of the reference targets placed in the Hall building testing environment

Table 9: Summary of the reference targets placed in the Hall building testing environment.

Number of spheres	Number of checkerboard targets
5	12

Figure 48: Sample of the reference targets placed the in Hall building testing environment.

After placing the reference targets, the Faro Focus3D X 130 laser scanner was securely screwed to a tripod and was placed in the first scanning position. A Lenovo E440 laptop was connected to the scanner via WLAN, to control it remotely (see Figure 49). Before starting the scan, the scanning parameters specific to the scan were selected (see Figure 50). Subsequently, the first scan was initiated, in which the laser scanner scanned the environment from the fist position,

and saved the resulting point cloud on the SD card. After the first scan was completed, the laser scanner and tripod were moved to the next scanning position for the next scan. This process was repeated until a sufficient number of scans was reached. The number and location of scans are dependent upon the range of the scanner, the complexity of the environment and the modeling requirements (i.e., what needs to appear in the point cloud). For case study I, 6 scans were sufficient to capture the Hall building testing environment completely (see Figure 51).

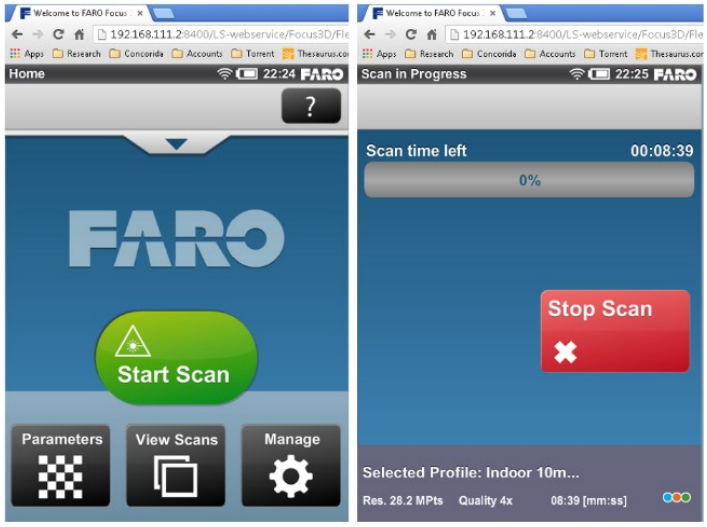

Figure 49: Interface used to control the laser scanner.

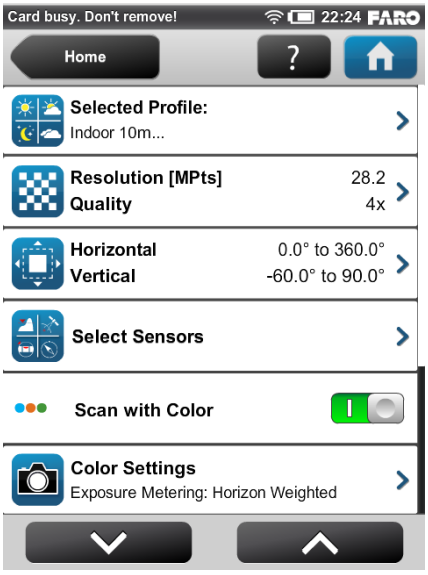

Figure 50: The scanning parameters used in both case studies.

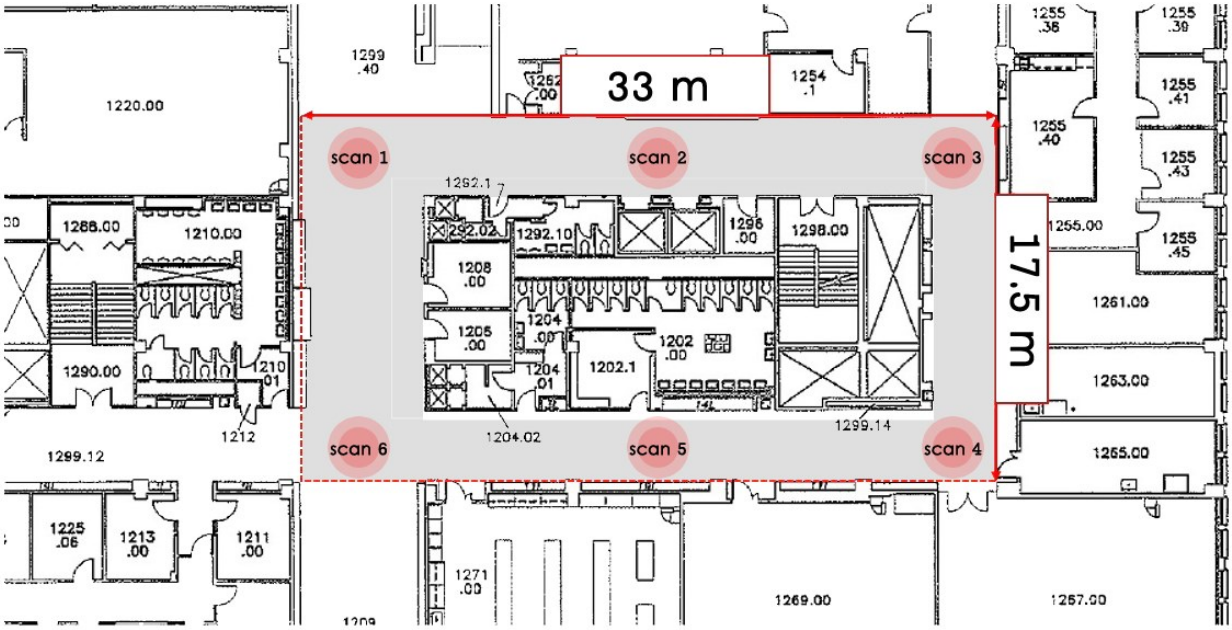

Figure 51: The scanning positions used in the Hall building testing environment.

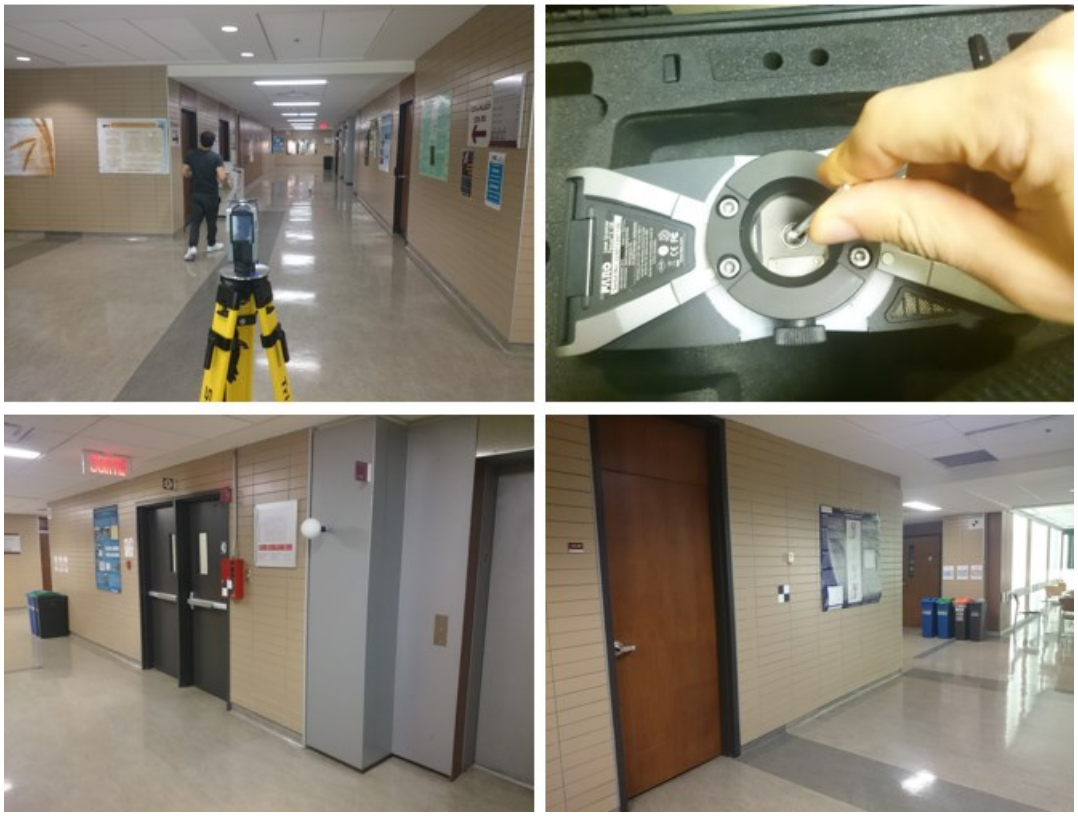

Figure 52: Pictures of the data collection for the Hall building laser-based point cloud.

Data processing

In data collection stage, the testing environment was scanned from different positions to create several point clouds. In the data processing stage, these point clouds will be registered in a common coordinate system to create one comprehensive point cloud of the environment. This process is commonly referred to as registration. In this case study, the Trimble RealWorks10 software was used for registration. The first step towards doing this was to load all the scans from the different scanning positions into the software. Next, the reference targets that were placed during data collection were identified in each scan (see Figure 53 and Figure 54). After all the available targets were identified, they were manually matched between the different scans. For example, in Figure 55 the target "Target1" from the scan "H_005" was manually matched with the targets "Target 6" and "Target 9" from the scans "H_006" and "H_007", respectively. After matching at least 3 targets between every two scans, the registration was analyzed, and the residual error was computed (see Figure 56). Finally, any unwanted points were removed from the registered point cloud to create the final laser-based point cloud of the Hall building (see Figure 57).

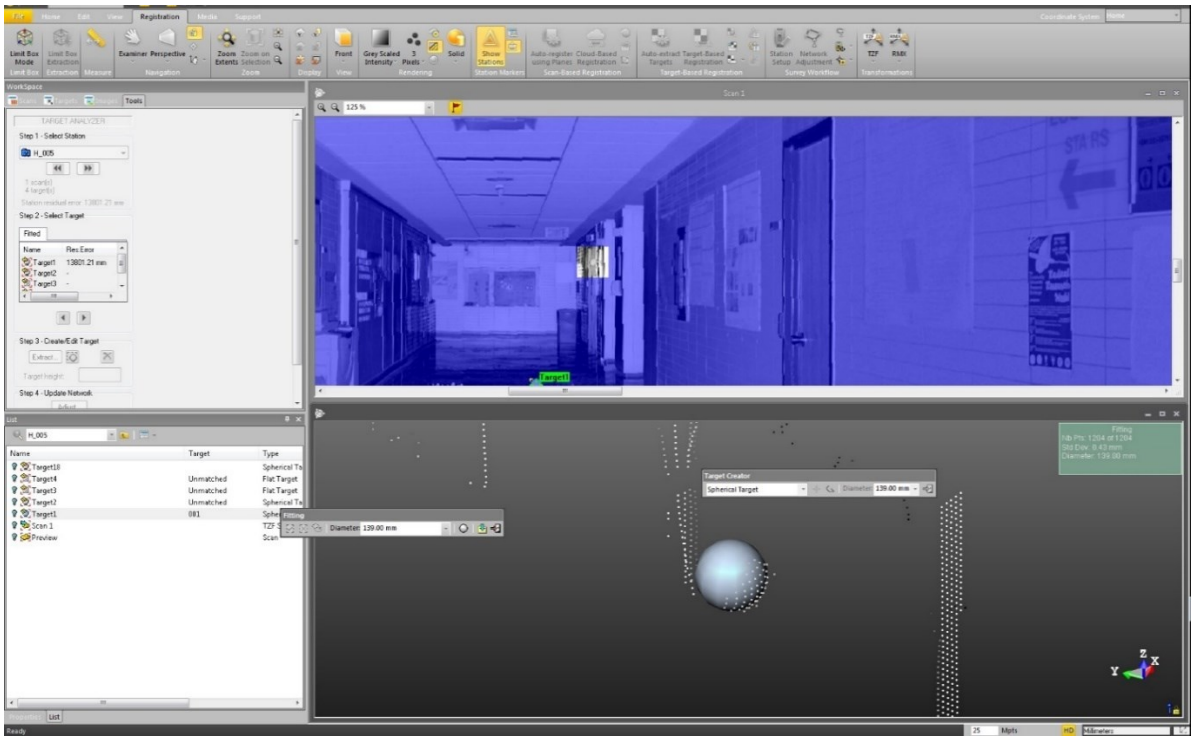

Figure 53: Identifying the spherical targets.

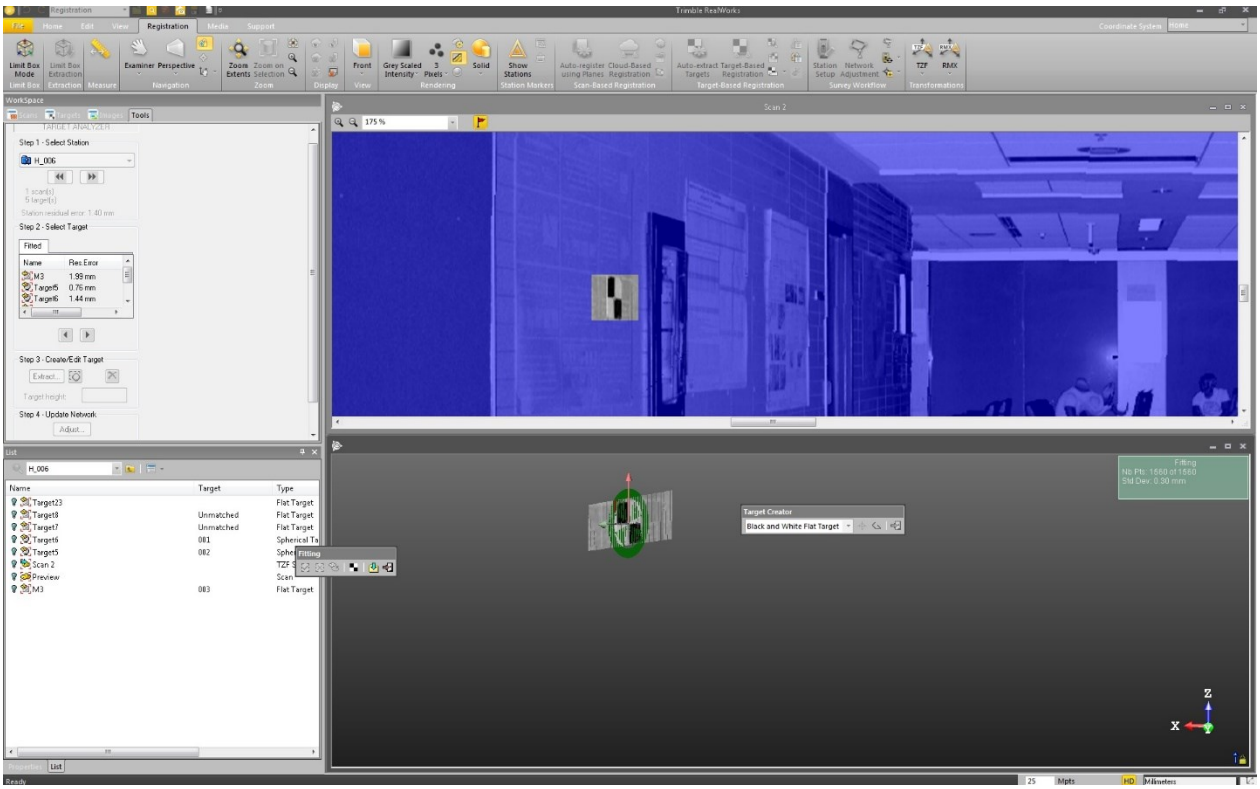

Figure 54: Identifying the checkerboard targets.

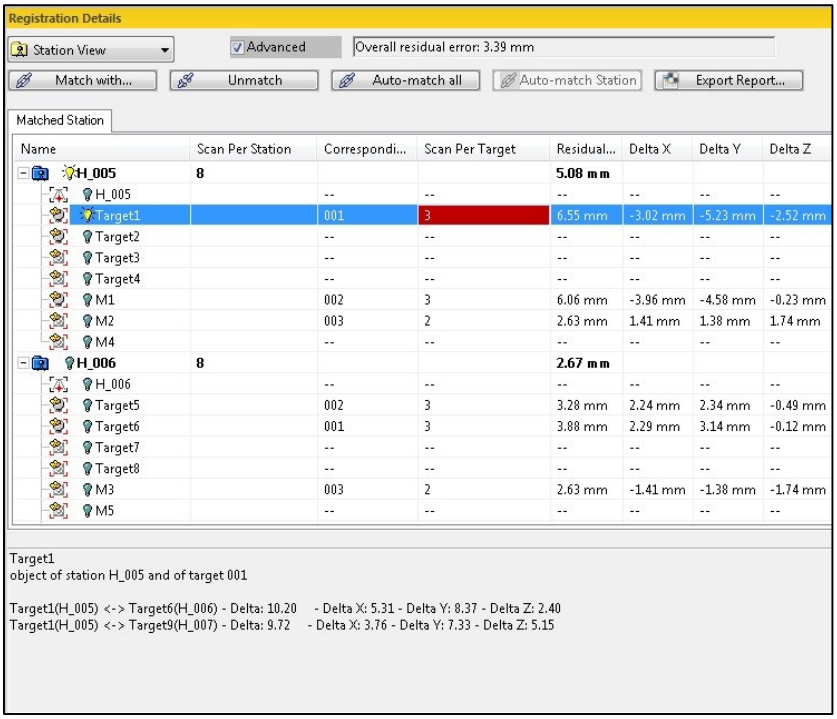

Figure 55: Matching the reference targets between the different scans.

Registration Details

Station View | Advanced | Overall residual error: 2.00 mm

Match with... | Unmatch | Auto-match all | Auto-match Station | Export Report...

Matched Station

Name	Scan Per Station	Correspondi...	Scan Per Target	Residual...	Delta X	Delta Y	Delta Z
H_005	**10**			**2.72 mm**			
H_005		--	--	--	--	--	--
M1		002	3	5.41 mm	-3.48 mm	-4.10 mm	0.64 mm
M2		--	--	--	--	--	--
M4		--	--	--	--	--	--
M18		014	2	3.89 mm	-2.19 mm	-2.44 mm	-2.09 mm
M19		015	2	0.98 mm	-0.89 mm	0.01 mm	0.43 mm
Target1		--	--	--	--	--	--
Target2		013	2	0.88 mm	-0.02 mm	0.62 mm	-0.62 mm
Target3		--	--	--	--	--	--
Target4		016	2	2.43 mm	1.15 mm	-0.43 mm	-2.10 mm
H_006	**8**			**2.17 mm**			
H_006		--	--	--	--	--	--
M3		--	--	--	--	--	--
M5		--	--	--	--	--	--
M6		005	2	1.45 mm	-0.23 mm	0.73 mm	1.23 mm
Target5		002	3	3.33 mm	2.37 mm	2.29 mm	-0.49 mm
Target6		001	2	1.73 mm	1.36 mm	0.50 mm	-0.94 mm
Target7		--	--	--	--	--	--
Target8		--	--	--	--	--	--
H_007	**9**			**1.66 mm**			
H_007		--	--	--	--	--	--
M15		--	--	--	--	--	--
M16		--	--	--	--	--	--
Target9		001	2	1.73 mm	-1.36 mm	-0.50 mm	0.94 mm
Target10		010	2	1.35 mm	0.64 mm	1.03 mm	-0.58 mm
Target11		002	3	2.13 mm	1.10 mm	1.81 mm	-0.15 mm
Target12		--	--	--	--	--	--
Target13		005	2	1.45 mm	0.23 mm	-0.73 mm	-1.23 mm
Target14		--	--	--	--	--	--
H_008	**8**			**1.78 mm**			
H_008		--	--	--	--	--	--
M8		007	2	2.51 mm	0.98 mm	2.27 mm	0.41 mm
M14		--	--	--	--	--	--
Target38		010	2	1.35 mm	-0.64 mm	-1.03 mm	0.58 mm
Target39		006	3	2.47 mm	-0.09 mm	0.19 mm	2.46 mm
Target40		008	3	0.79 mm	0.74 mm	-0.21 mm	0.18 mm
Target41		--	--	--	--	--	--
Target42		--	--	--	--	--	--
H_009	**7**			**1.69 mm**			
H_010	**9**			**1.98 mm**			

Figure 56: Residual error for the Hall building laser-based point cloud.

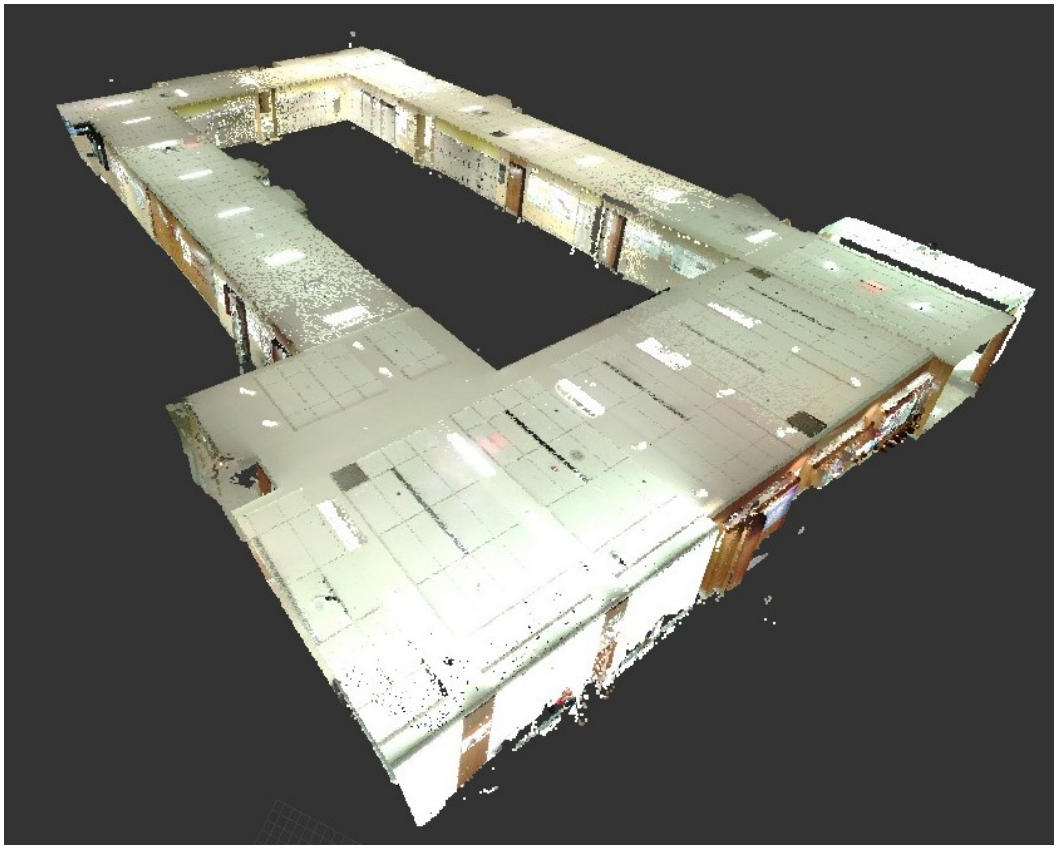

Figure 57: Laser-based point cloud of the Hall building testing environment.

4.2.3. Evaluation of Accuracy

In order to measure the accuracy of the UAS-based point cloud, a deviation analysis was conducted. To do this, a ground truth point cloud that accurately represents the spatial information of the testing environment was required. In this research, the laser-based point cloud from the laser scanner served as the ground truth point cloud. However, before the laser-based point cloud was declared the ground truth for this experiment its accuracy was checked.

Confirmation of the ground truth

Since the laser-based point cloud will serve as the ground truth in this study, its accuracy must be confirmed. To do this, a laser distance measurer was used to measure the actual dimensions of several location in the testing environment (see Figure 58). Later, the same locations were measured in the laser-based point cloud (see Figure 59) and compared with the actual dimensions in order to confirm that the laser-based point cloud can be used as the ground truth.

Figure 58: Measuring the actual dimensions of the Hall building testing environment.

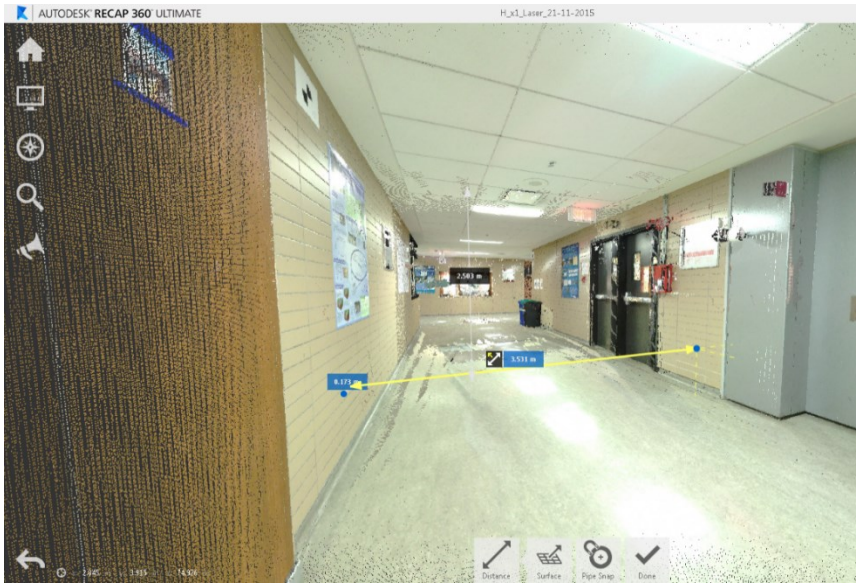

Figure 59: Measuring the dimensions of the Hall building laser-based point cloud.

Table 10: Validation of the ground truth (case study I).

Location #	Actual dimensions (m)	Measured dimensions from the laser-based point cloud (m)	Difference (mm)	Error%
1	1.088	1.089	-1.0	0.092%
2	3.535	3.533	2.0	0.057%
3	2.503	2.503	0.0	0.000%
4	3.531	3.531	0.0	0.000%
5	2.503	2.504	-1.0	0.040%
6	3.593	3.593	0.0	0.000%
7	3.971	3.970	1.0	0.025%
8	3.488	3.489	-1.0	0.029%

Location #	Actual dimensions (m)	Measured dimensions from the laser-based point cloud (m)	Difference (mm)	Error%
9	2.501	2.503	-2.0	0.080%
10	3.483	3.485	-2.0	0.057%
11	2.630	2.634	-4.0	0.152%
12	5.458	5.459	-1.0	0.018%
13	5.472	5.471	1.0	0.018%
Average=			**-0.6**	**0.044%**

Table 10 displays the actual and measured dimensions of 13 different locations in the Hall building. From this table, it can be noticed that the average difference between the actual and measured dimensions is 0.6 mm. Additionally, the average error was computed to be 0.044%. Therefore, the Hall building laser-based point cloud can be used as the ground truth.

Control points

The first step towards conducting the deviation analysis was to align the UAS-based point cloud with the ground truth point cloud (i.e., the laser-based point cloud) in a common coordinate system. To do this, 10 control points were placed in various locations throughout the Hall building testing environment before any data collection took place (see Figure 60). After generating both the UAS- and laser-based point clouds, 3 control points were matched between the different clouds to align them in a common coordinate system (see Figure 61). Furthermore, the remaining control points were compared between the UAS- and laser-based point clouds in a control point deviation analysis.

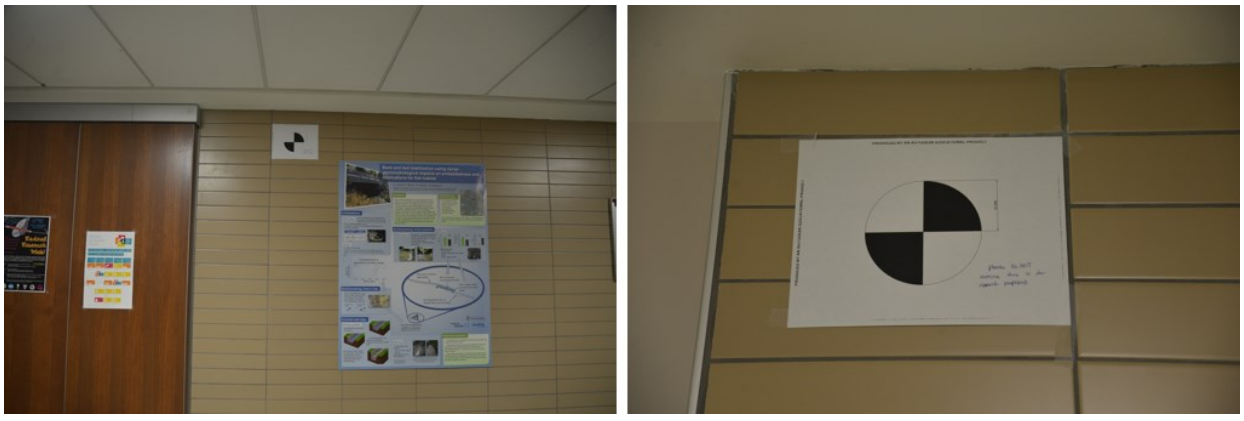

Figure 60: Control points placed in Hall building testing environment.

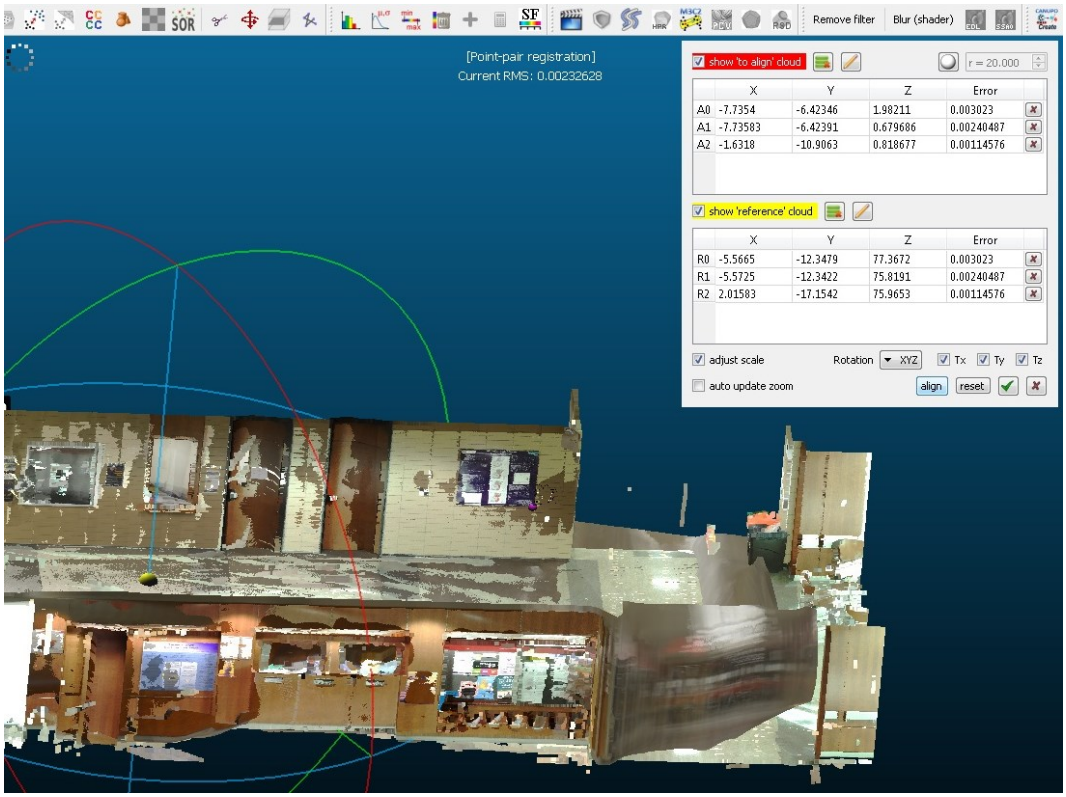

Figure 61: Aligning the UAS- and laser-based point clouds in common coordinate system

Point Cloud Deviation Analysis

In the point cloud deviation analysis the distance between each point in the UAS-based cloud and its hypothetical corresponding location in the ground truth point cloud is calculated. To do this, the UAS-based cloud was registered with the ground truth cloud in a common coordinate system. Then, the deviation of each point in the UAS-based point cloud was measured from their location in the ground truth point cloud using the open source software CloudCompare. The result was a scalar field that represents the deviation of each point in the UAS-based point cloud from the ground truth (see Figure 62). This scalar field consists of 100 deviation classes where each class represents a different range of deviation. For instance, points that fall under class 1 (7,334,122 points) deviate between 0 and 0.8 cm from the ground truth. Table 34 in appendix A shows the 100 deviation classes for the Hall building UAS-based point cloud. The results were then further analyzed to show the percentage of points that fall within each deviation class (see Figure 63). Additionally, Figure 64 shows the cumulative percentage of points per deviation class.

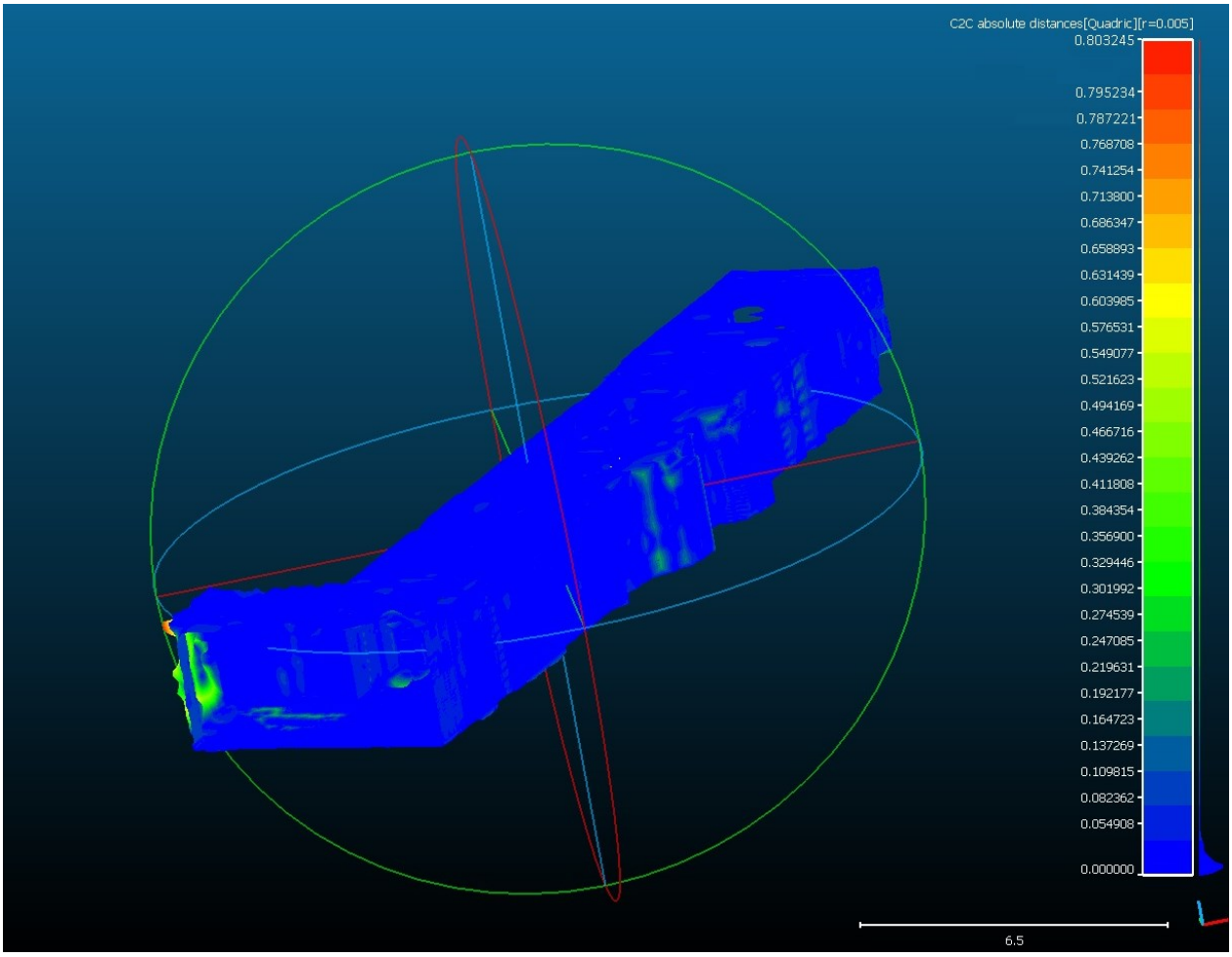

Figure 62: Deviation scalar field assigned to the Hall building UAS-based point cloud.

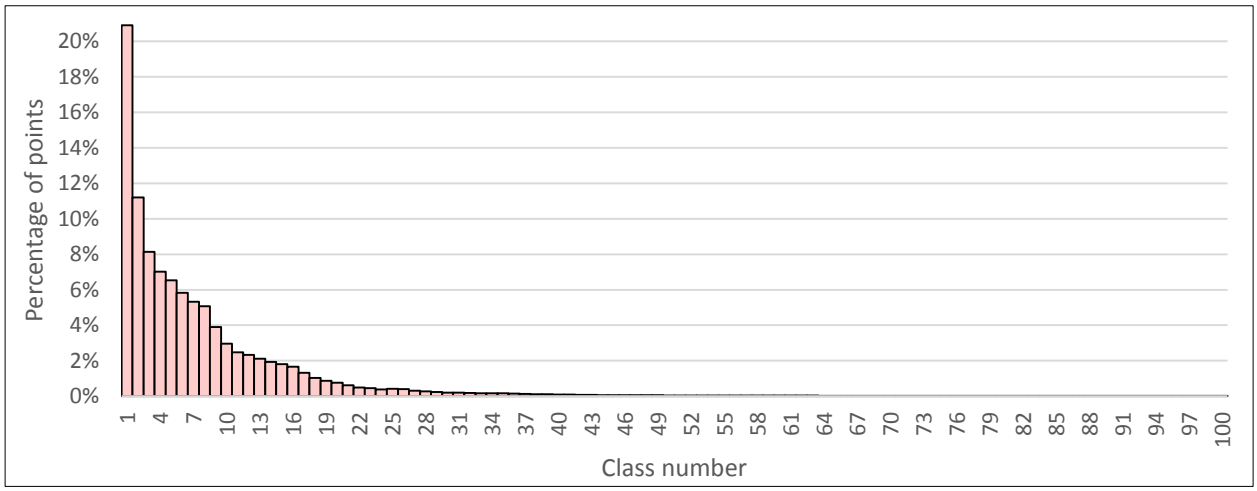

Figure 63: Percentage of points per deviation class –Hall building UAS-based point cloud.

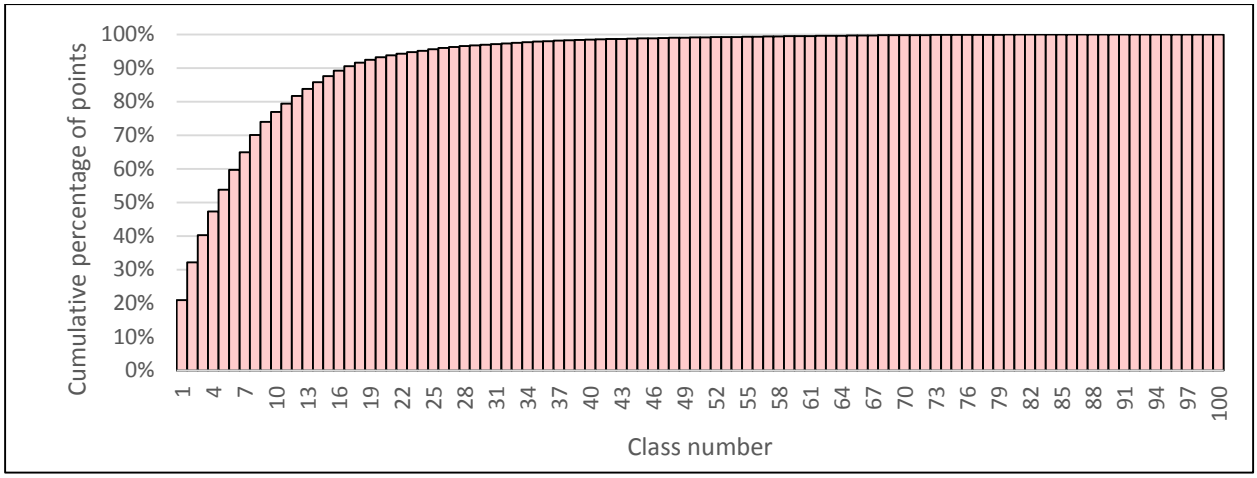

Figure 64: Cumulative percentage of points per deviation class – Hall building UAS-based point cloud.

Control Point Deviation Analysis

In the control point deviation analysis, the coordinates of each control point in the UAS-based point cloud and the ground truth point cloud were compared. This was done to find the deviation of each control point on the X, Y, and Z axis from the ground truth (see Figure 65). Additionally, the absolute distance between the location of the control points in the ground truth cloud and in their location in the UAS-based cloud was also computed. Table 11 shows the results of the control point deviation analysis.

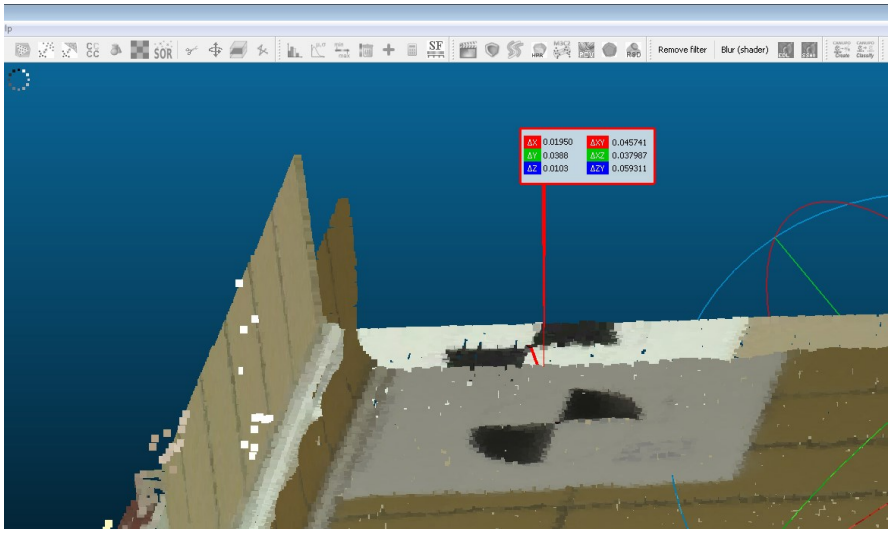

Figure 65: Control point deviation analysis for the Hall building UAS-based point cloud.

Table 11: Control point deviation analysis (case study I).

Control point #	ΔX (cm)	ΔY (cm)	ΔZ (cm)	Absolute distance (cm)
1	2.47	3.07	2.09	4.46
2	1.95	3.88	1.03	4.46
3 [a]	-	-	-	-
4	2.25	1.68	2.45	3.73
5	1.80	1.50	2.41	3.36
6 [a]	-	-	-	-
7	2.76	2.29	2.23	4.23
8 [a]	-	-	-	-
9	0.30	2.86	1.09	3.07
10	3.27	2.87	1.57	4.62
Maximum	**3.27**	**3.88**	**2.45**	**4.62**
Minimum	**0.30**	**1.50**	**1.03**	**3.07**
Average	**2.11**	**2.59**	**1.84**	**3.99**
Standard deviation	**0.94**	**0.83**	**0.61**	**0.61**

[a] The control points that were used for aligning the UAS-based point cloud with the ground truth point cloud.

4.2.4. Evaluation of Density

Another metric for measuring the effectiveness of UAS-based modeling is density. Therefore, the density of the Hall building UAS-based point cloud was compared to the density of the Hall building laser-based point cloud. In doing this, ten $1m^2$ sections were randomly taken at the UAS-based point cloud and the number of points was computed (see Figure 66). Next, identical sections were taken at the laser-based point cloud and the number of points was also computed (see Figure 67). Moreover, after noticing that the location of the section significantly affects the density of the laser-based point cloud, the sections were classified in accordance with their location, and distance from the laser scanner. The location classification represents where the section was taken: floor, wall, or ceiling. In the distance classification, the shortest distance between the 1 m^2 sections and the closest scanning position was used to assign the sections with one of the distance classes (see Table 12). Finally, Table 13 shows the number of points for each 1 m^2 section in the UAS- and laser-based point cloud.

Table 12: Distance classification.

Distance from the laser scanner (m)	Distance classes
0.1 - 0.5	v. close
0.5 - 1.0	close
1.0 - 2.0	far
2.0 - 4.0	v. far

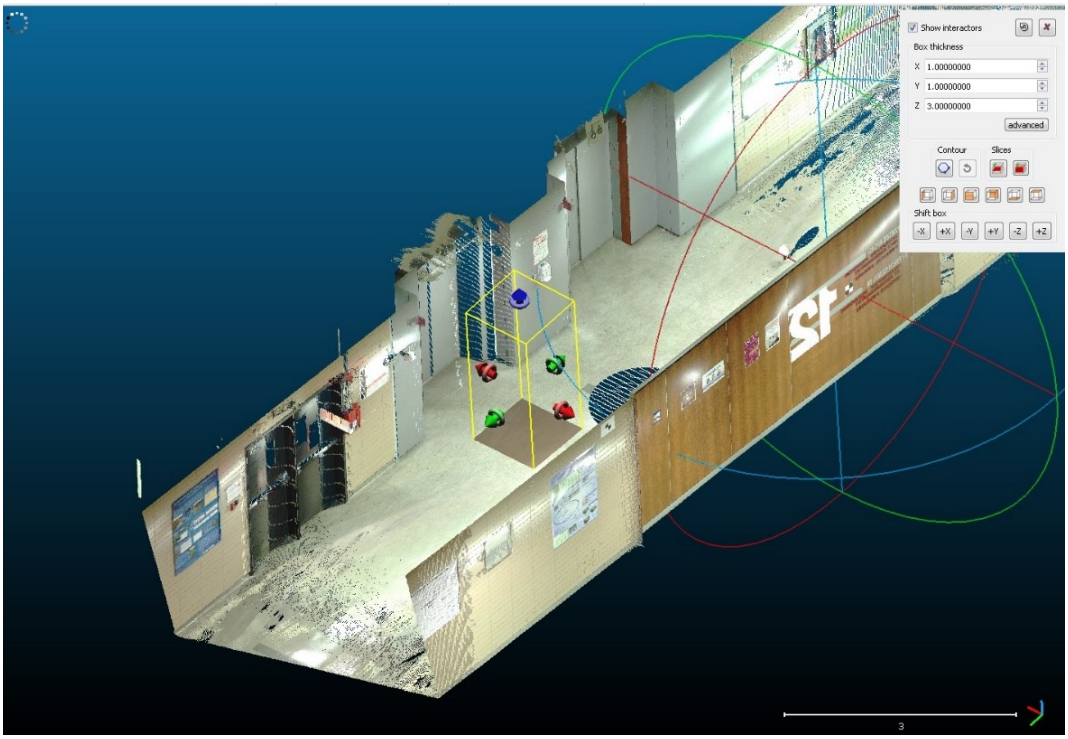

Figure 66: Sectioning the Hall building UAS-based point cloud.

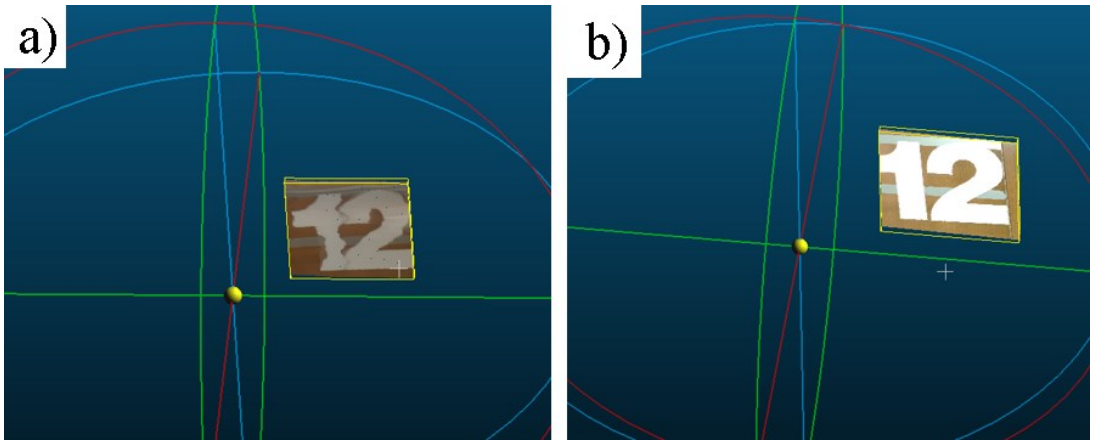

Figure 67: A sample of the 1 m^2 sections: a) at the UAS-based point cloud, b) at the laser-based point cloud.

Table 13: Number of points for each $1m^2$ section (case study I).

Section #	Number of points in the UAS-based point cloud	Number of points in the laser-based point cloud	Location class	Distance class
1	75,647	265,708	Floor	v. close
2	77,889	263,955	Wall	close
3	77,876	16,640	Floor	v. far
4	80,998	17,820	Wall	v. far
5	72,230	19,195	Wall	v. far
6	78,449	352,964	Floor	v. close
7	74,670	17,956	Wall	v. far
8	77,079	155,681	Floor	close
9	73,380	56,165	Wall	far
10	82,840	15,072	Floor	v. far
Average	**77,106**	**118,116**		
Standard deviation	**3,279**	**130,914**		

4.2.5. Time-based Comparison

To perform a time-based comparison, the time required for generating the UAS- and laser-based point clouds were documented while conducting the case study. Specifically, for the UAS-based technique, the time required for setting up the visual markers and collecting overlapping images was documented during the data collection stage. Additionally, the time required for processing the images and creating the UAS-based point cloud was also documented. This included the time needed for: 1) image filtration, in which blurry images were removed from the image set; 2) upload-to-software, in which the images were uploaded to the cloud-based software Autodesk Recap 360; 3) manual registration, in which the Recap 360 software was used to scale the point cloud and manually register images to improve the results; and 4) cloud processing, in which the Recap 360 software automatically generated the UAS-based point cloud on the cloud computing technology. Table 14 shows the time required for generating the Hall building UAS-based point cloud. Moreover, for the laser-based point cloud, the time required for setting up the reference targets, scanning the testing environment, and registering the scans to generate the laser-based point cloud were all recorded. Table 15 shows the time required for generating the Hall building laser-based point cloud.

Table 14: Time required for generating the Hall building UAS-based point cloud [a].

Setting up the visual markers (min)	Image acquisition (min)	Image filtration (min)	Upload-to-software [b] (min)	Manual registration (min)	Cloud processing (hr)	Total duration **excluding** cloud processing (hr)	Total duration **including** cloud processing (hr)
55.00	15.00	10.00	16.00	11.00	24.00	1.78	25.78

[a] The table is color-coded. Green belongs to the data collection stage, and yellow belongs to the data processing stage.

[b] Performed with a 19.86 Mbps internet upload speed (Ookla, 2015).

Table 15: Time required for generating the Hall building laser-based point cloud [a].

Setting up reference targets (min)	Scanning the testing environment (min)	Registration [b] (min)	Total duration (hr)
16	74	110	3.33

[a] The table is color-coded. Green belongs to the data collection stage, and yellow belongs to the data processing stage.

[b] Performed using a Lenovo E440. Technical specifications outlined in Table 6, page 56.

4.2.6. Cost-based Comparison

To perform a cost-based comparison, the cost of equipment and software used for constructing the Hall building UAS- and laser-based point clouds were recorded from official invoices and company websites. Additionally, the cost of labor needed for creating these point clouds was estimated as well. Table 16 shows the estimated cost of manpower, in which the time needed for data collection and processing were added up, and multiplied by the cost of labor per hour ($20/hour). Note that the cloud processing time was excluded from the calculation of labor costs, because it was done automatically on the cloud computing technology. Subsequently, the labor costs were added to the equipment and software costs to get the total cost of generating the Hall building UAS- and laser-based point clouds (see Table 17).

Table 16: Estimated cost of labor (case study I).

Technique	Duration of data collection (hr)	Duration of data processing **excluding** cloud processing (hr)	hourly labor rate ($/hr)[a]	Cost of manpower ($)
UAS-based	1.2	0.6	20.0	35.7
Laser-based	1.5	1.8	20.0	66.7

[a] Adopted from Dai et al. (2012)

Table 17: Cost-based comparison (case study I).

Technique	Equipment cost ($)	Software cost ($)	Cost of labor ($)	**Total**
UAS-based	2,637 [a]	2,500 [c]	36	**$ 5,173**
Laser-based	54,775 [b]	9,625 [d]	67	**$ 64,467**

[a] Acquired from an official invoice from Aircraft Modeler's Research Inc. (2015).

[b] Includes the cost of the Faro Focus 3D X130 laser scanner, a tripod, and the reference targets package (5 spheres and 24 checkerboard targets). Acquired from an official invoice from Cansel Survey Equipment Ltd. (2015).

[c] $500/year; projected for five years. Acquired from Autodesk (2015).

[d] Acquired from an invoice from Cansel Survey Equipment Ltd. (2015).

4.3. Case Study II – 2nd Floor of EV Building

4.3.1. Point Cloud Generation Using the UAS

Data Collection

In the data collection stage, the images required for generating a UAS-based point cloud of the EV building testing environment were collected. The first step towards doing this was adding visual markers to sections that were assumed to have a low number of features. In total 55 visual markers were placed in the EV building testing environment (see Figure 68).

Figure 68: Visual markers in the EV building testing environment.

After setting out the visual markers, the ground control station (i.e., the DJI remote controller connected to the Sony Xperia Z2 smartphone) was used to set the camera resolution to 4000x3000 pixels. Then, the ground control station was used to pilot the UAS around the testing environment and collect several overlapping images of it (see Figure 69). To ensure the proper matching of features, an overlap of 80% or more was maintained between adjacent images, as well as extra overlapping images were taken at the corners of adjacent corridors.

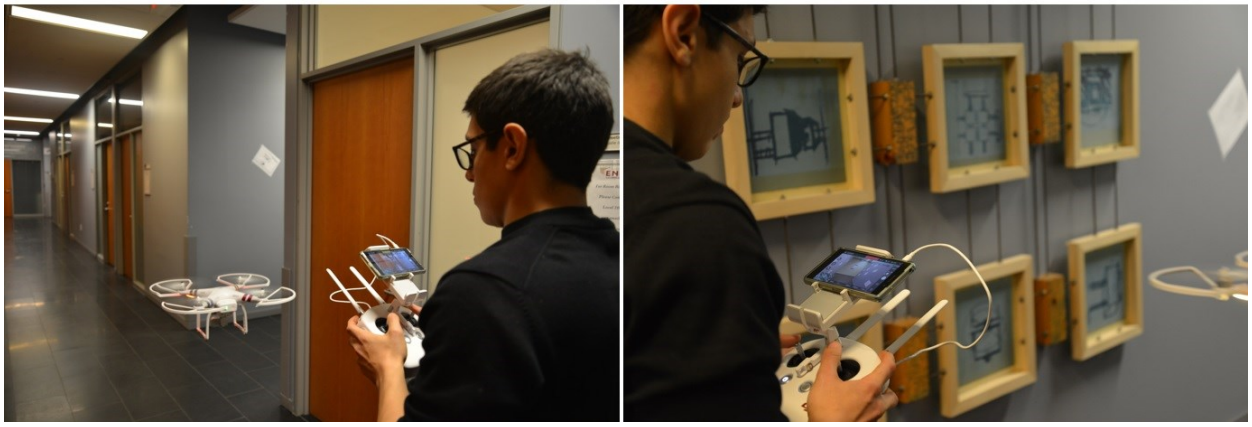

Figure 69: Pictures of the data collection for the EV building UAS-based point cloud.

Table 18: Summary of the data collection for the EV building UAS-based point cloud.

Number of visual markers placed	Number of images collected	Image resolution (pixels)	Focal length (mm)
55	220	4000x3000	8

Data processing

The first step after image acquisition was data filtration, in which irregularities such as moving objects (e.g., people passing) and blurry images were manually removed from the set of images (see Table 19). Afterward, the remaining images were uploaded to the cloud-based software Autodesk ReCap 360 to generate the UAS-based point cloud. Recap 360 automatically generated the EV building UAS-based 3D point cloud. However, it was manually scaled by defining a well-known dimension in the point cloud. Furthermore, it was noticed that some elements in the environment were appearing in an incorrect location in the point cloud. This was mainly caused by the presence of two visually similar corridors in the environment. This issue was solved by manually registering the images that suffered from this problem to images that appeared in their correct location (see Figure 70). Figure 71 shows the final UAS-based point cloud of the EV building testing environment.

Table 19: Summary of the data filtration for the EV building UAS-based point cloud.

Original No. of images	No. of images after filtration
220	203

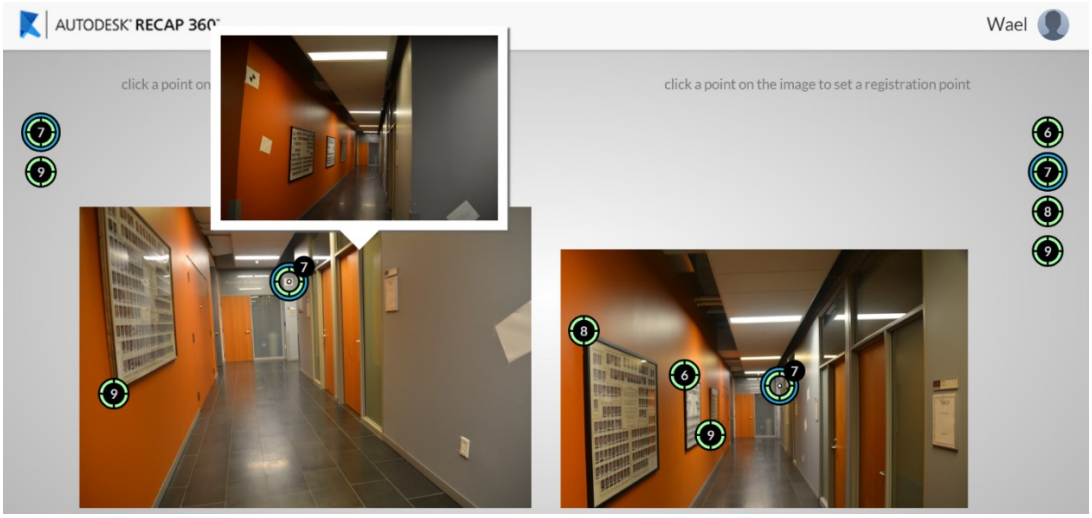

Figure 70: Manual registration.

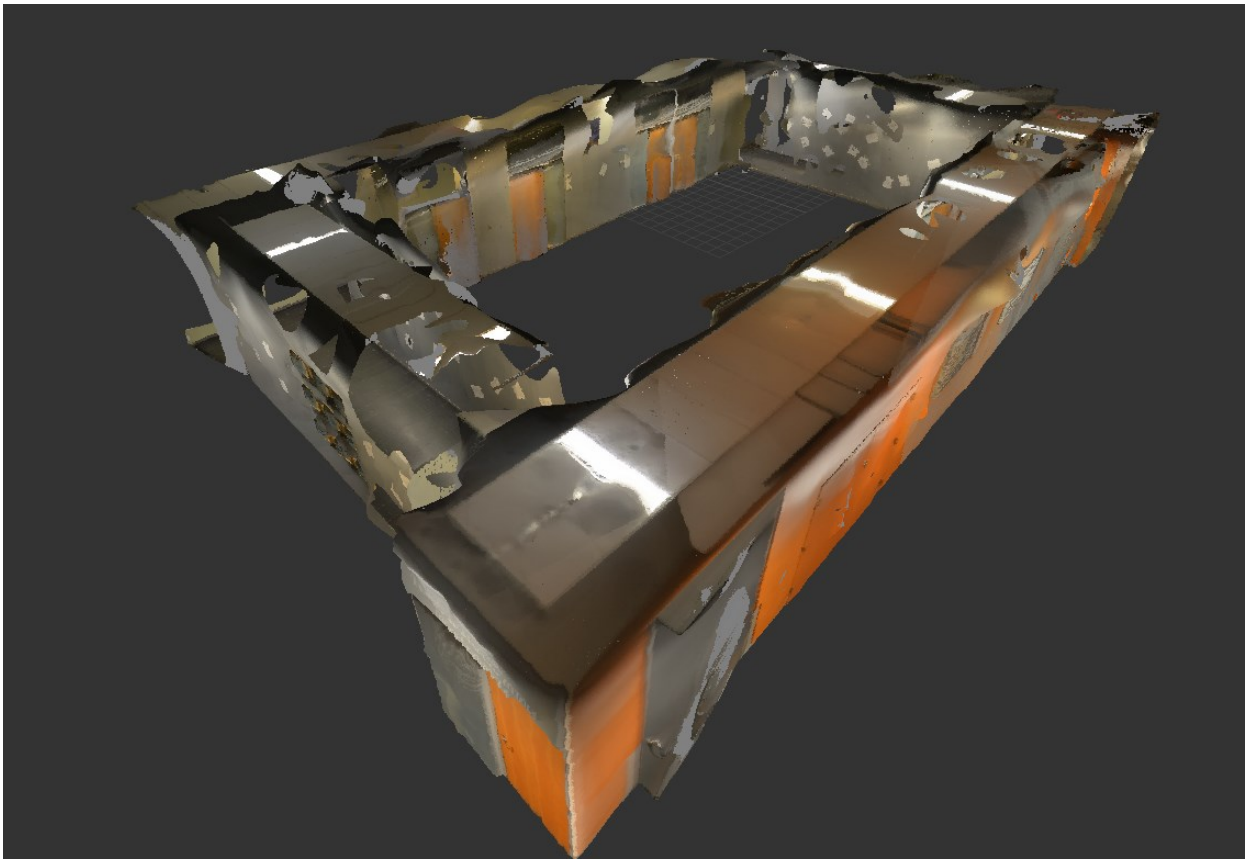

Figure 71: UAS-based point cloud of the EV building testing environment.

4.3.2. Point Cloud Generation Using the Laser Scanner

Data collection

In the data collection stage, the reference targets were first placed in various locations throughout the EV building testing environment (see Figure 72). Table 20 shows a summary of the reference targets placed in the EV building testing environment. After placing the reference targets, the Faro Focus3D X 130 laser scanner was placed in the first scanning position to scan it. The scanning parameters used for this case study were similar to ones used for case study I (see Figure 50). After the scanning parameters were set, the laser scanner was used to scan the testing environment from the first position. After the first scan was completed, the scanner and tripod were moved to the next scanning position for the next scan. This process was repeated until a sufficient number of scans was reached. For the EV building testing environment, 4 scans were sufficient to capture the environment completely (see Figure 73).

Figure 72: Sample of the reference targets placed the in EV building testing environment.

Table 20: Summary of the reference targets placed in the EV building testing environment.

Number of spheres	Number of checkerboard targets
5	7

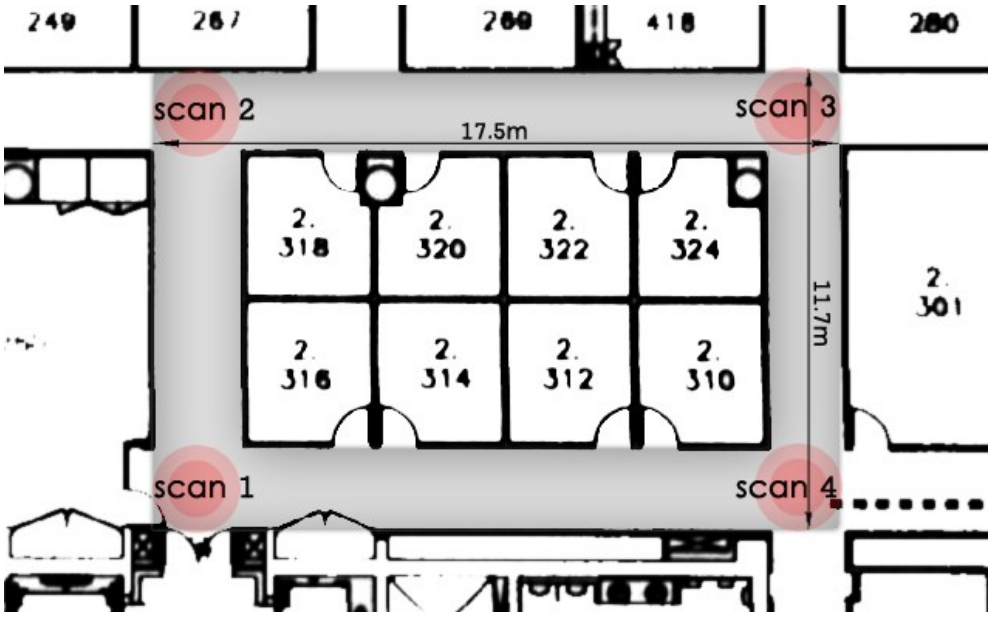

Figure 73: The scanning positions used in the EV building testing environment.

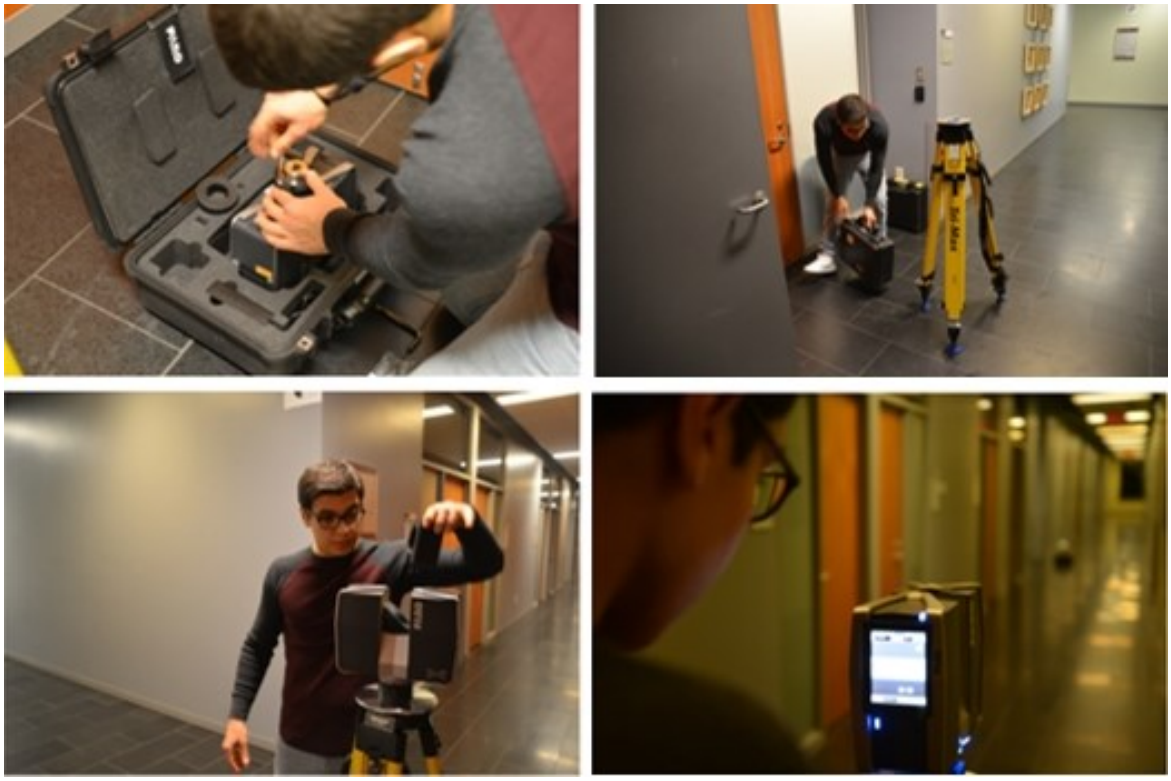

Figure 74: Pictures of the data collection for the EV building laser-based point cloud.

Data Processing

In the data processing stage, the Trimble RealWorks10 software was used to register the point clouds from the different scanning positions in a common coordinate system. This was done by matching the reference targets between the point clouds from the different scanning positions (see Figure 75). After matching at least 3 targets between every two scans, the registration was analyzed, and the residual error was computed. Figure 78 shows the final residual error computed for the EV building laser-based point cloud. Finally, the registered point cloud was removed from any unwanted points (Figure 76), to create the final EV building laser-based point cloud (see Figure 77).

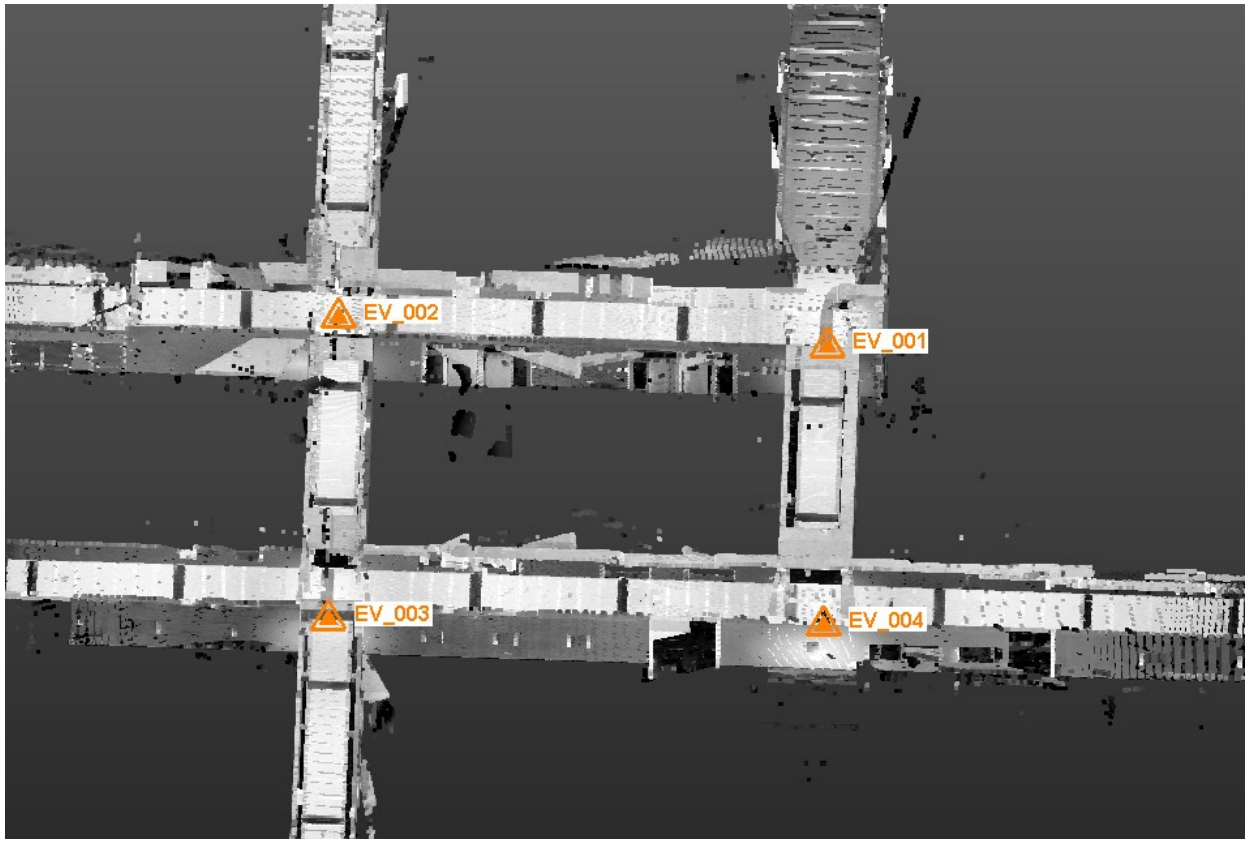

Figure 75: Registering the point clouds from the different scanning positions.

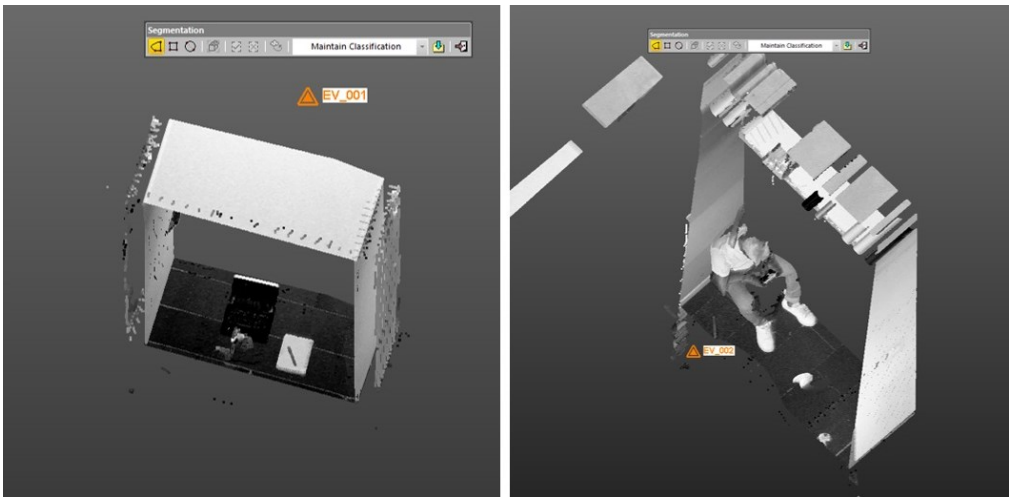

Figure 76: Sample of the unwanted points.

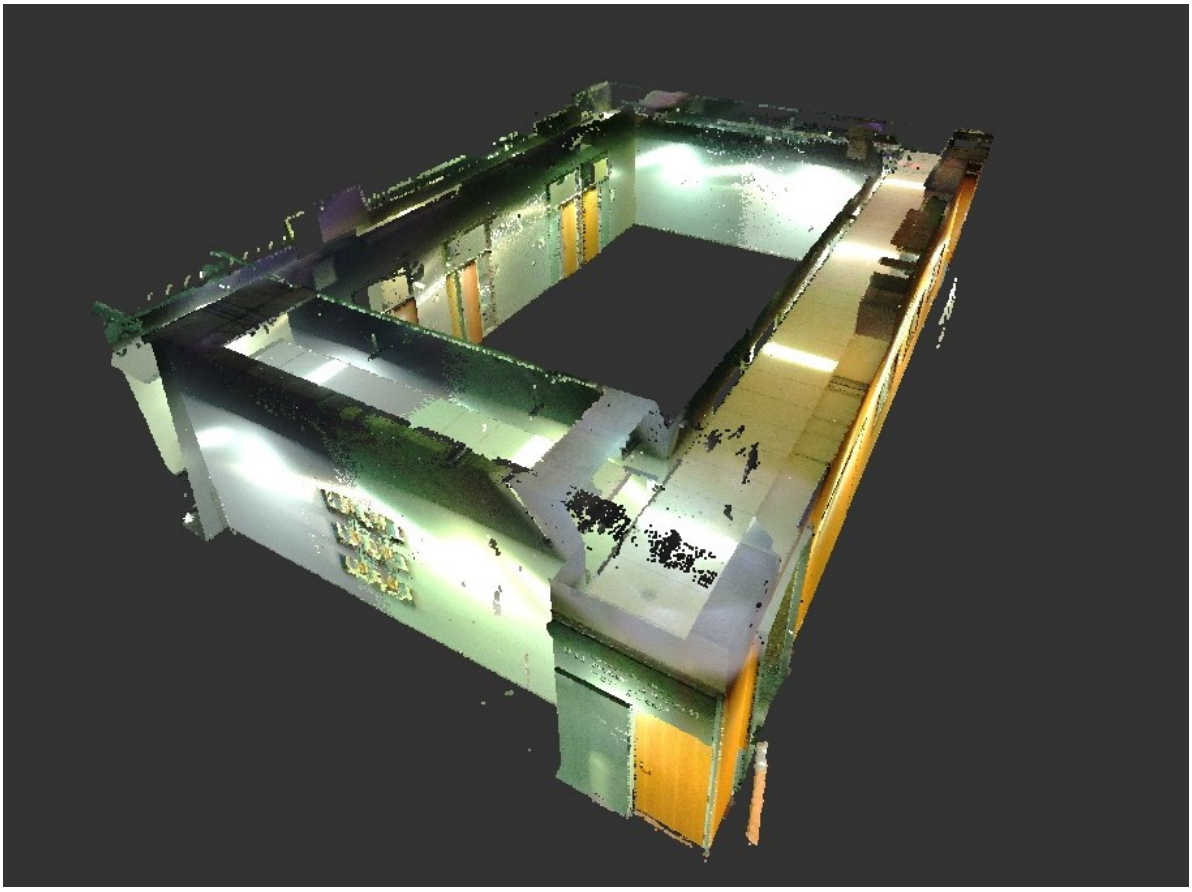

Figure 77: Laser-based point cloud of the EV building testing environment.

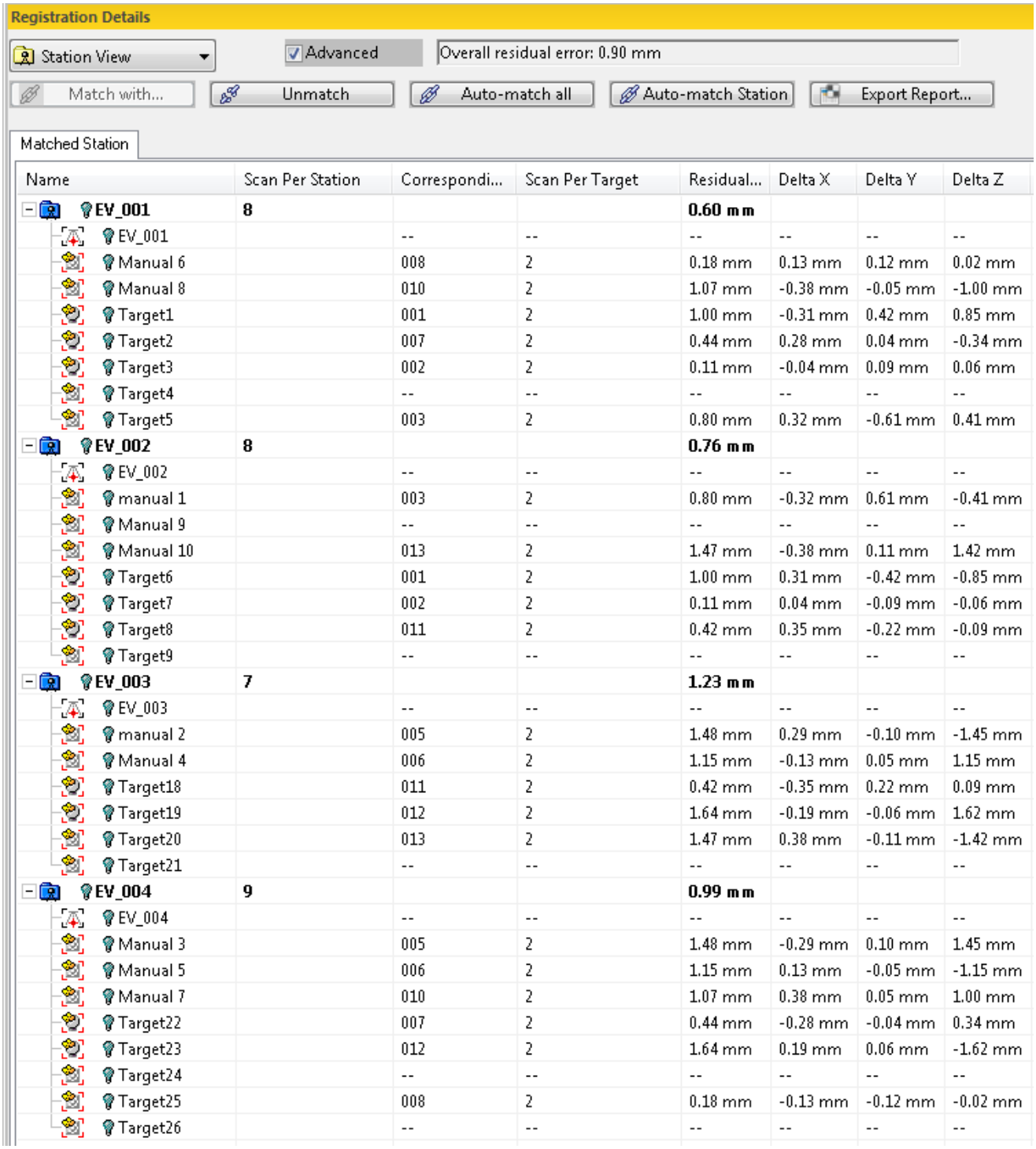

Name	Scan Per Station	Correspondi...	Scan Per Target	Residual...	Delta X	Delta Y	Delta Z
EV_001	**8**			**0.60 mm**			
EV_001		--	--	--	--	--	--
Manual 6		008	2	0.18 mm	0.13 mm	0.12 mm	0.02 mm
Manual 8		010	2	1.07 mm	-0.38 mm	-0.05 mm	-1.00 mm
Target1		001	2	1.00 mm	-0.31 mm	0.42 mm	0.85 mm
Target2		007	2	0.44 mm	0.28 mm	0.04 mm	-0.34 mm
Target3		002	2	0.11 mm	-0.04 mm	0.09 mm	0.06 mm
Target4		--	--	--	--	--	--
Target5		003	2	0.80 mm	0.32 mm	-0.61 mm	0.41 mm
EV_002	**8**			**0.76 mm**			
EV_002		--	--	--	--	--	--
manual 1		003	2	0.80 mm	-0.32 mm	0.61 mm	-0.41 mm
Manual 9		--	--	--	--	--	--
Manual 10		013	2	1.47 mm	-0.38 mm	0.11 mm	1.42 mm
Target6		001	2	1.00 mm	0.31 mm	-0.42 mm	-0.85 mm
Target7		002	2	0.11 mm	0.04 mm	-0.09 mm	-0.06 mm
Target8		011	2	0.42 mm	0.35 mm	-0.22 mm	-0.09 mm
Target9		--	--	--	--	--	--
EV_003	**7**			**1.23 mm**			
EV_003		--	--	--	--	--	--
manual 2		005	2	1.48 mm	0.29 mm	-0.10 mm	-1.45 mm
Manual 4		006	2	1.15 mm	-0.13 mm	0.05 mm	1.15 mm
Target18		011	2	0.42 mm	-0.35 mm	0.22 mm	0.09 mm
Target19		012	2	1.64 mm	-0.19 mm	-0.06 mm	1.62 mm
Target20		013	2	1.47 mm	0.38 mm	-0.11 mm	-1.42 mm
Target21		--	--	--	--	--	--
EV_004	**9**			**0.99 mm**			
EV_004		--	--	--	--	--	--
Manual 3		005	2	1.48 mm	-0.29 mm	0.10 mm	1.45 mm
Manual 5		006	2	1.15 mm	0.13 mm	-0.05 mm	-1.15 mm
Manual 7		010	2	1.07 mm	0.38 mm	0.05 mm	1.00 mm
Target22		007	2	0.44 mm	-0.28 mm	-0.04 mm	0.34 mm
Target23		012	2	1.64 mm	0.19 mm	0.06 mm	-1.62 mm
Target24		--	--	--	--	--	--
Target25		008	2	0.18 mm	-0.13 mm	-0.12 mm	-0.02 mm
Target26		--	--	--	--	--	--

Figure 78: Residual error for the EV building laser-based point cloud.

4.3.3. Evaluation of Accuracy

Similarly to case study I, to measure the accuracy of the EV building UAS-based point cloud in case study II, a deviation analysis was conducted. The EV building laser-based point cloud will serve as the ground truth for this deviation analysis. The following sections show how the deviation analysis was conducted for case study II.

Confirmation of the ground truth

Since the EV building laser-based point cloud will serve as the ground truth in this study, its accuracy must be validated. To do this, a laser distance measurer was used to measure the actual dimensions of 8 locations in the EV building testing environment (see Figure 79). Later, the same locations were measured in the EV building laser-based point cloud (see Figure 80), which were then compared with the actual dimensions to confirm that it can be used as the ground truth.

Figure 79: Measuring the actual dimensions of the EV building testing environment.

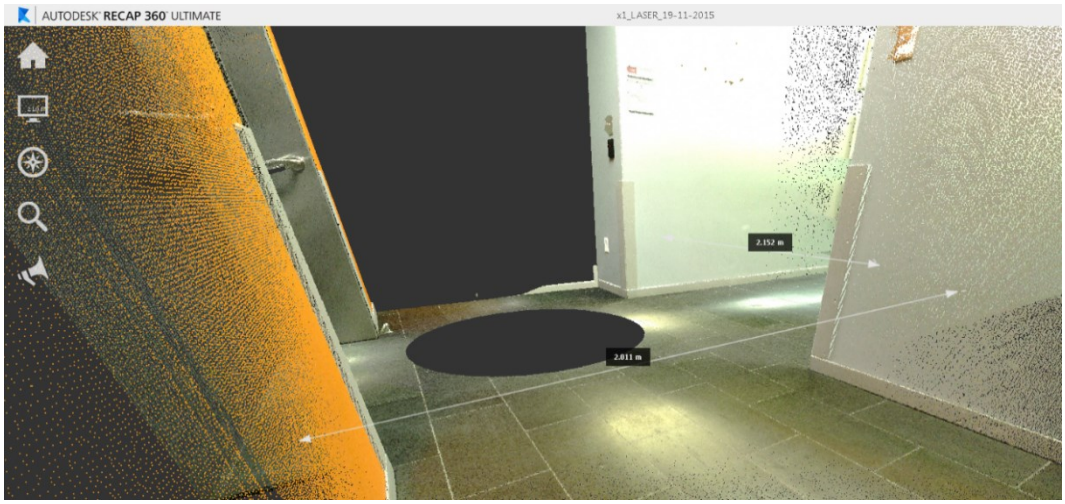

Figure 80: Measuring the dimensions of the EV building laser-based point cloud.

Table 21: Validation of the ground truth (case study II)

Location #	Actual dimensions (m)	Measured dimensions from the laser-based point cloud (m)	Difference (mm)	Error%
1	2.152	2.152	0.0	0.000%
2	2.987	2.985	2.0	0.067%
3	1.945	1.946	-1.0	0.051%
4	2.973	2.972	1.0	0.034%
5	1.830	1.831	-1.0	0.055%
6	2.985	2.985	0.0	0.000%
7	2.013	2.011	2.0	0.099%
8	2.985	2.983	2.0	0.067%
Average=			**0.6**	**0.047%**

Table 21 displays the actual and measured dimensions of 8 different locations in the EV building testing environment. From this table, it can be noticed that the average difference between the actual and measured is 0.6 mm. In addition, the average error was computed to be 0.047%. Therefore, the EV building laser-based point cloud can be used as the ground truth.

Control points

The first step towards conducting the deviation analysis was to align the UAS-based point cloud with the ground truth point cloud in a common coordinate system. To do this, 8 control points were placed in various locations throughout the EV building testing environment, before any data collection was done (see Figure 81). Later, after generating both the UAS- and laser-based point

clouds, 3 control points were matched between the different clouds to align them in a common coordinate system. Moreover, the remaining control points were compared between the UAS- and laser-based point clouds in the control point deviation analysis.

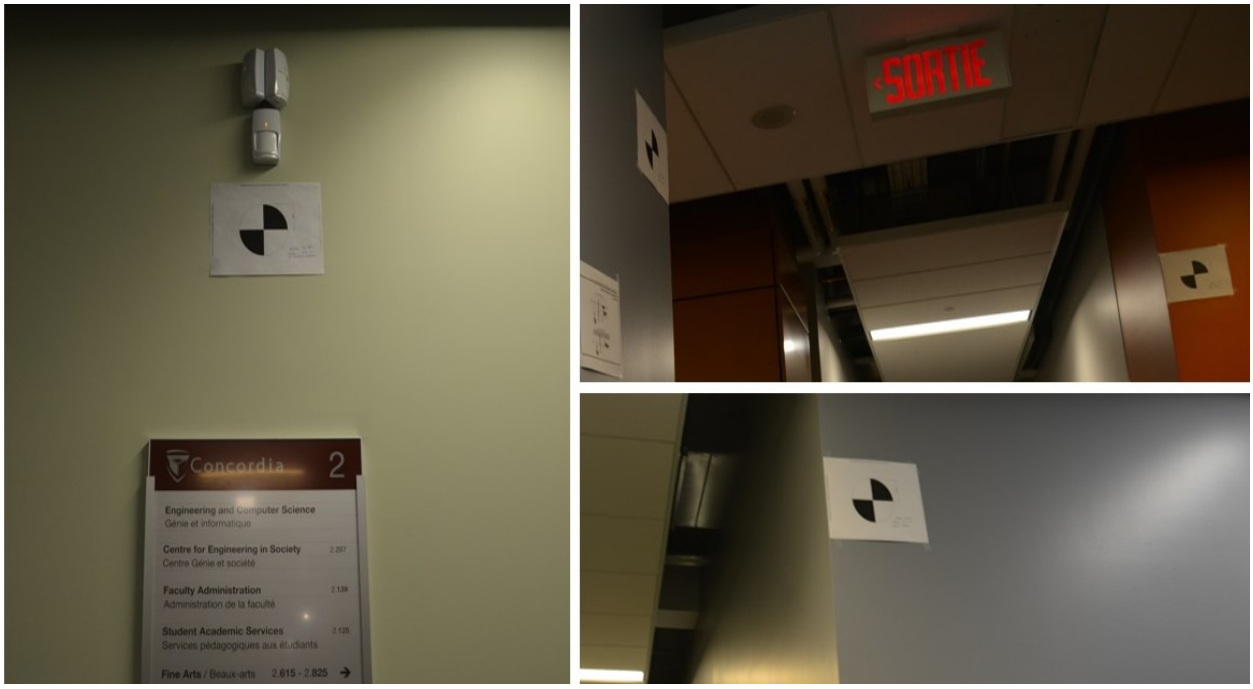

Figure 81: Control points placed in the EV building testing environment.

Point Cloud Deviation Analysis

In the point cloud deviation analysis, the distance between each point in the EV building UAS-based point cloud and its hypothetical corresponding location in the ground truth point cloud (i.e., the EV building laser-based point cloud) was measured using the CloudCompare software. The result was a scalar field that represents the deviation of each point (in the UAS-based point cloud) from the ground truth. This scalar field consists of 100 deviation classes, where each class represents a different range of deviation. Table 35 in appendix A shows the 100 deviation classes for the EV building UAS-based point cloud. These results were then further analyzed to show the percentage of points that fall within each deviation class (see Figure 82). Furthermore, Figure 83 shows the cumulative percentage of points per deviation class.

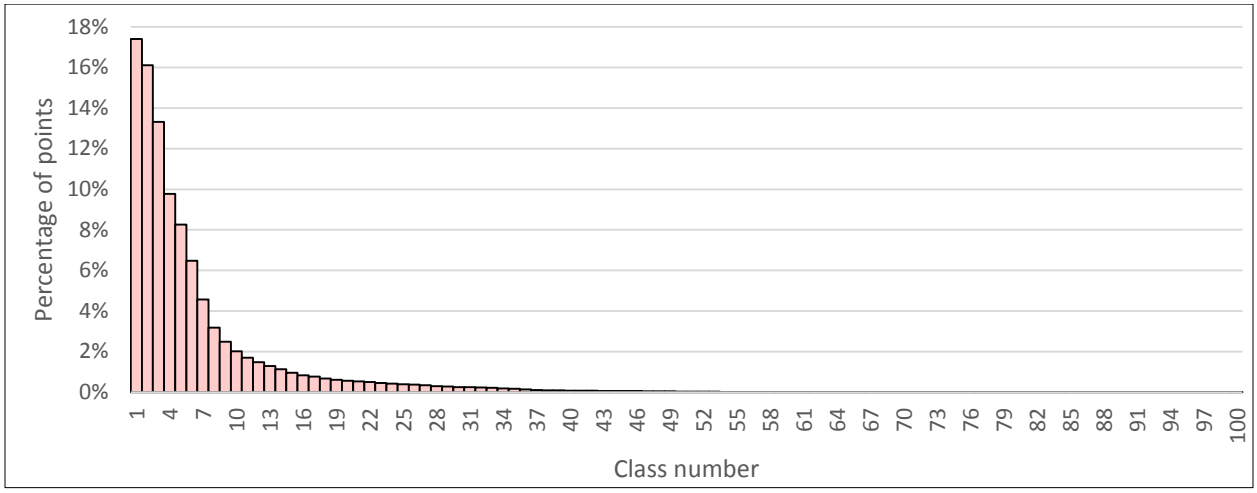

Figure 82: Percentage of points per deviation class –EV building UAS-based point cloud.

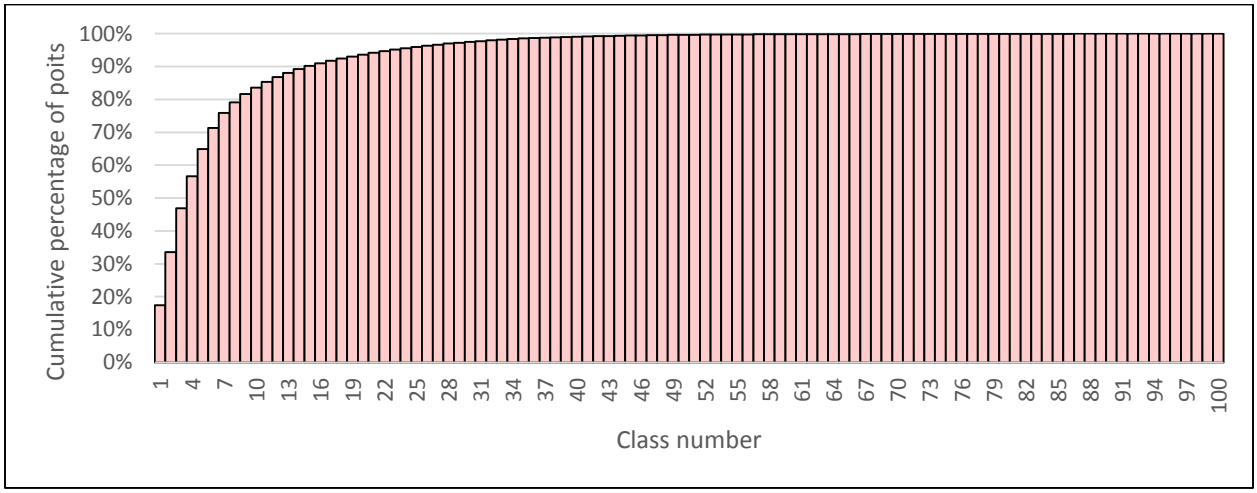

Figure 83: Cumulative percentage of points per deviation class – EV building UAS-based point cloud.

Control Point Deviation Analysis

In the control point deviation analysis, the coordinates of each control point in the EV building UAS-based point cloud and the ground truth point cloud were compared. This was done to find the deviation of each control point on the X, Y, and Z axis from the ground truth. Additionally, the absolute distance between the location of the control points in the UAS-based point cloud and in their location in the ground truth point cloud was also computed. Table 22 shows the results of the control point deviation analysis.

Table 22: Control point deviation analysis (case study II).

Control point #	ΔX (cm)	ΔY (cm)	ΔZ (cm)	Absolute distance (cm)
1	2.76	0.63	2.94	4.08
2 [a]	-	-	-	-
3	0.71	1.12	2.04	2.44
4	0.73	0.84	1.91	2.21
5 [a]	-	-	-	-
6	5.13	1.79	2.84	6.13
7 [a]	-	-	-	-
8	3.29	2.55	0.99	4.28
Maximum	**5.13**	**2.55**	**2.94**	**6.13**
Minimum	**0.71**	**0.63**	**0.99**	**2.21**
Average	**2.52**	**1.39**	**2.14**	**3.83**
Standard deviation	**1.87**	**0.78**	**0.79**	**1.59**

[a] The control points that were used for aligning the UAS-based point cloud with the ground truth point cloud.

4.3.4. Evaluation of Density

To evaluate the density of the EV building UAS-based point cloud, it was compared to the density of the EV-building laser-based point cloud. In doing this, ten 1m^2 sections were randomly taken at the UAS-based point cloud and the number of points was computed (see Figure 84). Next, identical sections were taken at the laser-based point cloud and the number of points was also computed (see Figure 85). Furthermore, the sections were then classified in accordance with their location, and distance from the laser scanner. These classifications are similar to the ones used in case study I (see section 4.2.4). Finally, Table 23 shows the number of points for each 1 m^2 section taken at the EV building UAS- and laser-based point clouds.

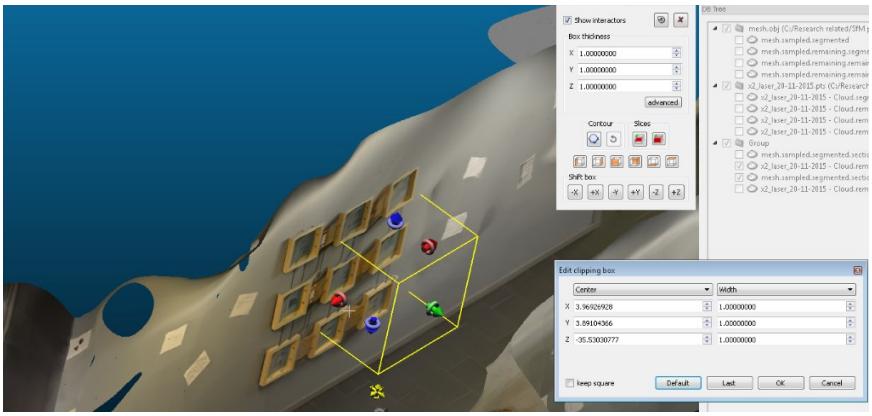

Figure 84: Sectioning the EV building UAS-based point cloud.

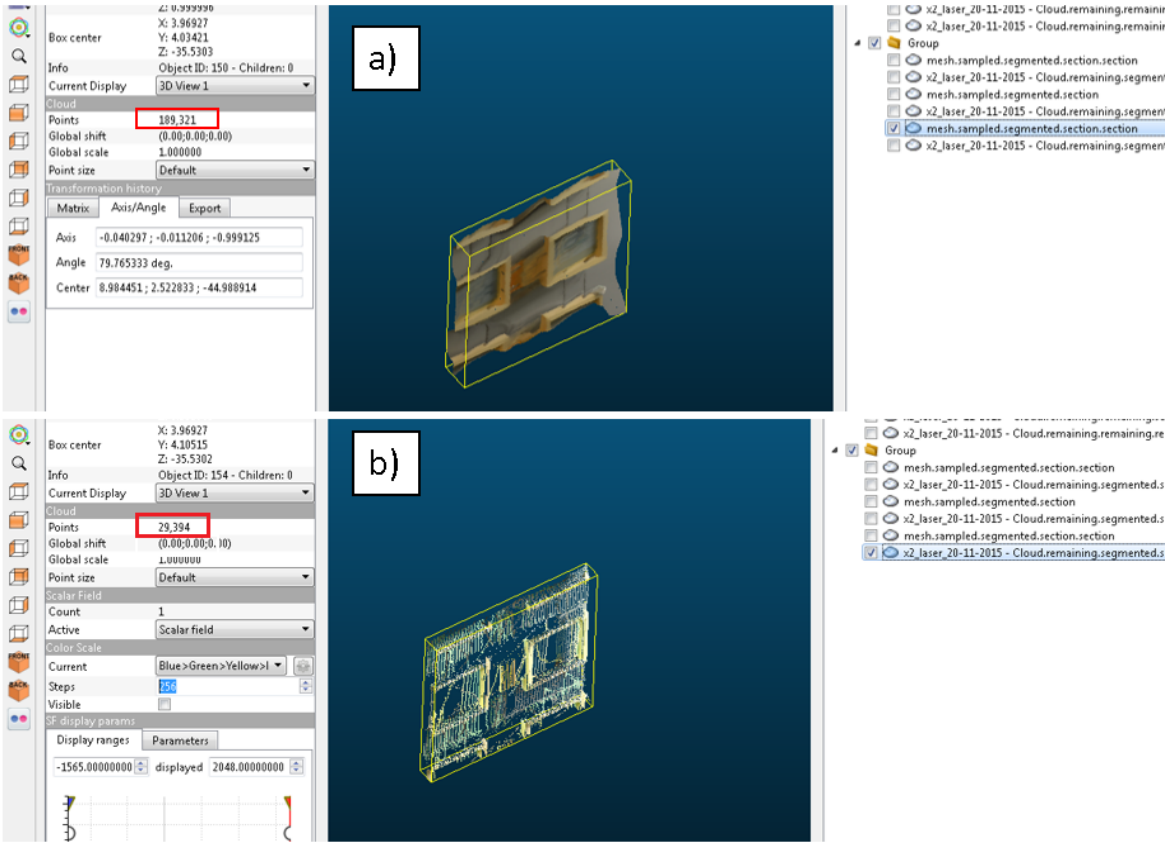

Figure 85. A sample of the 1 m^2 sections: a) at the UAS-based point cloud, b) at the laser-based point cloud.

Table 23: Number of points for each 1m^2 section (case study II).

Section #	Number of points in the UAS-based point cloud	Number of points in the laser-based point cloud	Location class	Distance class
1	179,272	356,053	Floor	v. close
2	189,321	29,394	Wall	v. far
3	180,576	161,621	Floor	close
4	193,156	1,207,979	Wall	v. close
5	185,450	51,852	Ceiling	far
6	183,777	1,752,233	Ceiling	v. close
7	199,625	78,571	Ceiling	far
8	183,826	53,572	Floor	far
9	185,931	129,260	Floor	close
10	191,719	102,940	Wall	close
Average	**187,265**	**392,348**		
Standard deviation	**6,229**	**594,695**		

4.3.5. Time-based Comparison

To perform a time-based comparison, the time required for generating the EV building UAS- and laser-based point clouds were documented while conducting the case study. Specifically, with respect to the UAS-based point cloud, the time required for setting up the visual markers and collecting the overlapping images was documented during the data collection stage. Additionally, the time required for processing the images and creating the UAS-based point cloud was also documented. Table 24 shows the time required for generating the EV building UAS-based point cloud. Moreover, regarding the laser-based point cloud, the time required for setting up the reference targets, scanning the testing environment, and registering the scans from the different positions were all recorded. Table 25 shows the time required for generating the EV building laser-based point clouds.

Table 24: Time required for generating the EV building UAS-based point cloud [a].

Setting up the visual markers (min)	Image acquisition (min)	Image filtration (min)	Upload-to-software [b] (min)	Manual registration (min)	Cloud processing (hr)	Total duration **excluding** cloud processing (hr)	Total duration **including** cloud processing (hr)
42.00	11.00	9.00	13.00	17.00	20.00	1.53	21.53

[a] The table is color-coded. Green belongs to the data collection stage, and yellow belongs to the data processing stage.

[b] Performed with a 19.86 Mbps internet upload speed (Ookla, 2015).

Table 25: Time required for generating the EV building laser-based point cloud.

Setting up the reference targets (min)	Scanning the testing environment (min)	Registration[1] (min)	Total duration (hr)
14	61	90	2.75

[a] The table is color-coded. Green belongs to the data collection stage, and yellow belongs to the data processing stage.

[b] Performed using a Lenovo E440. Technical specifications outlined in Table 6, page 56.

4.3.6. Cost-based Comparison

To perform a cost-based comparison, the cost of equipment and software used for creating the EV building UAS- and laser-based point clouds were recorded from official quotations and company websites. Additionally, the cost of labor needed for creating these point clouds was estimated as well. Table 26 shows the estimated cost of labor, in which the time needed for data collection and processing were added up, and multiplied by the hourly cost of labor ($20/hr). Note that the cloud processing time was excluded from the estimation of labor costs, because it is done automatically on the cloud computing technology. Subsequently, the labor costs were then added to the equipment and software costs to get the total cost of generating the EV building UAS- and laser-based point clouds (see Table 27).

Table 26: Estimated cost of labor (case study II).

Technique	Duration of data collection (hr)	Duration of data processing **excluding** cloud processing (hr)	hourly labor rate ($/hr) [a]	Cost of manpower ($)
UAS-based	0.9	0.7	20.0	30.7
laser-based	1.3	1.5	20.0	55.0

[a] Adopted from Dai et al. (2012)

Table 27: Cost-based comparison (case study II).

Technique	Equipment cost ($)	Software cost ($)	Cost of labor ($)	**Total**
UAS-based	2,637[a]	2,500[c]	31	**$5,168**
Laser-based	54,775[b]	9,625[d]	55	**$64,455**

[a] Acquired from an official invoice from Aircraft Modeler's Research Inc. (2015).

[b] Includes the cost of the Faro Focus 3D X130 laser scanner, a tripod, and the reference targets package. Acquired from an official invoice from Cansel Survey Equipment Ltd. (2015).

[c] $500/year; projected for five years. Acquired from Autodesk (2015).

[d] Acquired from an invoice from Cansel Survey Equipment Ltd. (2015).

CHAPTER 5: DISCUSSION AND LESSONS LEARNED

5.1. Accuracy

To measure the accuracy of the UAS-based point cloud in both studies, a deviation analysis was conducted on two levels: (a) a point cloud level, and (b) a control point level. In case study I, it can be noticed from the point cloud deviation analysis done on the Hall building UAS-based point cloud (see Table 34 and Figure 64), that the deviation of 80% of the points ranges between 0 and 8.8 cm from the ground truth. In addition, the deviation of 90% of the points ranges between 0 and 12.8 cm. In case study II, the point cloud deviation analysis done on the EV building UAS-based point cloud (see Table 35 and Figure 83) shows that the deviation range for 80% of the points is between 0 and 6.5 cm. Additionally, the deviation range for 90% of the points is between 0 and 11.3 cm. With respect to the control point deviation analysis done on the Hall building UAS-based point cloud (see Table 11), it can be noticed that the average deviation of the control points is 2.11 cm, 2.59 cm, and 1.84 cm on the X-, Y-, and Z-axis, respectively. Moreover, the average absolute distance between the control points in the Hall building UAS-based cloud and their corresponding locations in the ground truth point cloud is 3.99 cm. Regarding the control point deviation analysis done on the EV building UAS-based point cloud (see Table 22), the average deviation of the EV building control points is 2.52 cm, 1.39 cm, and 2.14 cm on the X-, Y-, and Z-axis, respectively. Also, the average absolute distance between the control points in the EV building UAS-based and their corresponding locations in the ground truth point clouds is 3.83cm

These results are of no surprise to the author since the error of image-based modeling has been reported by other research studies to be within the range of centimeters (Bhatla et al., 2012; Klein et al., 2012), as was the case in this paper. However, some points in the UAS-based point clouds suffered from extremely high deviation. For instance, in case study I, 1% of the points in the Hall building UAS-based point cloud had a deviation range between 38.5 and 80.3 cm. These high errors can be attributed to two things: windows, and occlusion. Figure 86 shows an example of the errors caused by windows, in which the window was not modeled correctly due to the incorrect depth information collected from the transparent glass.

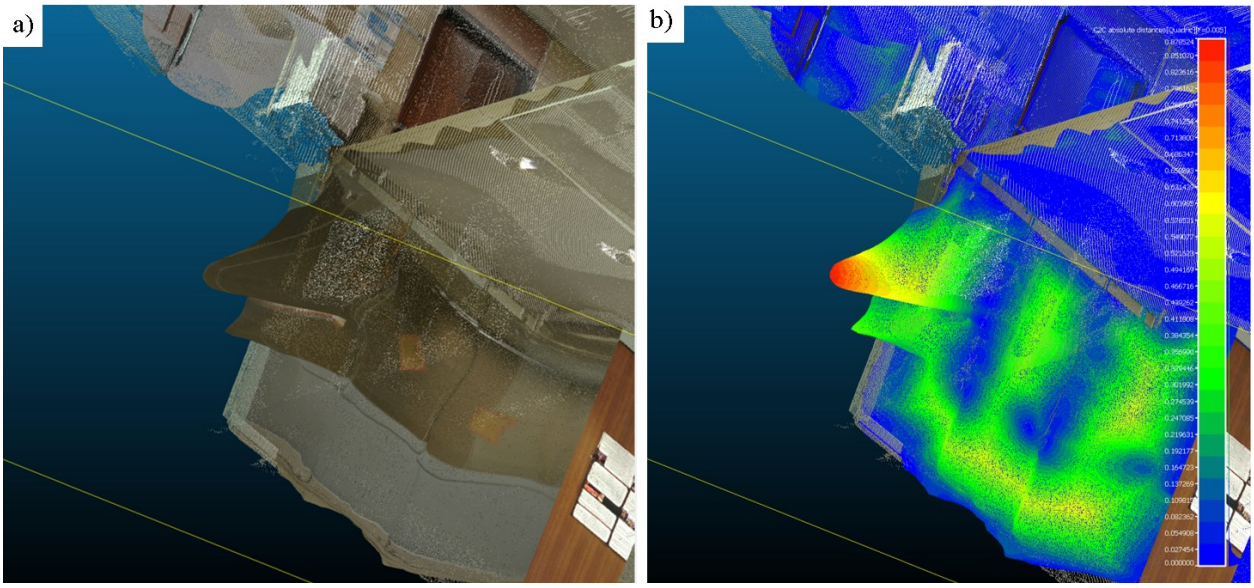

Figure 86: Errors caused by windows: a) the point cloud with color information, b) the point cloud with the deviation scalar field.

Furthermore, the high deviation values are also caused by occlusion. This issue mainly occurs when elements in the environment don't appear completely in the overlapping images due to the occlusion (i.e., blockage) from other elements. For example, in Figure 87 the side of the elevator didn't appear completely in the images because it was occluded by the column highlighted in red. As a result, the side of the elevator was not modeled completely, which caused high deviation values (see Figure 88)

Figure 87: Elevator partially occluded by the column highlighted in red.

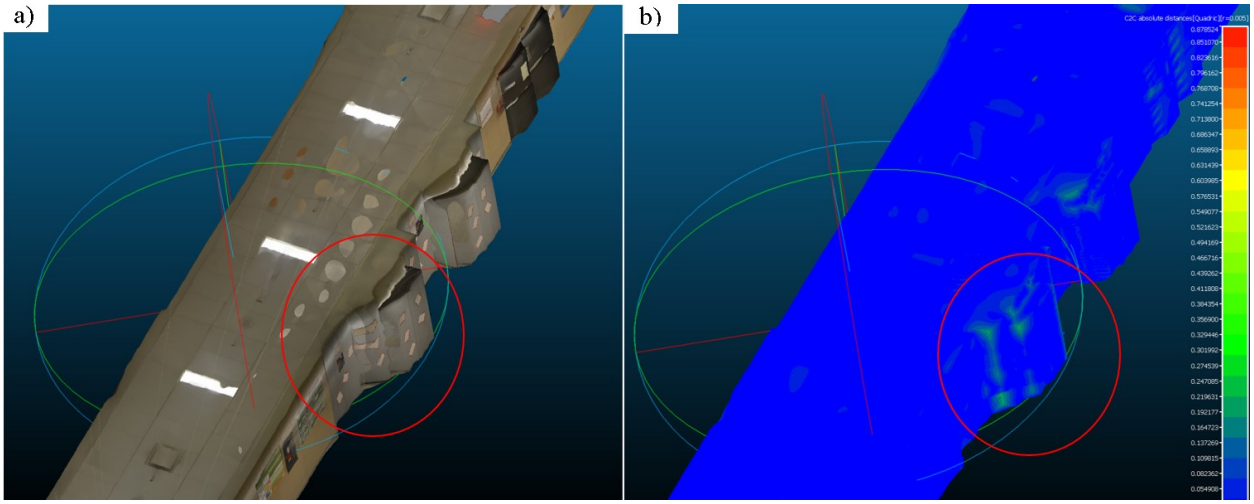

Figure 88: Example of the errors caused by occlusion: a) the point cloud with color information, b) the point cloud with the deviation scalar field.

5.2. Density

To evaluate the density of the UAS-based point clouds in the case studies, their density was compared to that of the laser-based point clouds. For case study I, the average density of the Hall building UAS-based point cloud is 77,106 pts/m^2, while the average density of the Hall building laser-based point cloud is 118,116 pts/m^2 (see Table 13). Regarding case study II, the average density of the EV building UAS-based point cloud is 187,265 pts/m^2, while the average density of the EV building laser-based point cloud is 392,348 pts/m^2 (see Table 23). Moreover, the overall findings from both case studies indicate that there is a strong correlation between the density of the laser-based point clouds and the location of the laser scanner. Specifically, the density of the laser-based point clouds was highest at the locations that were closest to the laser scanner and was lowest at the locations that were furthest from it. On the other hand, it was observed that the UAS-based point clouds had a consistent density throughout the model. Furthermore, at the sections that are very close to the laser scanner (0.1 to 0.5 m), the laser-based point clouds were significantly denser than the UAS-based point clouds. However, at the sections that very far from the scanner (2 to 4 m), the UAS-based point clouds were denser than the laser-based point clouds.

5.3. Time

To perform a time-based comparison, the time required for generating the UAS- and laser-based point clouds were documented while conducting the case studies. Table 28 summarizes the time required for generating the point clouds in each case study.

Table 28: Summary of the time required for generating the point clouds in each case study.

Point cloud	Duration of data collection (hr)	Duration of data processing **excluding** cloud processing (hr)	Duration of data processing **including** cloud processing (hr)
Hall – UAS-based	1.17	0.62	24.62
EV– UAS-based	0.88	0.65	20.65
Average UAS-based	1.03	0.63	22.63
Hall – laser-based	1.50	1.83	
EV – laser -based	1.25	1.50	
Average laser-based	1.38	1.67	

A key limitation in this comparison is the internet speed used to upload the images during the data processing of the UAS-based point clouds, in which if a different internet speed were to be used this time would be completely different. Furthermore, another limitation is the performance of the machine used for registering the laser-based point clouds. In this research, a Lenovo E440 fitted with a Solid State Drive (SSD) was used for registration. However, if the computer used was fitted with a Hard Disk Drive (HDD) the registration time would be significantly higher because SSDs are 3 times faster than HDDs.

5.3.1. Time-based Comparison for Data Collection

Table 28 summarizes the time required for the data collection in each case study. The results show that the data collection for the laser-based point clouds required 30% more time than the data collection for the UAS-based point clouds. The time-consuming nature of the laser-based modeling approach can be attributed to the bulkiness of its equipment. Namely, to model an environment completely, it should be scanned from several positions. For every scanning position, the tripod and the laser scanner will need to be moved and reassembled, which can be very time-consuming.

Moreover, as the complexity of the environment increases, rigorous planning of the scanner's location and the location of its reference targets will be required. For example, if a corridor and a room were to be modeled, 3 scans would be required: one in the corridor, one in the room, and one in the entrance to the room which is required for registering the two other scans together. Therefore, complex environments not only need rigorous planning of the scanning positions, but also require more scans, which makes laser-based modeling very time-consuming. On the other hand, UAS-based modeling doesn't require much planning and organization before starting the data collection. The only aspect that makes the data collection for the UAS-based point clouds time-consuming is the amount of visual markers required. If the environment is visually complex and has several features, then visual markers will not be required. However, if the environment is featureless (e.g., stucco walls with one uniform color), then a large number of visual markers will be required, which can be time-consuming.

5.3.2. Time-based Comparison for Data Processing

Table 28 also summarizes the time required for processing the point clouds in each case study. It can be observed from the results, that the data processing for the UAS-based point clouds took on average 0.63 hours when cloud processing was excluded. This was less than half the time needed for processing the laser-based point clouds (1.67 hours). However, when cloud processing was included, the processing of the UAS-based point clouds took on average of 22.63 hours, which was significantly more than the time needed for processing the laser-based point clouds (1.67 hours). Therefore, it can be concluded that cloud processing is particularly advantageous because all of the heavy processing is done on the cloud computing technology, and the computer can be used for other tasks. However, one drawback to this is that it is a time-consuming process.

5.4. Cost

Table 29: The cost of generating the point clouds in each case study.

Point cloud	Total cost
Hall – UAS-based	$ 5,173
EV– UAS-based	$ 5,168
Average UAS-based	**$ 5,171**
Hall – laser-based	$ 64,467
EV – laser -based	$ 64,455
Average laser-based	**$ 64,461**

Table 29 summarizes the estimated cost of generating the UAS- and laser-based clouds in case study I and case study II. The average cost of generating the UAS-based point clouds was estimated to be $5,171 while the average cost of generating the laser-based point clouds was estimated to be $64,461. Therefore, it can be concluded that affordability is one of the most attractive features in the UAS-based modeling approach because it is a fraction of the cost of laser-based modeling.

5.5. Limitations of UAS-based Modeling

In this section, any problems encountered while constructing the UAS-based point clouds were outlined and discussed. This was done to highlight any limitations related to the 3D modeling of indoor building environments using a UAS.

5.5.1. Effect of Using Visual Markers

To examine the importance of using visual markers in UAS-based modeling, the EV building testing environment was modeled twice. In the first modeling effort, the environment was modeled after adding unique visual markers to sections that were assumed to have a low number of features (see Figure 89). In the second attempt, the environment was modeled without adding any visual markers.

Figure 89: Placing visual markers before data collection.

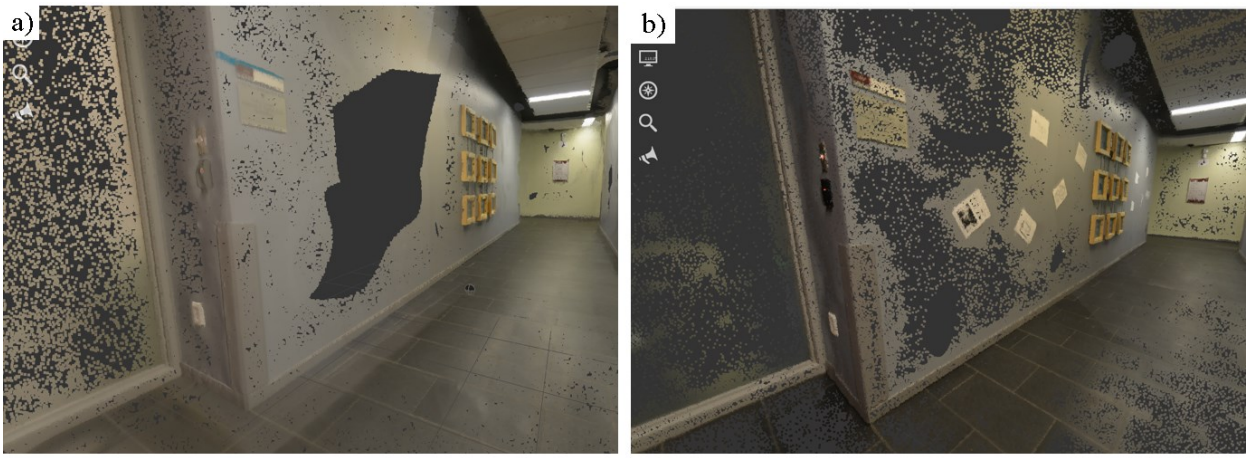

Figure 90: EV building UAS-based point cloud: a) before adding the visual markers, b) after adding the visual markers.

It can be noticed from Figure 90-a, that the wall was not fully modeled when there were no visual markers, but it was fully modeled when visual markers were added to it (Figure 90-b). This incomplete modeling was caused by the insufficient contrast and visual complexity (i.e., low number of features) of this wall section. Adding unique visual markers (e.g., random posters) to this wall increased the number of features available, which in turn increased the number of features matched and triangulated, leading to the adequate modeling of this section. Therefore, it can be concluded that the incomplete modeling of featureless surfaces is a key limitation of the UAS-based modeling approach. This issue can be mitigated by adding unique visual markers to featureless sections in order to artificially increase the number of features.

5.5.2. Incorrect Modeling of Visually Similar Sections

Another key limitation of UAS-based modeling is incorrect modeling of visually similar sections. This issue was encountered while constructing the EV building UAS-based point cloud because the environment includes two visually similar corridors (see Figure 91). The similarity between the wall on the right in the first corridor (see Figure 91-a) and the wall on the right in the second corridor (see Figure 91-b) has led to the incorrect matching of features. In other words, the features from the first corridor were matched with the features from the second corridor. Consequently, both corridors were modeled as one “merged” corridor (see Figure 92). This issue was solved by manually registering the images that suffered from this problem to the images that

appeared in their correct location (see Figure 93). Figure 94 shows the final EV building UAS-based point cloud after manual registration was done.

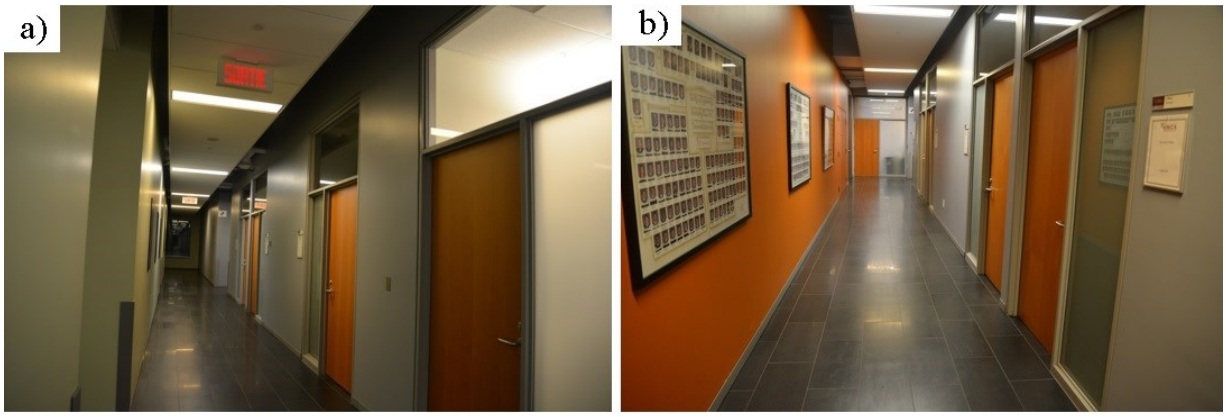

Figure 91: Two visually similar corridors in the EV building testing environment.

Figure 92: Merged point cloud of the two visually similar corridors.

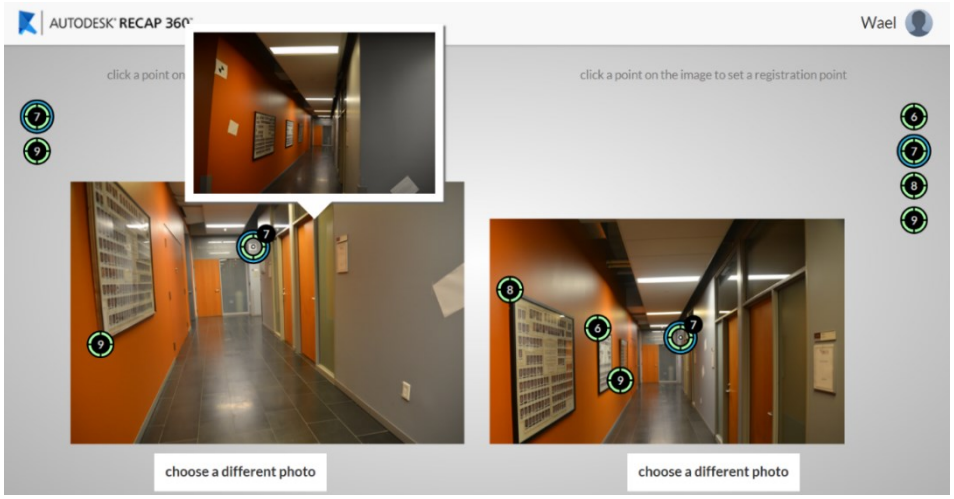

Figure 93: Manual registration of the two visually similar corridors.

Figure 94: The EV building UAS-based point cloud after manual registration was done.

5.5.3. Inability to Model Environments With Insufficient Lighting

Since the UAS-based modeling technique uses visible images to model the environment. Sufficient lighting must be available in the scene in order to model it. In some cases, sufficient lighting is not available in the environment (e.g., power blackouts, caves, etc.). To model in such conditions illumination must be provided artificially (i.e., use a flashlight for illumination during data collection). To study such cases, a small room (4 m x 10.2 m) in Concordia University was modeled twice. In the first experiment, data collection was done under normal lighting conditions (Figure 95). And in the second experiment, the lights were turned off, and data collection was done using the DJI Phantom 3 and an LED flashlight as a light source for the images (Figure 96). The point clouds from both experiments were then compared to a ground truth point cloud created using the Faro Focus 3D laser scanner.

Figure 95: The testing environment using normal lighting conditions

Figure 96: LED flashlight attached to the DJI Phantom 3 to collect images using low lighting conditions.

Accuracy evaluation

To investigate the effect of insufficient lighting conditions on the accuracy of the point clouds, a deviation analysis was conducted on two levels: a) point cloud deviation analysis, b) control point deviation analysis. This deviation analysis was done for both the UAS-based point

cloud using normal lighting conditions and the UAS-based point cloud using low lighting conditions (i.e., using the LED flashlight as the only light source).

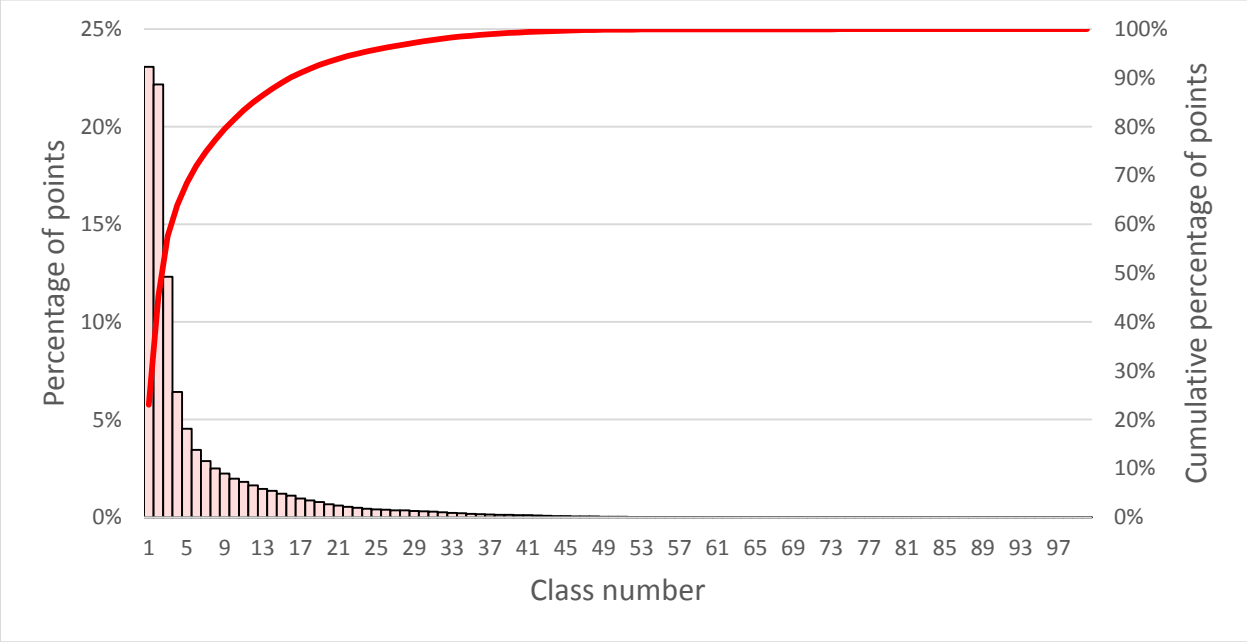

Figure 97: Point cloud deviation analysis for the UAS-based point cloud using normal lighting conditions.

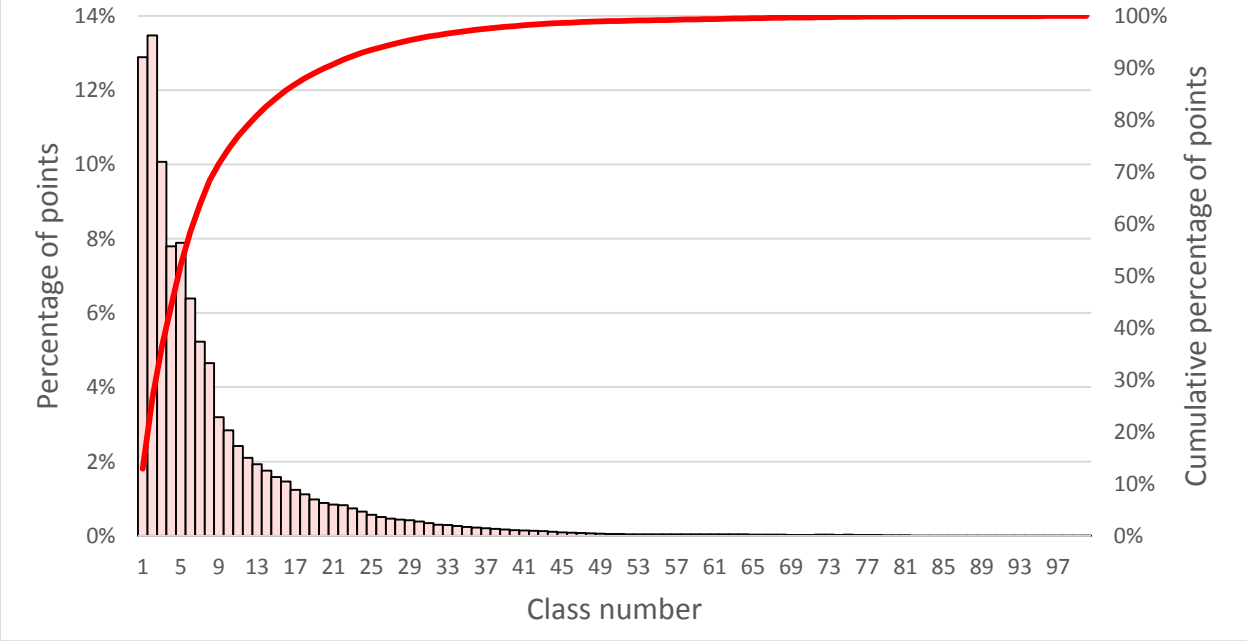

Figure 98: Point cloud deviation analysis for the UAS-based point cloud using low lighting conditions.

Table 30: Control point deviation analysis for the UAS-based point cloud using normal lighting conditions.

Control point #	ΔX (cm)	ΔY (cm)	ΔZ (cm)	Absolute distance (cm)
1	-	-	-	-
2	0.68	0.76	1.32	1.67
3	1.00	1.28	0.46	1.69
4	0.44	0.33	1.16	1.29
5	-	-	-	-
6	0.86	2.70	1.18	3.07
7	1.21	0.84	1.64	2.20
8	-	-	-	-
9	1.45	1.26	1.08	2.20
10	1.67	1.80	1.13	2.70
Maximum	**1.67**	**2.70**	**1.64**	**3.07**
Minimum	**0.44**	**0.33**	**0.46**	**1.29**
Average	**1.04**	**1.28**	**1.14**	**2.12**
Standard Deviation	**0.43**	**0.78**	**0.35**	**0.62**

Table 31: Control point deviation analysis for the UAS-based point cloud using low lighting conditions.

Control point #	ΔX (cm)	ΔY (cm)	ΔZ (cm)	Absolute distance (cm)
1	-	-	-	-
2	0.45	4.98	1.78	5.31
3	-	-	-	-
4	3.76	2.87	1.98	5.12
5	2.91	3.82	4.27	6.43
6	2.34	2.42	2.17	4.00
7	0.11	2.50	3.26	4.11
8	-	-	-	-
9	5.08	1.73	1.03	5.47
10	5.62	2.49	0.36	6.15
Maximum	**5.62**	**4.98**	**4.27**	**6.43**
Minimum	**0.11**	**1.73**	**0.36**	**4.00**
Average	**2.90**	**2.97**	**2.12**	**5.23**
Standard Deviation	**2.12**	**1.09**	**1.31**	**0.92**

From the point cloud deviation analysis it can be noticed that 80% of the points in the UAS-based point cloud using normal lighting conditions have a deviation of up to 7.16 cm from the ground truth (see Figure 97 and Table 36). 23% of those points have a deviation of 0.80 cm or less from the ground truth. In the case of the UAS-based point cloud using the low lighting conditions, 80% of the points in that point cloud have a deviation of up to 9.84 cm from the ground truth (see

Figure 98 and Table 37). 12% of those points have a deviation of 0.76 cm or less from the ground truth. From the control point deviation analysis, it can be noticed that the average absolute deviation of the control points in the UAS-based point cloud using normal lighting conditions is 2.12 cm from the ground truth (see Table 30). In the case of the UAS-based point cloud using low lighting conditions, the average absolute deviation is 5.23 cm from the ground truth (see Table 31). In sum, both deviation analyses show that lower lighting can slightly reduce the accuracy of the UAS-based point cloud, where the UAS-based point cloud using normal lighting conditions is slightly more accurate that the UAS-based point cloud constructed using the LED flashlight as an only light source.

Density evaluation

Table 32: Density analysis for UAS-based point clouds using different lighting conditions.

Section #	Number of points in section (normal lighting conditions)	Number of points in section (low lighting conditions)
1	166,714	180,894
2	169,809	173,602
3	170,888	168,806
4	182,945	169,964
5	173,874	181,217
Average	**172,846**	**174,897**
Standard Deviation	**5,544**	**5,273**

In order to investigate the effect of the different lighting conditions on the density of the UAS-based point clouds, five $1m^2$ sections were taken at various locations in each point cloud and the number of points was computed. It can be noticed from Table 32 that density of the UAS-based point cloud using normal lighting conditions is within the same range of the density of the UAS-based point cloud using low lighting conditions. Therefore, it can be concluded that the different lighting conditions do not affect the density of the UAS-based point cloud.

Time-based evaluation

Moreover, the different lighting conditions affected the number of images required for modeling the environment. In the case of normal lighting conditions 83 images were sufficient to model the environment completely. While in the case of low lighting conditions (i.e., using the

LED flashlight as the only light source) 136 images were required to model the environment. This is mainly because the number of features extracted from images with low light is significantly less than the number of features that can be extracted from properly illuminated images. Therefore, in order to model the environment with low lighting conditions extra images were taken. This increased number of images has in turn increased the data collection and data processing times for the point cloud under low lighting conditions. Table 33 shows the durations of data collection and data processing for the UAS-based point clouds under normal lighting conditions and low lighting conditions.

Table 33: Duration of data collection and data process under normal and low lighting conditions.

	Duration of data collection (Minutes)[1]	Duration of data processing (Hours)
Normal lighting conditions	6	8
Low lighting conditions	13	12

[1] Time needed for placing the visual markers was not included.

CHAPTER 6: SUMMARY AND CONCLUSION

Nowadays, billions of dollars are spent on managing as-built information during the O&M phase. Mainly, these increased costs are due to inefficiencies in processing, communicating, and revising as-built documents in the O&M phase (Gallaher et al., 2004). Thus, a more efficient way of handling as-built information is needed. Since BIMs have proven to be a valuable tool for the design and construction phases, many owners and facility managers believe that they can be beneficial for the O&M phase (McGraw-Hill Construction, 2014). Substituting traditional as-built documents with an as-built BIM can offer numerous benefits to the owner and facility management team. First, the as-built BIM can be shared on the cloud computing technology, in which each stakeholder is allowed to insert, add, extract, or modify information in the BIM, and share it with other stakeholders. This can facilitate efficient communication between the various stakeholders and reduce the overall time and cost of exchanging as-built information (Smith, 2007; Tang et al., 2010). Second, the use of as-built BIMs can enhance the visualization and analysis of proposed renovations, which can make the design and planning of future renovations more efficient (Tang et al., 2010; Woo et al., 2010). Last, as-built BIMs can be used for analyzing the facility's energy efficiency, which can help in designing energy efficient retrofits to accommodate sustainability guidelines and reduce the overall cost of energy consumption (Woo et al., 2010).

In current practice, the spatial information required to construct the as-built BIM is collected using laser distance measurers or measuring tapes in extensive manual field surveys (Klein et al., 2012). However, this process is extremely error-prone and time-consuming (Giel & Issa, 2011; Klein et al., 2012). An efficient alternative to manual field measurements is remote sensing (Giel & Issa, 2011; Klein et al., 2012). Remote sensing techniques use non-disruptive sensing equipment to 3D model the spatial information of the surrounding environment, and represent it in a 3D point cloud (Klein et al., 2011; Qu et al., 2014). The two most common remote sensing techniques are laser-based and image-based remote sensing (Klein et al., 2012). Nowadays, laser-based remote sensing is the most reliable technique for the 3D modeling of spatial information, because it can produce dense point clouds within an accuracy of 2 to 5 mm (Klein et al., 2012; Qu et al., 2014). Nonetheless, this technique is time-consuming and very expensive (Klein et al., 2012; Qu et al., 2014). On the other hand, image-based sensing is a cost-efficient and

user-friendly technique for the 3D modeling of spatial information (Bhatla et al., 2012; Golparvar-Fard et al., 2011; Klein et al., 2012).

To date, image-based sensing of indoor building environments has been conducted using images captured by handheld cameras, which requires the physical presence of personnel in the facility. However, if the images are captured via UAS, image-based sensing could be achieved remotely. With recent technological improvements, UAS have become a cost-effective and powerful tool for remote image acquisition (Siebert & Teizer, 2014). Thus, UAS-imagery is currently being used in several engineering fields, such as inspection, disaster response and assessment, agricultural analysis, surveying, among others. Nevertheless, to the author's best knowledge it is still not clear whether images collected by UAS can be used to 3D model the spatial information of indoor building environments.

Using a UAS for the 3D modeling of indoor building environments is expected to have several advantages. Firstly, the UAS can be used for remote image acquisition and modeling of dangerous environments (e.g., nuclear plans) without jeopardizing the safety of staff. Secondly, the UAS can be used to remotely model the critical building components of facilities that were affected by a disaster (e.g., earthquake, bombing). These models can be used to identify cracks and defects in such critical components, which can then be used to assess the facility's stability and ensure the safety of the rescue personnel in search and rescue missions. Thirdly, the UAS can be used to aerially capture images of large facilities (e.g., warehouse, factory), which can enable effective modeling of such facilities. The typical image acquisition using handheld cameras can be inefficient in such large facilities because it requires numerous images to capture all parts of the environment. In contrast, a UAS allows for effective image acquisition in such situations, as the environment can be captured more efficiently via aerial images. Lastly, the UAS can be used to collect images of areas that are inaccessible by foot (e.g., the top of large machinery), which can improve the quality and completeness of the generated 3D model.

The purpose of this thesis was two-fold. The first purpose was to test the feasibility of 3D modeling indoor building environments using images captured by a UAS. The second was to evaluate the effectiveness of modeling using the UAS in terms of accuracy, density, time, and cost. To achieve these objectives, two case studies were conducted: (1) the 12th floor of the Hall

building, and (2) the 2nd floor of the EV building, at Concordia University. In both studies, the first step was to collect overlapping images of the testing environment using a commercially available UAS (i.e., DJI Phantom 3 Professional). These images were then imported to the commercial software Autodesk ReCap 360 to generate the UAS-based 3D point cloud. Since laser scanning is considered the most accurate and reliable remote sensing technique available today, a laser-based 3D point cloud served as the ground truth for this research. To generate the laser-based point cloud, the Faro Focus 3D X 130 laser scanner was deployed to scan the testing environment. Later, in the evaluation and comparison stage, the UAS-based point cloud was compared to the laser-based point cloud in terms of accuracy, density, time, and cost, to highlight the effectiveness of UAS-based 3D modeling. Finally, any issues encountered while constructing the UAS-based point cloud were outlined and discussed in order to highlight the limitations of using a UAS for the 3D modeling of indoor building environments.

For the accuracy measurement, the laser-based point cloud was used as the ground truth. Before it was deemed to be the ground truth, its accuracy was confirmed by comparing its dimensions with the actual dimensions of the testing environment. Subsequently, the laser-based point cloud was registered in a common coordinate system with the UAS-based point cloud. Thereafter, the open source software CloudCompare was used to conduct a deviation analysis on two levels: (a) a point cloud level and (b) a control point level. For the point cloud deviation analysis the distance between each point in the UAS-based cloud and its hypothetical corresponding location in the laser-based point cloud (i.e., the ground truth) was computed. The point cloud deviation analysis results showed that 80% of the points in the Hall building UAS-based point cloud had a deviation range between 0 and 8.8 cm. Moreover, 80% of the points in the EV building UAS-based point cloud had a deviation range between 0 and 6.5 cm. For the control point deviation analysis, the control points were first placed in various locations throughout the testing environment before any data collection was done. Then, after generating the UAS-based and laser-based point clouds, the deviation of each control point was analyzed. This was achieved by comparing the Cartesian coordinates of each control point in the UAS-based cloud with its coordinates in the laser-based point cloud. In addition, the control points were further analyzed by measuring the distance between their location in the UAS-based point cloud and their location in the laser-based point cloud. For the first case study, the results indicated that the control points in

the Hall building had an average deviation (from the ground truth) of 2.11 cm, 2.59 cm, and 1.84 cm on the X-, Y-, and Z-axis, respectively. The average absolute distance between the control points' locations (in the UAS-based cloud) and their corresponding locations in the ground truth (i.e., laser-based point cloud) was 3.99 cm. Furthermore, in the second case study, the control point deviation analysis showed that the control points in the EV building UAS-based point cloud had an average deviation (from the ground truth) of 2.52 cm, 1.39 cm, and 2.14 cm on the X-, Y-, and Z-axis, respectively. The average absolute distance between the control points and their corresponding locations in the ground truth was 3.83 cm. Overall, the results of this accuracy analysis were consistent with previous research (e.g., Bhatla et al., 2012; Klein et al., 2012) that documented that image-based remote sensing had an error range within centimeters.

Regarding the density evaluation, the density of the UAS-based point cloud was compared to that of the laser-based point cloud. To accomplish this, ten 1 m^2 sections were randomly taken at different locations throughout the UAS-based point cloud, and the number of points was computed for each section. Second, identical 1 m^2 sections were taken in the laser-based point cloud and the number of points was also computed to be compared with those from the UAS-based point cloud. The results of this comparison for the first case study showed that the average density of the Hall building UAS-based point cloud was 77,106 pts/m^2 while the average density of the laser-based point cloud was 118,116 pts/m^2. For the second case study, the results showed that the average density of the EV building UAS-based point cloud was 187,265 pts/m^2, and the average density of the laser-based point cloud was 392,348 pts/m^2. The overall findings from both case studies indicated that there was a strong correlation between the density of the laser-based point clouds and the location of the laser scanner. Specifically, the density of the laser-based point cloud was highest at the locations that were closest to the laser scanner and was lowest at the locations that were furthest from it. On the other hand, it was observed that the UAS-based point cloud had a consistent density throughout the model.

With respect to the time-based comparison, the time needed for creating the UAS-based and the laser-based point clouds were recorded. This included the time required for on-site data collection and the necessary time for data processing in the office. When the data collection time was compared, the results indicated that the laser-based point clouds required approximately 30%

more time (for data collection) than the image-based point clouds. When comparing the data processing time, the results suggested that data processing for the UAS-based point clouds took on average 0.63 hours when cloud processing (i.e., the time required for automatically generating the UAS-based point cloud on the cloud computing technology) was excluded, which is less than half the time needed to process the laser-based point clouds (1.67 hours). However, when cloud processing was included, data processing for the UAS-based point clouds took on average 22.63 hours, which is significantly more than the time needed for processing the laser-based point clouds. Therefore, it can be concluded that cloud processing is particularly advantageous because all of the heavy processing is done on the cloud computing technology, and the computer can be used for other tasks. However, one drawback to this is that it is a time-consuming process.

In the cost-based comparison, the cost of equipment, software, and labor was estimated for each modeling approach. The average cost of constructing the UAS-based point clouds was estimated to be $5,171 while the average cost of constructing the laser-based point clouds was $64,461. These results clearly indicate that affordability is one of the most attractive features in UAS-based modeling because it is a fraction of the cost of laser-based modeling.

Finally, any issues encountered while constructing the UAS-based point clouds were outlined and discussed to highlight any limitations related to this modeling approach. Since SfM depends on the presence of features, visual markers were always added to featureless surfaces within the environment before starting the image acquisition for the UAS-based point clouds. To examine the importance of using visual markers in UAS-based modeling, the EV building testing environment was modeled twice: (a) once with the presence of visual markers on featureless surfaces, and (b) once without adding any visual markers. After comparing both point clouds, UAS-based modeling was not able to fully model the environment without visual markers. Therefore, this is a key limitation of UAS-based modeling because featureless surfaces (e.g., stucco walls with one solid color) within the environment will not be fully modeled. Another key limitation of UAS-based modeling is the incorrect modeling of visually similar sections. This issue was encountered while constructing the EV building UAS-based point cloud because the EV testing environment includes two visually similar corridors. This similarity has led to the incorrect matching of features, where the features from one corridor were matched to features from another corridor. As a result,

both corridors were modeled as one "merged" corridor. This issue was mitigated by manually registering the images that caused this problem to the images that were correctly modeled in their location. The final limitation that was investigated was the inability of the UAS-based modeling technique to model environments with insufficient lighting. To study this limitation, a small room in Concordia University was modeled twice, once with the presence of normal lighting conditions, and once with using an LED flashlight as the only light source. The accuracy of these models was then evaluated by comparing them to a ground truth model of the room that was constructed using a laser scanner. According to the results of this evaluation the accuracy of the UAS-based point cloud is slightly reduced due to low lighting conditions. For instance, the point cloud deviation analysis showed that the deviation of 80% of the points in the UAS-based point cloud using low lighting conditions (i.e., using the LED flashlight as the only light source) was 37% more than the deviation of 80% of the points in the UAS-based point cloud using normal lighting conditions. To investigate the effects of low lighting conditions of the density of the UAS-based point clouds five $1m^2$ sections were taken at various locations in each point cloud and the number of points was computed. The results of this analysis showed that the different lighting conditions have no significant effect on the density of the UAS-based point cloud. For example, the average density of the UAS-based point cloud using normal lighting conditions was 172,846 pts/m^2, which was quite close to that of the UAS-based point cloud using low lighting conditions (174,897 pts/m^2). Finally, the effect of the different lighting conditions was investigated in terms of time. This was done by comparing the data collection and data processing times required for generating each point cloud. It can be noticed from Table 33 that the UAS-based point cloud using low lighting conditions required double the time for data collection and 50% more time for data processing than the UAS-based point cloud under normal lighting conditions. This was caused by the larger number of images required to generate the UAS-based point cloud using low lighting conditions, where it required 64% more images than the UAS-based point cloud using normal lighting conditions. This increased number of images was caused by the low number of features that can be extracted from the images with low light. Therefore, to model the environment with low lighting conditions extra images were taken of the environment, which increased the data collection and data processing times.

These studies demonstrate that UAS-based modeling is able to model the spatial information of indoor building environments with dense point clouds and with acceptable accuracy. Moreover, these studies show that 3D modeling of spatial information with a UAS can be a time- and cost-effective approach. While the present research focused solely on spatial information, future research would benefit from a focus on improving the UAS by mounting other sensors on it to enable the collection of other types of information. For example, if the UAS is equipped with an infrared (IR) camera, it can be used to collect the facility's thermal information. This information could then be fused with the 3D point cloud (from the digital camera) to generate a 3D thermal model. 3D thermal models enable engineers to detect air infiltration and heat losses from the building envelope, and simulate the facility's energy efficiency. This can facilitate the design of energy efficient retrofits that can reduce the facility's overall energy consumption. In turn, this can reduce the overall energy cost, and decrease the amount of pollutants used to power the facility. Furthermore, future research could concentrate on using the UAS for specific applications. For example, the UAS can be used for post-disaster modeling without endangering human life. In fact, search and rescue missions inside a facility that is affected by a disaster (e.g., earthquake, bombing, etc.) can be very dangerous to the life of the rescue personnel. This is mainly due to the high degree of uncertainty in regards to the facility's stability. Therefore, a method could be developed to use the UAS for remotely modeling critical building components (e.g., concrete columns) after the occurrence of a disaster. These models can be used to identify cracks and defects in such critical components, which can be used to assess the facility's stability and ensure the safety of the rescue personnel in search and rescue missions. These are just a few examples of how UAS can be utilized to enhance the different engineering fields. It is evident that with today's rapidly evolving and improving technology, the possibilities are limitless.

BIBLIOGRAPHY

AIBOTIX (2015). Discover the possibilities of UAV drones. Retrieved from https://www.aibotix.com/en/applications.html

Aircraft Modeler's Research Inc. (2015). *Official invoice.* Company website https://amr-rc.com/contact.html

Autodesk (2015). About Working With Point Clouds. Retrieved from http://help.autodesk.com/view/ACD/2015/ENU/?guid=GUID-C0C610D0-9784-4E87-A857-F17F1F7FEEBE

Autodesk ReCap 360 (version 2.0) [Computer software]. Autodesk (2015). Retrieved from https://recap360.autodesk.com/

Ball, M. (2014). Building information modeling for the win: Top 10 benefits of BIM. Retrieved from http://lineshapespace.com/building-information-modeling-top-10-benefits-of-bim/

Bhatla, A., Choe, S. Y., Fierro, O., & Leite, F. (2012). Evaluation of accuracy of as-built 3D modeling from images taken by handheld digital cameras. *Automation in Construction, 28*, 116-127.

Boehler, W., Vicent, M. B., & Marbs, A. (2003). Investigating laser scanner accuracy. *The International Archives of Photogrammetry, Remote Sensing and Spatial Information Sciences, 34*(Part 5), 696-701.

Cansel Survey Equipment Ltd. (2015). *Official invoice*. Company website https://www.cansel.ca/

Carvajal, F., Agüera, F., & Pérez, M. (2011). Surveying a landslide in a road embankment using unmanned aerial vehicle photogrammetry. Paper presented at the *International Conference on Unmanned Aerial Vehicle in Geomatics (UAV-g),* 14-16.

CloudCompare. (2015). *CloudCompare version 2.6.1: User manual*. Retrieved from http://www.danielgm.net/cc/doc/qCC/CloudCompare%20v2.6.1%20-%20User%20manual.pdf

CloudCompare (version 2.6.2) [GPL software]. EDF R&D, Telecom ParisTech (2015). Retrieved from http://www.cloudcompare.org/

Colomina, I., & Molina, P. (2014). Unmanned aerial systems for photogrammetry and remote sensing: A review. *ISPRS Journal of Photogrammetry and Remote Sensing, 92*, 79-97.

Cyrill Stachniss. (Jul 9, 2015). Photogrammetry I - 08a - matching - cross correlation (2015).

D. Smith. (2007). An Introduction to Building Information Modeling. Journal of Building Information Modeling, 12-14.

Dai, F., & Lu, M. (2010). Assessing the accuracy of applying photogrammetry to take geometric measurements on building products. *Journal of Construction Engineering and Management.*

Dai, F., Rashidi, A., Brilakis, I., & Vela, P. (2012). Comparison of image-based and time-of-flight-based technologies for three-dimensional reconstruction of infrastructure. *Journal of Construction Engineering and Management,* 69-79

DJI. (2015). *Phantom 3 professional: User manual*. Retereieved from http://download.dji-innovations.com/downloads/phantom_3/en/Phantom_3_Professional_User_Manual_v1.0_en.pdf

Eisenbeiß, H. (2009). *UAV photogrammetry*. (Unpublished PhD dissertation). University of Technology Dresden, Zurich, Switzerland.

Faro Technologies Inc. (2011). *FARO Laser Scanner Focus3D: User Manual*. Retrieved from ftp://12.166.64.163/Faro/e866_faro_laser_scanner_focus3d_manual_en[1].pdf

Faro Technologies Inc. (2014). *FARO Focus3D X 130: Technical sheet*. Retrieved from http://www.faro.com/products/3d-surveying/laser-scanner-faro-focus-3d/downloads#Download

Gallaher, M., O'Connor, A., Dettbarn, J., & Gilday, L. (2004). *Cost analysis of inadequate interoperability in the U.S. capital facilities industry*. (NIST GCR 04-867). Gaithersburg, MD: National Institute of Standards and Technology. doi:http://dx.doi.org/10.6028/NIST.GCR.04-867

Giel, B., & Issa, R. (2011). Using laser scanning to access the accuracy of as-built BIM. *Computing in Civil Engineering (2011),* 665-672.

Golparvar-Fard, M., Bohn, J., Teizer, J., Savarese, S., & Peña-Mora, F. (2011). Evaluation of image-based modeling and laser scanning accuracy for emerging automated performance monitoring techniques. *Automation in Construction, 20*(8), 1143-1155.

Höfle, B., & Hollaus, M. (2010). Urban vegetation detection using high density full-waveform airborne lidar data-combination of object-based image and point cloud analysis. na.

Huber, D., Akinci, B., Oliver, A. A., Anil, E., Okorn, B. E., & Xiong, X. (2011). Methods for automatically modeling and representing as-built building information models. Paper presented at the *Proceedings of the NSF CMMI Research Innovation Conference.*

Jizhou, W., Zongjian, L., & Chengming, L. (2004). Reconstruction of buildings from a single UAV image. Paper presented at the *Proc. International Society for Photogrammetry and Remote Sensing Congress,* 100-103.

Jung, J., Hong, S., Jeong, S., Kim, S., Cho, H., Hong, S., & Heo, J. (2014). Productive modeling for development of as-built BIM of existing indoor structures. *Automation in Construction, 42*, 68-77.

Klein, L., Li, N., & Becerik-Gerber, B. (2011). Comparison of image-based and manual field survey methods for indoor as-built documentation assessment. *Computing in civil engineering (2011)* (pp. 59-66) ASCE Publications.

Klein, L., Li, N., & Becerik-Gerber, B. (2012). Imaged-based verification of as-built documentation of operational buildings. *Automation in Construction, 21*, 161-171.

Lato, M. J. (2010,). Remote monitoring of deformation using terrestrial laser scanning (TLS or terrestrial LiDAR). *Geotechnical Instrumentation News*, 30(1), 27.

Lowe, D. G. (2004). Distinctive image features from scale-invariant keypoints. *International Journal of Computer Vision, 60*(2), 91-110.

MarketsandMarkets. (2014). Unmanned aerial vehicle (UAV) market by class, subsystem, application, funding, & by payload - forecast & analysis from 2014 to 2020. (AS 2802). doi:http://www.marketsandmarkets.com/Market-Reports/unmanned-aerial-vehicles-uav-market-662.html

McGraw-Hill Construction. (2012). *The business value of BIM in north america: Multi-year trend analysis and user ratings (2007–2012)*. (Electronic). doi:http://analyticsstore.construction.com/index.php/2012-business-value-of-bim-in-north-america-smartmarket-report.html

McGraw-Hill Construction. (2014). *The business value of BIM for owners*. (Electronic). doi:http://analyticsstore.construction.com/index.php/smartmarket-reports/BIMforOwnersSMR.html

Metni, N., & Hamel, T. (2007). A UAV for bridge inspection: Visual servoing control law with orientation limits. *Automation in Construction, 17*(1), 3-10.

Niethammer, U., Rothmund, S., Schwaderer, U., Zeman, J., & Joswig, M. (2011). Open source image-processing tools for low-cost UAV-based landslide investigations. *Int. Arch. Photogramm. Remote Sens. Spat. Inf. Sci, 38*(1), C22.

O'Day, E. (2013). 3D laser scanning: Different type of scanners. Retrieved from http://ideatesolutions.blogspot.ca/2013/07/3d-laser-scanning-different-type-of.html

Okorn, B., Xiong, X., Akinci, B., & Huber, D. (2010). Toward automated modeling of floor plans. In *Proceedings of the Symposium on 3D Data Processing, Visualization and Transmission* (Vol. 2).

Ookla. (Nov 27, 2015). Speed test. Retrieved from http://www.speedtest.net/

Qu, T., Coco, J., Rönnäng, M., & Sun, W.Challenges and trends of implementation of 3D point cloud technologies in building information modeling (BIM): Case studies. Paper presented at the *Computing in Civil and Building Engineering (2014),* 809-816.

Quirk, V. (2012). A brief history of BIM. Retrieved from http://www.archdaily.com/302490/a-brief-history-of-bim

Rasam, A. R. A., Hamid, N. A., Hamid, M. Z., Maarof, I., & Samad, A. M. (2013). 3D photorealistic modeling of university building using digital close range photogrammetry. Paper presented at the *Control and System Graduate Research Colloquium (ICSGRC), 2013 IEEE 4th,* 147-151.

Rau, J., Jhan, J., Lo, C., & Lin, Y. (2011). Landslide mapping using imagery acquired by a fixed-wing UAV. *Int.Arch.Photogramm.Remote Sens.Spat.Inf.Sci, 38*, 1-C22.

Remondino, F., Barazzetti, L., Nex, F., Scaioni, M., & Sarazzi, D. (2011). UAV photogrammetry for mapping and 3d modeling–current status and future perspectives. *International Archives of the Photogrammetry, Remote Sensing and Spatial Information Sciences, 38*(1), C22.

Rufino, G., & Moccia, A. (2005). Integrated VIS-NIR hyperspectral/thermal-IR electro-optical payload system for a mini-UAV. *Infotech@ Aerospace,* 1-9.

Siebert, S., & Teizer, J. (2014). Mobile 3D mapping for surveying earthwork projects using an unmanned aerial vehicle (UAV) system. *Automation in Construction, 41*, 1-14.

Snavely, K. N. (2008). *Scene reconstruction and visualization from internet photo collections.* (Unpublished PhD dissertation). University of Washington, Washington, USA.

Snavely, N., Simon, I., Goesele, M., Szeliski, R., & Seitz, S. M. (2010). Scene reconstruction and visualization from community photo collections. *Proceedings of the IEEE, 98*(8), 1370-1390.

Tang, P., Huber, D., Akinci, B., Lipman, R., & Lytle, A. (2010). Automatic reconstruction of as-built building information models from laser-scanned point clouds: A review of related techniques. *Automation in Construction, 19*(7), 829-843.

The National Building Specification [NBS]. (2014). *NBS national BIM report 2014.* (Annual report). doi:http://www.thenbs.com/topics/bim/articles/index.asp

Thoeni, K., Giacomini, A., Murtagh, R., & Kniest, E. (2014). A comparison of multi-view 3D reconstruction of a rock wall using several cameras and a laser scanner. *Int.Arch.Photogramm.Remote Sens.Spat.Inf.Sci, 45*, 573-580.

Thompson, M. M. (1966). Manual of photogrammetry (3d ed.). Falls Church, Va.: American Society of Photogrammetry.

Triggs, B., McLauchlan, P. F., Hartley, R. I., & Fitzgibbon, A. W. (2000). Bundle adjustment—a modern synthesis. *Vision algorithms: Theory and practice* (pp. 298-372) Springer.

Trimble RealWroks (version 10.0.2.414) [Computer software] .Trimble (2015). Retrieved from http://www.trimble.com/3d-laser-scanning/realworks.aspx

Tsai, F., Wu, T., Lee, I., Chang, H., & Su, A. Y. Reconstruction of indoor models using point clouds generated from single-lens reflex cameras and depth images.

Tzedaki, V., & Kamara, J. (2013). Capturing as-built information for a BIM environment using 3D laser scanner: A process model. *AEI 2013,* 486-495.

Wefelscheid, C., Hänsch, R., & Hellwich, O. (2011). Three-dimensional building reconstruction using images obtained by unmanned aerial vehicles. *International Archives of the Photogrammetry, Remote Sensing and Spatial Information Sciences, 38*, 1.

Westoby, M., Brasington, J., Glasser, N., Hambrey, M., & Reynolds, J. (2012). 'Structure-from-Motion'photogrammetry: A low-cost, effective tool for geoscience applications. *Geomorphology, 179*, 300-314.

Woo, J., Wilsmann, J., & Kang, D. (2010). Use of as-built building information modeling. In *Construction Research Congress, 1,* 538-547.

Xie, F., Lin, Z., Gui, D., & Lin, H. (2012). Study on construction of 3D building based on UAV images. *ISPRS-International Archives of the Photogrammetry, Remote Sensing and Spatial Information Sciences, 1*, 469-473.

APPENDIX A: RESULTS TABLES

Table 34: Point cloud deviation classes for the Hall building UAS-based point cloud (case study I).

Class #	Range start(cm)	Range end (cm)	Number of points	Percentage	Cumulative
1	0.00	0.80	7334122	20.9124%	20.9124%
2	0.80	1.61	3927369	11.1984%	32.1109%
3	1.61	2.41	2853085	8.1352%	40.2461%
4	2.41	3.21	2459764	7.0137%	47.2598%
5	3.21	4.02	2290800	6.5320%	53.7918%
6	4.02	4.82	2047210	5.8374%	59.6292%
7	4.82	5.62	1866658	5.3226%	64.9517%
8	5.62	6.43	1778026	5.0698%	70.0216%
9	6.43	7.23	1365212	3.8927%	73.9143%
10	7.23	8.03	1036860	2.9565%	76.8708%
11	8.03	8.84	869057	2.4780%	79.3488%
12	8.84	9.64	820336	2.3391%	81.6879%
13	9.64	10.44	739279	2.1080%	83.7959%
14	10.44	11.25	677297	1.9312%	85.7271%
15	11.25	12.05	635549	1.8122%	87.5393%
16	12.05	12.85	582468	1.6608%	89.2002%
17	12.85	13.65	465734	1.3280%	90.5281%
18	13.65	14.46	359497	1.0251%	91.5532%
19	14.46	15.26	306851	0.8750%	92.4282%
20	15.26	16.06	265284	0.7564%	93.1846%
21	16.06	16.87	214090	0.6105%	93.7950%
22	16.87	17.67	173383	0.4944%	94.2894%
23	17.67	18.47	159171	0.4539%	94.7433%
24	18.47	19.28	132050	0.3765%	95.1198%
25	19.28	20.08	144307	0.4115%	95.5313%
26	20.08	20.88	137519	0.3921%	95.9234%
27	20.88	21.69	109418	0.3120%	96.2354%
28	21.69	22.49	93347	0.2662%	96.5016%
29	22.49	23.29	82473	0.2352%	96.7367%
30	23.29	24.10	72844	0.2077%	96.9444%
31	24.10	24.90	70594	0.2013%	97.1457%
32	24.90	25.70	65636	0.1872%	97.3329%
33	25.70	26.51	59690	0.1702%	97.5031%
34	26.51	27.31	57684	0.1645%	97.6676%
35	27.31	28.11	60717	0.1731%	97.8407%
36	28.11	28.92	49272	0.1405%	97.9812%
37	28.92	29.72	45155	0.1288%	98.1099%

Class #	Range start(cm)	Range end (cm)	Number of points	Percentage	Cumulative
38	29.72	30.52	40837	0.1164%	98.2264%
39	30.52	31.33	36658	0.1045%	98.3309%
40	31.33	32.13	32152	0.0917%	98.4226%
41	32.13	32.93	31015	0.0884%	98.5110%
42	32.93	33.74	28342	0.0808%	98.5918%
43	33.74	34.54	26263	0.0749%	98.6667%
44	34.54	35.34	23341	0.0666%	98.7333%
45	35.34	36.14	21614	0.0616%	98.7949%
46	36.14	36.95	22046	0.0629%	98.8578%
47	36.95	37.75	19004	0.0542%	98.9119%
48	37.75	38.55	17700	0.0505%	98.9624%
49	38.55	39.36	17192	0.0490%	99.0114%
50	39.36	40.16	16508	0.0471%	99.0585%
51	40.16	40.96	16128	0.0460%	99.1045%
52	40.96	41.77	15855	0.0452%	99.1497%
53	41.77	42.57	15422	0.0440%	99.1937%
54	42.57	43.37	15177	0.0433%	99.2370%
55	43.37	44.18	14873	0.0424%	99.2794%
56	44.18	44.98	14682	0.0419%	99.3212%
57	44.98	45.78	14637	0.0417%	99.3630%
58	45.78	46.59	14539	0.0415%	99.4044%
59	46.59	47.39	14384	0.0410%	99.4454%
60	47.39	48.19	13592	0.0388%	99.4842%
61	48.19	49.00	13302	0.0379%	99.5221%
62	49.00	49.80	12764	0.0364%	99.5585%
63	49.80	50.60	11574	0.0330%	99.5915%
64	50.60	51.41	10305	0.0294%	99.6209%
65	51.41	52.21	9357	0.0267%	99.6476%
66	52.21	53.01	9003	0.0257%	99.6732%
67	53.01	53.82	8664	0.0247%	99.6980%
68	53.82	54.62	8316	0.0237%	99.7217%
69	54.62	55.42	7718	0.0220%	99.7437%
70	55.42	56.23	7246	0.0207%	99.7643%
71	56.23	57.03	6897	0.0197%	99.7840%
72	57.03	57.83	6545	0.0187%	99.8027%
73	57.83	58.63	6024	0.0172%	99.8198%
74	58.63	59.44	5823	0.0166%	99.8364%
75	59.44	60.24	5452	0.0155%	99.8520%
76	60.24	61.04	5086	0.0145%	99.8665%
77	61.04	61.85	4834	0.0138%	99.8803%
78	61.85	62.65	4741	0.0135%	99.8938%

Class #	Range start(cm)	Range end (cm)	Number of points	Percentage	Cumulative
79	62.65	63.45	4345	0.0124%	99.9062%
80	63.45	64.26	3840	0.0109%	99.9171%
81	64.26	65.06	3429	0.0098%	99.9269%
82	65.06	65.86	3009	0.0086%	99.9355%
83	65.86	66.67	2800	0.0080%	99.9435%
84	66.67	67.47	2710	0.0077%	99.9512%
85	67.47	68.27	2475	0.0071%	99.9583%
86	68.27	69.08	2107	0.0060%	99.9643%
87	69.08	69.88	1939	0.0055%	99.9698%
88	69.88	70.68	1902	0.0054%	99.9752%
89	70.68	71.49	1821	0.0052%	99.9804%
90	71.49	72.29	1558	0.0044%	99.9849%
91	72.29	73.09	1229	0.0035%	99.9884%
92	73.09	73.90	1079	0.0031%	99.9914%
93	73.90	74.70	818	0.0023%	99.9938%
94	74.70	75.50	703	0.0020%	99.9958%
95	75.50	76.31	484	0.0014%	99.9971%
96	76.31	77.11	375	0.0011%	99.9982%
97	77.11	77.91	250	0.0007%	99.9989%
98	77.91	78.72	193	0.0006%	99.9995%
99	78.72	79.52	130	0.0004%	99.9999%
100	79.52	80.32	52	0.0001%	100.0000%

Table 35: Point cloud deviation classes for the EV building UAS-based point cloud (case study II).

Class #	Range start (cm)	Range end (cm)	Number of points	Percentage	Cumulative
1	0.00	0.81	5,603,825	17.4037%	17.4037%
2	0.81	1.62	5,189,735	16.1177%	33.5214%
3	1.62	2.43	4,290,159	13.3239%	46.8452%
4	2.43	3.24	3,149,181	9.7804%	56.6256%
5	3.24	4.05	2,659,317	8.2590%	64.8846%
6	4.05	4.86	2,084,885	6.4750%	71.3596%
7	4.86	5.67	1,472,048	4.5717%	75.9313%
8	5.67	6.48	1,023,029	3.1772%	79.1085%
9	6.48	7.29	801,717	2.4899%	81.5984%
10	7.29	8.10	648,419	2.0138%	83.6122%
11	8.10	8.91	546,076	1.6959%	85.3081%
12	8.91	9.72	475,778	1.4776%	86.7857%
13	9.72	10.53	416,276	1.2928%	88.0785%
14	10.53	11.34	362,648	1.1263%	89.2048%
15	11.34	12.15	307,060	0.9536%	90.1584%

Class #	Range start (cm)	Range end (cm)	Number of points	Percentage	Cumulative
16	12.15	12.96	270,395	0.8398%	90.9982%
17	12.96	13.77	248,189	0.7708%	91.7690%
18	13.77	14.58	216,262	0.6716%	92.4406%
19	14.58	15.39	196,776	0.6111%	93.0518%
20	15.39	16.20	184,175	0.5720%	93.6238%
21	16.20	17.01	173,540	0.5390%	94.1627%
22	17.01	17.82	162,886	0.5059%	94.6686%
23	17.82	18.63	148,011	0.4597%	95.1283%
24	18.63	19.44	135,349	0.4204%	95.5486%
25	19.44	20.24	125,185	0.3888%	95.9374%
26	20.24	21.05	119,235	0.3703%	96.3077%
27	21.05	21.86	113,051	0.3511%	96.6588%
28	21.86	22.67	98,668	0.3064%	96.9652%
29	22.67	23.48	88,753	0.2756%	97.2409%
30	23.48	24.29	82,322	0.2557%	97.4965%
31	24.29	25.10	79,182	0.2459%	97.7425%
32	25.10	25.91	75,420	0.2342%	97.9767%
33	25.91	26.72	70,681	0.2195%	98.1962%
34	26.72	27.53	63,008	0.1957%	98.3919%
35	27.53	28.34	53,338	0.1657%	98.5575%
36	28.34	29.15	45,485	0.1413%	98.6988%
37	29.15	29.96	36,921	0.1147%	98.8135%
38	29.96	30.77	30,946	0.0961%	98.9096%
39	30.77	31.58	28,244	0.0877%	98.9973%
40	31.58	32.39	26,208	0.0814%	99.0787%
41	32.39	33.20	24,401	0.0758%	99.1545%
42	33.20	34.01	22,993	0.0714%	99.2259%
43	34.01	34.82	21,716	0.0674%	99.2933%
44	34.82	35.63	20,169	0.0626%	99.3559%
45	35.63	36.44	18,985	0.0590%	99.4149%
46	36.44	37.25	17,720	0.0550%	99.4699%
47	37.25	38.06	16,599	0.0516%	99.5215%
48	38.06	38.87	15,114	0.0469%	99.5684%
49	38.87	39.68	12,783	0.0397%	99.6081%
50	39.68	40.49	11,157	0.0347%	99.6428%
51	40.49	41.30	10,065	0.0313%	99.6740%
52	41.30	42.11	9,439	0.0293%	99.7034%
53	42.11	42.92	8,430	0.0262%	99.7295%
54	42.92	43.73	7,065	0.0219%	99.7515%
55	43.73	44.54	5,520	0.0171%	99.7686%
56	44.54	45.35	4,816	0.0150%	99.7836%

Class #	Range start (cm)	Range end (cm)	Number of points	Percentage	Cumulative
57	45.35	46.16	4,544	0.0141%	99.7977%
58	46.16	46.97	4,266	0.0132%	99.8109%
59	46.97	47.78	3,940	0.0122%	99.8232%
60	47.78	48.59	3,424	0.0106%	99.8338%
61	48.59	49.40	3,154	0.0098%	99.8436%
62	49.40	50.21	2,981	0.0093%	99.8529%
63	50.21	51.02	3,030	0.0094%	99.8623%
64	51.02	51.83	2,787	0.0087%	99.8709%
65	51.83	52.64	2,093	0.0065%	99.8774%
66	52.64	53.45	2,143	0.0067%	99.8841%
67	53.45	54.26	2,468	0.0077%	99.8918%
68	54.26	55.07	2,627	0.0082%	99.8999%
69	55.07	55.88	2,274	0.0071%	99.9070%
70	55.88	56.69	2,183	0.0068%	99.9138%
71	56.69	57.50	1,967	0.0061%	99.9199%
72	57.50	58.31	1,980	0.0061%	99.9260%
73	58.31	59.12	1,708	0.0053%	99.9313%
74	59.12	59.92	1,696	0.0053%	99.9366%
75	59.92	60.73	1,563	0.0049%	99.9414%
76	60.73	61.54	1,523	0.0047%	99.9462%
77	61.54	62.35	1,395	0.0043%	99.9505%
78	62.35	63.16	1,356	0.0042%	99.9547%
79	63.16	63.97	1,250	0.0039%	99.9586%
80	63.97	64.78	1,103	0.0034%	99.9620%
81	64.78	65.59	1,104	0.0034%	99.9654%
82	65.59	66.40	1,027	0.0032%	99.9686%
83	66.40	67.21	940	0.0029%	99.9716%
84	67.21	68.02	897	0.0028%	99.9743%
85	68.02	68.83	891	0.0028%	99.9771%
86	68.83	69.64	816	0.0025%	99.9796%
87	69.64	70.45	811	0.0025%	99.9822%
88	70.45	71.26	738	0.0023%	99.9845%
89	71.26	72.07	657	0.0020%	99.9865%
90	72.07	72.88	618	0.0019%	99.9884%
91	72.88	73.69	615	0.0019%	99.9903%
92	73.69	74.50	549	0.0017%	99.9920%
93	74.50	75.31	517	0.0016%	99.9936%
94	75.31	76.12	430	0.0013%	99.9950%
95	76.12	76.93	394	0.0012%	99.9962%
96	76.93	77.74	347	0.0011%	99.9973%
97	77.74	78.55	313	0.0010%	99.9982%

Class #	Range start (cm)	Range end (cm)	Number of points	Percentage	Cumulative
98	78.55	79.36	275	0.0009%	99.9991%
99	79.36	80.17	198	0.0006%	99.9997%
100	80.17	80.98	93	0.0003%	100.0000%

Table 36: Point cloud deviation analysis for the UAS-based point cloud using normal lighting conditions.

Class #	Range Start (cm)	Range End (cm)	Percentage	Cumulative
1	0.00	0.80	23.06477%	23.06477%
2	0.80	1.59	22.17399%	45.23876%
3	1.59	2.39	12.32338%	57.56213%
4	2.39	3.18	6.41021%	63.97235%
5	3.18	3.98	4.53017%	68.50251%
6	3.98	4.77	3.45638%	71.95889%
7	4.77	5.57	2.87258%	74.83147%
8	5.57	6.36	2.49452%	77.32599%
9	6.36	7.16	2.24046%	79.56645%
10	7.16	7.95	1.97556%	81.54201%
11	7.95	8.74	1.81149%	83.35349%
12	8.74	9.54	1.62380%	84.97729%
13	9.54	10.33	1.44725%	86.42454%
14	10.33	11.13	1.34698%	87.77152%
15	11.13	11.92	1.20440%	88.97592%
16	11.92	12.72	1.11300%	90.08892%
17	12.72	13.51	0.95286%	91.04178%
18	13.51	14.31	0.85986%	91.90164%
19	14.31	15.10	0.77443%	92.67607%
20	15.10	15.90	0.66746%	93.34353%
21	15.90	16.69	0.59781%	93.94135%
22	16.69	17.49	0.53154%	94.47288%
23	17.49	18.28	0.48182%	94.95470%
24	18.28	19.08	0.43891%	95.39362%
25	19.08	19.87	0.40785%	95.80147%
26	19.87	20.67	0.38392%	96.18540%
27	20.67	21.46	0.36116%	96.54656%
28	21.46	22.26	0.34669%	96.89324%
29	22.26	23.05	0.32378%	97.21702%
30	23.05	23.85	0.30173%	97.51876%
31	23.85	24.64	0.28692%	97.80568%
32	24.64	25.44	0.25711%	98.06279%
33	25.44	26.23	0.22422%	98.28702%
34	26.23	27.03	0.19960%	98.48661%

Class #	Range Start (cm)	Range End (cm)	Percentage	Cumulative
35	27.03	27.82	0.17103%	98.65764%
36	27.82	28.62	0.15244%	98.81007%
37	28.62	29.41	0.14449%	98.95456%
38	29.41	30.21	0.12696%	99.08153%
39	30.21	31.00	0.11608%	99.19761%
40	31.00	31.80	0.11041%	99.30802%
41	31.80	32.59	0.10281%	99.41083%
42	32.59	33.39	0.09048%	99.50131%
43	33.39	34.18	0.07414%	99.57545%
44	34.18	34.98	0.06260%	99.63806%
45	34.98	35.77	0.05576%	99.69382%
46	35.77	36.57	0.04874%	99.74256%
47	36.57	37.36	0.04243%	99.78499%
48	37.36	38.16	0.04290%	99.82789%
49	38.16	38.95	0.02633%	99.85421%
50	38.95	39.75	0.01969%	99.87390%
51	39.75	40.54	0.01758%	99.89148%
52	40.54	41.34	0.01463%	99.90611%
53	41.34	42.13	0.01077%	99.91688%
54	42.13	42.93	0.00843%	99.92531%
55	42.93	43.72	0.00791%	99.93323%
56	43.72	44.52	0.00674%	99.93996%
57	44.52	45.31	0.00395%	99.94391%
58	45.31	46.11	0.00255%	99.94646%
59	46.11	46.90	0.00227%	99.94873%
60	46.90	47.69	0.00203%	99.95076%
61	47.69	48.49	0.00204%	99.95280%
62	48.49	49.28	0.00213%	99.95493%
63	49.28	50.08	0.00200%	99.95694%
64	50.08	50.87	0.00204%	99.95898%
65	50.87	51.67	0.00175%	99.96073%
66	51.67	52.46	0.00190%	99.96263%
67	52.46	53.26	0.00194%	99.96457%
68	53.26	54.05	0.00182%	99.96639%
69	54.05	54.85	0.00199%	99.96838%
70	54.85	55.64	0.00154%	99.96992%
71	55.64	56.44	0.00174%	99.97166%
72	56.44	57.23	0.00165%	99.97331%
73	57.23	58.03	0.00159%	99.97490%
74	58.03	58.82	0.00140%	99.97629%
75	58.82	59.62	0.00153%	99.97782%

Class #	Range Start (cm)	Range End (cm)	Percentage	Cumulative
76	59.62	60.41	0.00147%	99.97929%
77	60.41	61.21	0.00134%	99.98063%
78	61.21	62.00	0.00128%	99.98191%
79	62.00	62.80	0.00135%	99.98325%
80	62.80	63.59	0.00130%	99.98455%
81	63.59	64.39	0.00120%	99.98575%
82	64.39	65.18	0.00130%	99.98705%
83	65.18	65.98	0.00108%	99.98813%
84	65.98	66.77	0.00107%	99.98919%
85	66.77	67.57	0.00108%	99.99027%
86	67.57	68.36	0.00102%	99.99130%
87	68.36	69.16	0.00104%	99.99233%
88	69.16	69.95	0.00088%	99.99322%
89	69.95	70.75	0.00091%	99.99413%
90	70.75	71.54	0.00082%	99.99495%
91	71.54	72.34	0.00081%	99.99576%
92	72.34	73.13	0.00082%	99.99657%
93	73.13	73.93	0.00063%	99.99721%
94	73.93	74.72	0.00061%	99.99782%
95	74.72	75.52	0.00053%	99.99835%
96	75.52	76.31	0.00049%	99.99884%
97	76.31	77.11	0.00040%	99.99924%
98	77.11	77.90	0.00030%	99.99954%
99	77.90	78.70	0.00026%	99.99981%
100	78.70	79.49	0.00019%	100.00000%

Table 37: Point cloud deviation analysis for the UAS-based point cloud using low lighting conditions.

Class #	Range Start (cm)	Range End (cm)	Percentage	Cumulative
1	0.00	0.76	12.8899%	12.8899%
2	0.76	1.52	13.4810%	26.3709%
3	1.52	2.27	10.0718%	36.4427%
4	2.27	3.03	7.7961%	44.2389%
5	3.03	3.78	7.8900%	52.1289%
6	3.78	4.54	6.3922%	58.5210%
7	4.54	5.30	5.2249%	63.7460%
8	5.30	6.05	4.6522%	68.3982%
9	6.05	6.81	3.1981%	71.5962%
10	6.81	7.57	2.8434%	74.4397%
11	7.57	8.32	2.4196%	76.8593%
12	8.32	9.08	2.1028%	78.9620%

Class #	Range Start (cm)	Range End (cm)	Percentage	Cumulative
13	9.08	9.84	1.9252%	80.8872%
14	9.84	10.59	1.7525%	82.6397%
15	10.59	11.35	1.5834%	84.2232%
16	11.35	12.10	1.4591%	85.6822%
17	12.10	12.86	1.2392%	86.9214%
18	12.86	13.62	1.1125%	88.0340%
19	13.62	14.37	0.9809%	89.0149%
20	14.37	15.13	0.8863%	89.9012%
21	15.13	15.89	0.8378%	90.7390%
22	15.89	16.64	0.8219%	91.5608%
23	16.64	17.40	0.7335%	92.2943%
24	17.40	18.16	0.6550%	92.9494%
25	18.16	18.91	0.5651%	93.5145%
26	18.91	19.67	0.5079%	94.0225%
27	19.67	20.42	0.4614%	94.4838%
28	20.42	21.18	0.4331%	94.9170%
29	21.18	21.94	0.4165%	95.3335%
30	21.94	22.69	0.3832%	95.7166%
31	22.69	23.45	0.3392%	96.0559%
32	23.45	24.21	0.2982%	96.3541%
33	24.21	24.96	0.2872%	96.6412%
34	24.96	25.72	0.2632%	96.9044%
35	25.72	26.48	0.2393%	97.1437%
36	26.48	27.23	0.2207%	97.3644%
37	27.23	27.99	0.2016%	97.5660%
38	27.99	28.74	0.1841%	97.7500%
39	28.74	29.50	0.1699%	97.9200%
40	29.50	30.26	0.1515%	98.0715%
41	30.26	31.01	0.1429%	98.2143%
42	31.01	31.77	0.1336%	98.3480%
43	31.77	32.53	0.1258%	98.4737%
44	32.53	33.28	0.1105%	98.5842%
45	33.28	34.04	0.0943%	98.6785%
46	34.04	34.80	0.0846%	98.7631%
47	34.80	35.55	0.0750%	98.8382%
48	35.55	36.31	0.0682%	98.9064%
49	36.31	37.06	0.0555%	98.9619%
50	37.06	37.82	0.0493%	99.0112%
51	37.82	38.58	0.0444%	99.0556%
52	38.58	39.33	0.0425%	99.0981%
53	39.33	40.09	0.0402%	99.1383%

Class #	Range Start (cm)	Range End (cm)	Percentage	Cumulative
54	40.09	40.85	0.0386%	99.1769%
55	40.85	41.60	0.0385%	99.2154%
56	41.60	42.36	0.0377%	99.2530%
57	42.36	43.12	0.0370%	99.2901%
58	43.12	43.87	0.0366%	99.3266%
59	43.87	44.63	0.0369%	99.3635%
60	44.63	45.38	0.0361%	99.3996%
61	45.38	46.14	0.0357%	99.4352%
62	46.14	46.90	0.0360%	99.4712%
63	46.90	47.65	0.0354%	99.5066%
64	47.65	48.41	0.0352%	99.5418%
65	48.41	49.17	0.0336%	99.5754%
66	49.17	49.92	0.0310%	99.6065%
67	49.92	50.68	0.0288%	99.6353%
68	50.68	51.44	0.0277%	99.6630%
69	51.44	52.19	0.0260%	99.6890%
70	52.19	52.95	0.0240%	99.7130%
71	52.95	53.70	0.0233%	99.7363%
72	53.70	54.46	0.0273%	99.7636%
73	54.46	55.22	0.0289%	99.7924%
74	55.22	55.97	0.0252%	99.8176%
75	55.97	56.73	0.0270%	99.8446%
76	56.73	57.49	0.0220%	99.8666%
77	57.49	58.24	0.0188%	99.8854%
78	58.24	59.00	0.0192%	99.9046%
79	59.00	59.75	0.0169%	99.9215%
80	59.75	60.51	0.0120%	99.9334%
81	60.51	61.27	0.0101%	99.9436%
82	61.27	62.02	0.0086%	99.9522%
83	62.02	62.78	0.0058%	99.9580%
84	62.78	63.54	0.0042%	99.9622%
85	63.54	64.29	0.0043%	99.9665%
86	64.29	65.05	0.0040%	99.9705%
87	65.05	65.81	0.0035%	99.9740%
88	65.81	66.56	0.0034%	99.9774%
89	66.56	67.32	0.0030%	99.9804%
90	67.32	68.07	0.0030%	99.9833%
91	68.07	68.83	0.0027%	99.9861%
92	68.83	69.59	0.0026%	99.9887%
93	69.59	70.34	0.0024%	99.9910%
94	70.34	71.10	0.0020%	99.9930%

Class #	Range Start (cm)	Range End (cm)	Percentage	Cumulative
95	71.10	71.86	0.0019%	99.9950%
96	71.86	72.61	0.0016%	99.9966%
97	72.61	73.37	0.0012%	99.9978%
98	73.37	74.13	0.0010%	99.9988%
99	74.13	74.88	0.0008%	99.9996%
100	74.88	75.64	0.0004%	100.0000%